Numerical Modeling of a Radio-Frequency Micro Ion Thruster

by

Michael Meng-Tsuan Tsay

Submitted to the Department of Aeronautics and Astronautics
in partial fulfillment of the requirements for the degree of

Master of Science in Aeronautics and Astronautics
at the
MASSACHUSETTS INSTITUTE OF TECHNOLOGY

May 2006

Author.....
Department of Aeronautics and Astronautics
May 26, 2006

Certified by.....
Manuel Martinez-Sanchez
Professor
Thesis Supervisor

Accepted by.....
Jaime Peraire
Professor of Aeronautics and Astronautics
Chair, Committee on Graduate Students

Numerical Modeling of a Radio-Frequency Micro Ion Thruster

by

Michael Meng-Tsuan Tsay

Submitted to the Department of Aeronautics and Astronautics
on May 26, 2006, in partial fulfillment of the
requirements for the degree of
Master of Science in Aeronautics and Astronautics

Abstract

A simple performance model is developed for an inductively-coupled radio-frequency micro ion thruster. Methods of particle and energy balance are utilized for modeling the chamber plasma discharge. A transformer model is incorporated in the equations of energy balance for investigating the effect of plasma on the primary circuit and for calculating the absorbed power by the plasma. A simple and one-dimensional ion extraction model is developed based on experimental observation and the result is validated with experimental data. Performance of the RF micro ion thruster is satisfactory with thrust and specific impulse of approximately 2 mN and 2000 seconds, respectively. Comparison is made with a miniature bombardment-type ion thruster, and the RF ion thruster is found to be more efficient when the coupling efficiency is above 80%. Optimization in driving frequency increases power absorption and ionization fraction tremendously. It has a positive but limited effect on propulsive performance as the ion beam current is space-charge limited.

Thesis Supervisor: Manuel Martinez-Sanchez
Title: Professor

Acknowledgements

I would like to express my deepest gratitude to my advisor, Professor Martinez-Sanchez, for his patience and encouragement. Without his guidance, I would not have the slightest idea on how to approach this project. In addition, I appreciate the help from Kurt Hohman and Lynn Olson of Busek, for providing me the experimental data and technical support. I also thank people from Mathworks for doing a wonderful job on developing MATLAB. Its usefulness surely made my life much easier.

Members of SPL, especially Paulo, Justin, Tanya, Felix and Ben (recently graduated) have been a big help during my course of study, academically and personally. These cool people provided me warm company when sometimes things got too tough or just plain boring. My officemates, Aya and Scott, have also entertained me during my everyday life in the office, and I thank them for building a comfortable atmosphere in the office so I can drag myself here to complete this thesis.

I thank Mom and Dad for being my piggy bank when funding got rough, and I also thank my sister for being there with open arms when I need some company during holidays. Last but not least, I would like to thank my girlfriend, Yuko, for being there at the most stressful time of my life: the qualifying exam. She has been the reason that kept me going. Regardless of the future, I appreciate her presence and her belief in me.

Contents

List of Figures

List of Tables

Nomenclature

ID	=	tube inner diameter	V_i	=	first ionization energy
R	=	tube inner radius	$V_{exc.}$	=	excitation energy
l	=	tube length	D_m	=	magnetic diffusivity
N	=	number of turns	ω	=	RF driving frequency
I_c	=	current in the coil	δ	=	skin depth
n_e	=	electron number density	σ	=	electric conductivity
n_i	=	ion number density	C	=	capacitance
n_n	=	neutral number density	L_c	=	coil inductance
$n_{s,L}$	=	axial sheath electron density	R_c	=	coil resistance
$n_{s,R}$	=	radial sheath electron density	L_p	=	plasma self-inductance
d_{eff}	=	effective plasma size	R_p	=	plasma resistance
A_{eff}	=	effective area for particle loss	L_2	=	transformed plasma inductance
V_{eff}	=	effective discharge volume	R_2	=	transformed plasma resistance
T_e	=	electron temperature	L_m	=	mutual inductance
T_i	=	ion temperature	P_{rf}	=	RF power
T_n	=	neutral temperature	P_{abs}	=	absorbed power by plasma
T_w	=	wall temperature	V_{net}	=	anode-cathode voltage
m_e	=	electron mass	V_{total}	=	anode-accelerator voltage
m_i	=	ion mass	A_{grid}	=	grid area
m_n	=	neutral mass	l_g	=	grid spacing
u_B	=	Bohm velocity	Γ	=	total flux

υ_i	=	ionization frequency	φ_i	=	grid transparency for ion
h_L	=	normalized axial sheath edge density	φ_n	=	grid transparency for neutrals
h_R	=	normalized radial sheath edge density	J	=	total current
λ_i	=	ion mean free path	η_u	=	utilization efficiency
Q_{in}	=	ion-neutral scattering cross-section	T	=	thrust
Q_{en}	=	e–n scattering cross-section	I_{sp}	=	specific impulse
γ	=	T_e/T_i	C	=	exit velocity
υ_{in}	=	ion-neutral collision frequency	P_{beam}	=	beam power
υ_{en}	=	electron-neutral collision frequency	η_e	=	electrical efficiency
$\sigma_{ion.}$	=	ionization cross-section	α	=	ionization fraction
c	=	particle thermal velocity	k	=	Boltzmann's constant

Chapter 1

Introduction

1.1 Overview

Ion thrusters, also known as ion engines, are electrostatic thrusters that rely on Coulomb forces to accelerate positively charged heavy-molecular-mass particles. Heavy noble gases, such as Argon and Xenon, are often chosen as propellant because of their stable and non-toxic nature. In addition, they carry higher momentum and thus produce more thrust-per-unit-area than light particles do when subjected to the same accelerating potential. In general, an ion thruster consists of an ionization chamber with or without an internal electron-emitting cathode depending on the ionization scheme, a grid system used for ion extraction and acceleration, and an external cathode used for plume neutralization. The most common type of ion thruster is the direct-current (DC) electron-bombardment ion thruster that was first developed by Kaufman from NASA in the 1960s. Other types of ion thrusters include inductively-coupled plasma (ICP) discharge radio-frequency (RF) ion thruster and electron cyclotron resonance (ECR) RF ion thruster. Work on ICP RF ion thrusters for the most part has been done by German scientists, while researches on ECR RF ion thrusters are primarily conducted in Japan.

1.2 Inductively-Coupled RF Ion Thrusters

ICP RF ion thrusters were first invented by Professor Loeb at the Giessen University of Germany in the 1960s. Since then, the European Aeronautic Defense and Space Company (EADS) Space Transportation GmbH and its industrial support, the German Astrium GmbH group, have adapted this concept and successfully developed a family of space-qualified RF thrusters known as the Radio-frequency Ion Thruster (RIT) series [1]. The flight models are also referred to as Radio-frequency Ion Thruster Assembly (RITA) series. The scope of this thesis research focuses on this type of ion thruster because of its long heritage and history of successful flight operations.

1.2.1 Design Concept

A two-grid Kaufman type of ion thruster with static ring-cusp magnetic field is shown in Figure 1. Major features of this type of thruster include an applied discharge potential and an internal hollow cathode for emitting primary electrons to "bombard" the neutral particles in order to achieve ionization. The ring-cusp shape of magnetic field is produced by permanent magnets and is used to confine the primary electrons and prolong their presence in the ionization chamber before being lost to the walls [2]. Figure 2 shows the schematics of a two-grid ICP RF ion thruster that is similar to the design used in the German RIT series. Unlike DC ion thrusters that use electron bombardment for ionization, ICP RF ion thrusters utilize electromagnetic fields induced by high-frequency coil currents to energize free electrons azimuthally. More specifically, the primary electric field in the coil induces an axial magnetic field, which in turn induces a secondary circular electric field by Maxwell's Law. Free electrons in the ionization chamber are energized and accelerated in this secondary electric field. Self-sustained ionization is then achieved by subsequent collisions and energy transfer with low-energy neutral particles along the path. During such process, the inductance of the plasma is coupled with the coil inductance, thus receiving its name of inductively-couple ion thrusters.

The success of German RIT-series ion thrusters proved that this RF technology can be robust and dependable. However, during the course of this thesis research, some difficulties in starting the plasma discharge were observed in experiments, possibly due to the lack of initial free electrons. A high-voltage device such as a Tesla coil was used to ignite the plasma, but its usage might not be necessary as the experiments are improved. It should be noted that the "positive high voltage" and "negative high voltage" in Figure 2 will be referred to as "anode bias" and "accelerator bias", respectively, in the following sections of this thesis. A simplified circuit realization of the acceleration system showing these two applied potentials can be found in Figure 12 in Section 2.4.1.

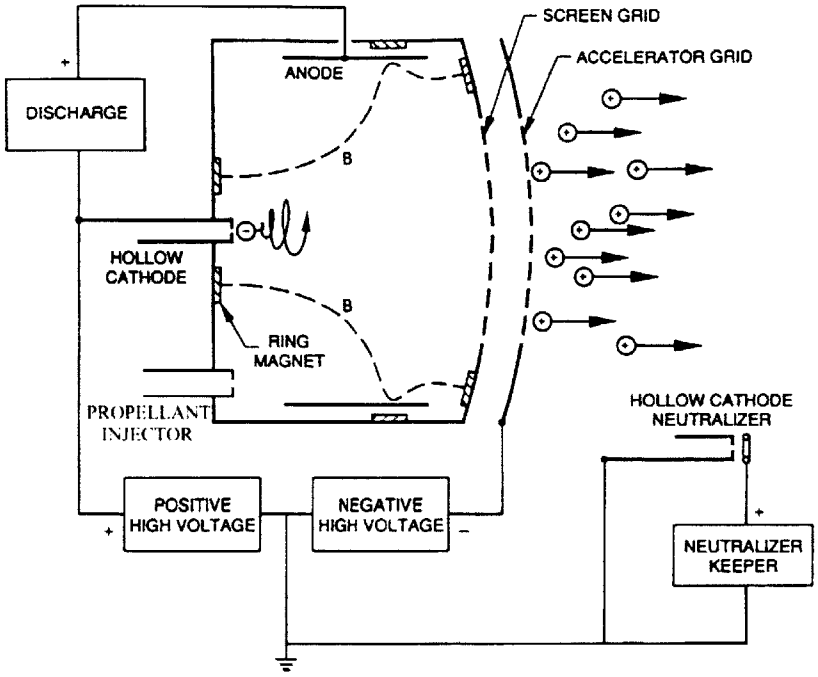

Figure 1: Schematics of a ring-cusped DC electron bombardment ion thruster [2].

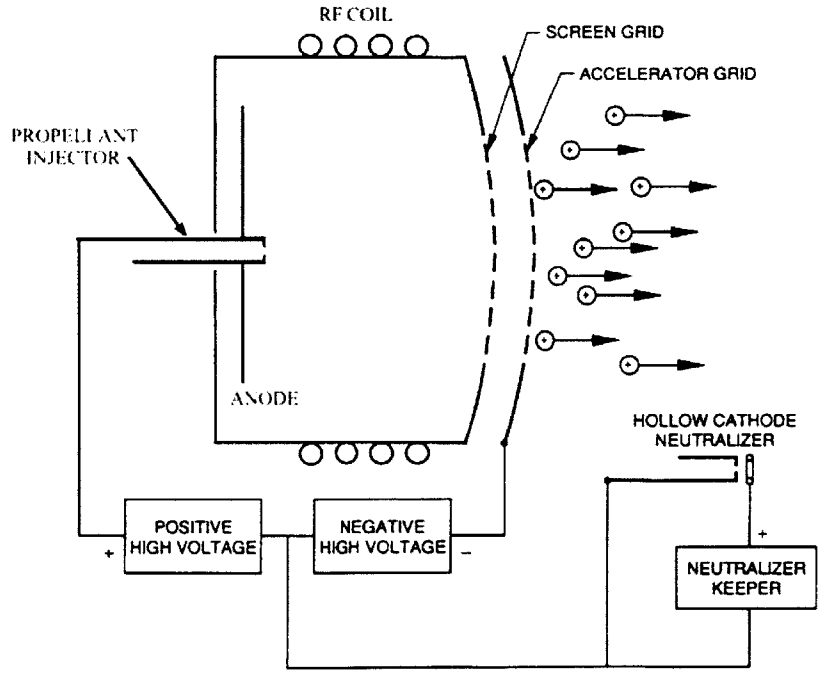

Figure 2: Schematics of an inductively-coupled RF ion thruster.

1.2.2 Advantages and Applications

The most prominent advantage of a RF ion thruster compared to its DC counterpart is the prolonged operational life due to the absence of the life-limiting internal hot cathode. The most recent RIT-series ion thrusters developed by EADS, the 200 mN class RIT-XT and RIT-22, can easily achieve life of > 10,000 hours with continuous firing capability, while preserving other favorable characteristics of a typical DC ion thruster, such as high specific impulse (> 3000 seconds), high propellant utilization (> 85%) and high efficiency (> 80%) [3,4,5]. Although the above reference data do not necessarily reflect the performance of a model of smaller scale, they demonstrate competency of the design. Overall, the durability of a RF ion thruster enables it to carry out interplanetary or north-south station keeping (NSSK) missions that requires either long firing time or long service life.

In comparison with ECR RF ion thrusters, ICP RF ion thrusters also possess a few advantages. ICP thrusters are operated at much lower frequency (MHz range) than ECR thrusters do (GHz range), thus the requirements on the power unit are not as strict. In addition, ECR thrusters require external static magnetic field and a fixed propellant flow rate in order to establish an electron cyclotron resonance; therefore thrust level is limited by the designated resonant frequency and input power. Such limitations do not exist in ICP thrusters; the mass flow rate and input power can be varied over an extremely wide range [5]. As a result, thrust level is easily adjustable by changing either flow control unit or input RF power. This feature enables ICP RF thrusters for precision propulsion and makes them suitable for delicate satellite formation missions. Miniature version of ICP RF ion thrusters have been proposed for potential NASA missions that require precision propulsion. These missions include the Space Interferometer Mission (SIM), Space Astronomy Far Infrared Telescope (SAFIR), Laser Interferometer Space Antenna (LISA), Micro-Arcsecond X-ray Imaging Mission (MAXIM) and Submillimeter Probe of the Evolution of Cosmic Structure (SPECS) [6].

1.2.3 History of Operations

The European Space Agency (ESA) and EADS had two successful satellite missions involving the use of ICP RF ion thrusters, RITA-10. The first mission, the European Retrievable Carrier (EURECA), was launched on 1992 by Space Shuttle Atlantis. EURECA was the largest spacecraft ever built by ESA, and it was to orbit the Earth and later be retrieved for sample access in 1993 by Space Shuttle Endeavor. During the year-long flight in space, RITA-10 powered EURECA flawlessly for 240 hours and no interference with satellite, payload or electronics was noticed [3].

Since the EURECA mission, the performance of RITA-10 was increased to over 20,000 hours of operation and it was eventually used to recovery the Advanced Relay Technology Mission (ARTEMIS) in 2002. The ARTEMIS satellite was originally designed to operate in a geosynchronous orbit at 36,000 km. However, due to an upper stage malfunction, ARTEMIS was stuck at a circular orbit at 31,000 km. With a thrust of only 15 mN, RITA-10 slowly but successfully raised the ARTEMIS to the targeted geosynchronous orbit, and thus rescued the ARTEMIS mission. To date, RITA-10 has been serving ARTEMIS flawlessly for its planned 10-year mission [3].

1.3 Project Motivation

During the 40 years of development of inductively-coupled RF ion thrusters, there have been numerous experimental and some computational works published by the German Astrium group and other scientists. However, there is no simple performance model like the one developed for DC ion thrusters by Brophy and Wilbur in 1980s. This simple mathematical performance model, well known as Brophy's model, is essentially a particle and energy balance calculation that relates thruster performance to adjustable operation parameters such as mass flow rate, propellant type, discharge potential and physical grid transparency [7]. Inspired by Brophy's model, this project intended to compute plasma properties and thruster performance of an inductively-coupled RF ion thruster with a similar approach. Although the calculation was not expected to be as simple as the algebraic expressions found in the Brophy's model, it should still be easy to use.

1.4 Objectives

As mentioned in the previous section, the main objective of this project is to develop a simple mathematical model that is comprehensible and easy to use for an inductively-coupled RF ion thruster. Instead of a fully kinetic particle simulation program, a less complex 1-D axisymmetrical computation code is developed to perform the necessary particle and energy balance calculations in ICP discharge. This code is required because there is no straightforward algebraic solution; heavy iterations are necessary in order to achieve the objectives. In addition, a circuit model and a simple ion extraction model are also developed for completing the performance analysis. In short, this project is to create a tool package for analyzing the characteristics and performance of an ICP RF ion thruster. This package includes circuit analysis, particle and energy balance in ICP discharge, and ion beam prediction from a two-grid acceleration system.

1.5 Experimental Data

This project was initiated to supplement the experimental work done by Busek Co. for the fulfillment of its NASA Small Business Innovation Research (SBIR) Phase I contract in 2005. Experimental data, provided by Mr. Kurt Hohman and Dr. Lynn Wilson of Busek, are used to validate the computation results. For the Phase I experiments, continuous ICP discharge was sustained for a 3 cm diameter RF micro ion thruster. Estimated thrust level was 2 mN when operated with 27 W forward power, 1 sccm Xenon flow and 1075 V inter-grid potential. Operation of the thruster in a vacuum chamber is shown in Figure 3.

A conceptual schematic of the Phase I thruster is shown in Figure 4. The drawing does not bear any dimensional accuracy. This prototype design resembles the configuration of a German RIT-series thruster except for the placement of anode; the anode is positioned internally instead of connecting at the screen grid. A capacitive matching network was placed in parallel with the coil circuit to ensure maximum power delivery to the plasma. A fixed-capacitance capacitor was used and the source frequency was adjusted to seek the matching condition. In experiments, separate power units were used for RF input power and accelerating potential. These power units will eventually be integrated into one for developing a flight model.

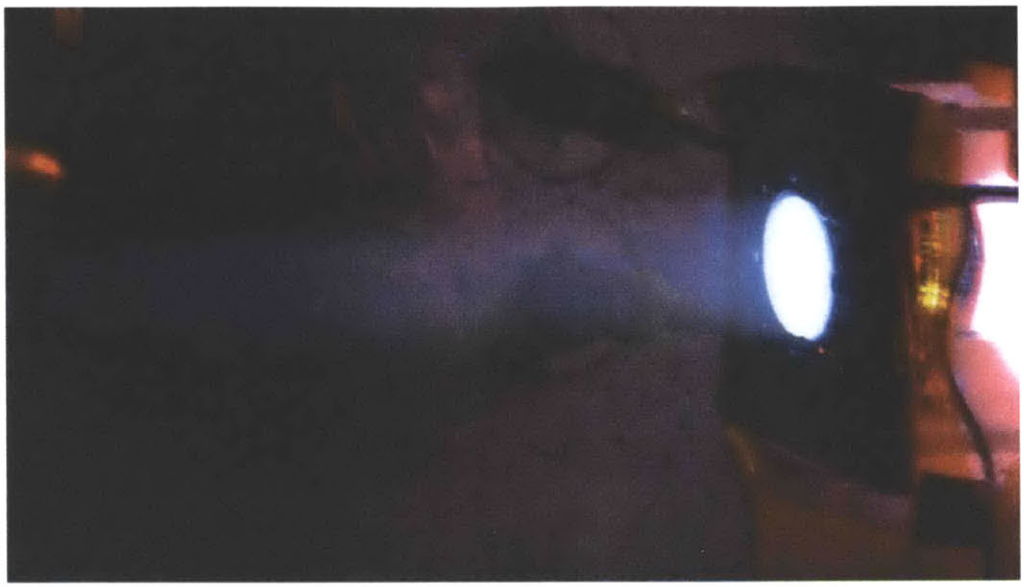

Figure 3: RF micro ion thruster operating in a vacuum chamber.

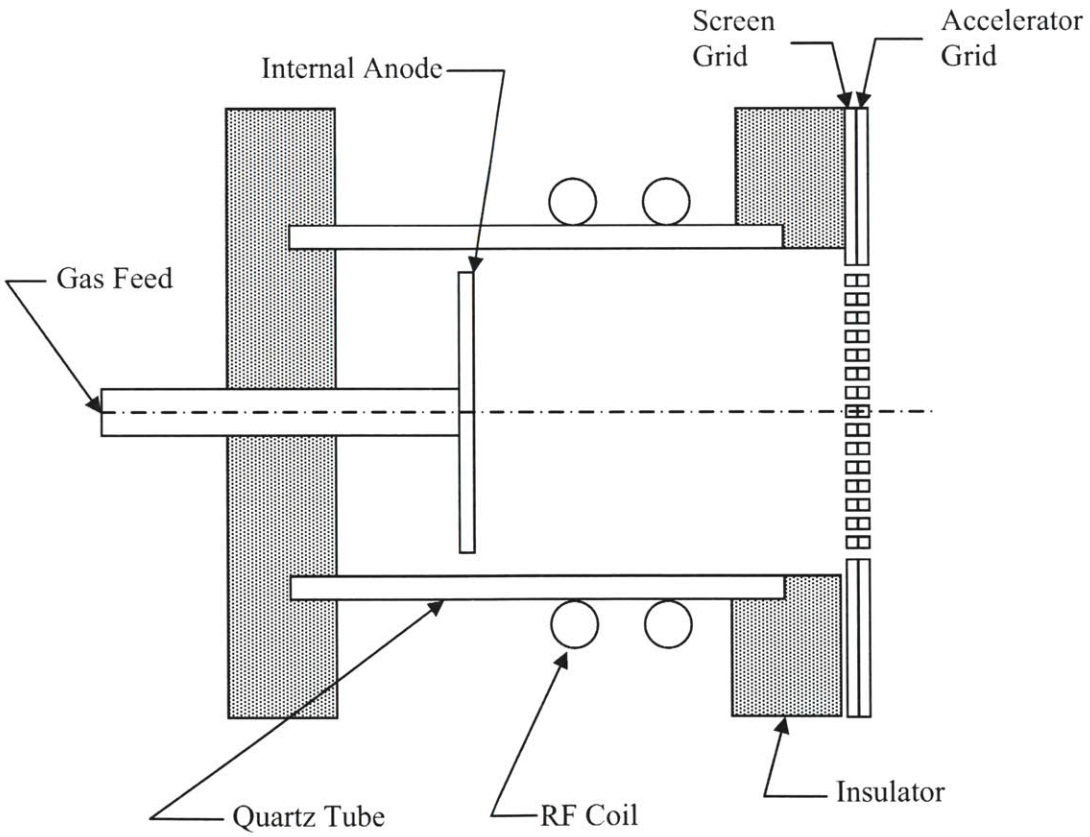

Figure 4: Conceptual arrangement of the RF micro ion thruster used in Phase I experiments. Drawing not to scale.

1.6 Thesis Outline

Theory on ICP discharge and ion extraction is discussed in next chapter, followed by outlines of the computation code in Chapter 3. Computation results are compared with available experimental data in Chapter 4. Discussions on the findings are also included in Chapter 4, followed by conclusion and thesis summary in Chapter 5. Three appendices are attached at the end of this thesis. Appendix A is a user's manual for running the simulation code. Appendix B shows the list of executable program and subprograms. Lastly, Appendix C presents an example of the program output.

Chapter 2

Theory

2.1 Overview

This chapter contains the fundamental physics behind this project. It consists of three major parts: ICP discharge model, network matching and circuit analysis, and ion extraction model. In the ICP discharge model, bulk plasma properties are calculated by means of a particle balance and an energy balance. Approximations are made in the calculation to include only dominant factors. The circuit network analysis is used for calculating power deposited into the plasma, and calculated reflected power is used to compare with experimental results in Chapter 4. A simplified 1-D ion extraction model is developed based on the experimental research conducted by D.C. Rovang and P.J. Wilbur in the1980s. Simulation results obtained from this extraction model are also compared with experiments in Chapter 4. Electron temperatures shown in the equations are in unit of Kelvin unless noted.

2.2 Inductively-Coupled Plasma Discharge Model

A global ICP discharge model published in 1994 by Lierberman and Gottscho is discussed in this section. In this model, electron density is considered to be volume-averaged and electron temperature is assumed to be uniform. Also, particles are assumed to have relaxed into a Maxwellian distribution. In this section, equations regarding particle balance and energy balance in an ICP discharge are introduced. These equations are used to calculate electron temperature and density, as well as other plasma properties. The effect of electromagnetic wave penetration, also known as the "skin depth" effect of RF plasma, is also discussed.

2.2.1 Particle Balance and Electron Temperature

Electron temperature in an ICP RF ion thruster is mainly affected by electron-neutral collisions and is usually kept low (less than 5 eV). This feature is very similar to the one in a typical DC ion thruster, since both types of thruster contain a low-density plasma source. Such level of

electron temperature is quite attractive because the electrons are energetic enough to initiate ionization but do not have too much excess kinetic energy to cause significant power loss to the anode.

The solution for the electron temperature can be found by means of a particle balance when the chamber geometry, wall temperature and background neutral particle density are specified. In the model described by Lierberman and Gottscho, the governing equation for calculating electron temperature is derived by assuming that ions and electrons only recombine at the wall. Particle balance is then achieved by equating ionization rate to diffusion loss rate. This statement can be expressed as [8]

$$\nu_i = \frac{u_B}{d_{eff}} \tag{1}$$

where ν_i represents ionization frequency. The right-hand side of Eq. 1 describes rate of particle loss due to diffusion, and it is related to some effective plasma size d_{eff} and the velocity u_B of ions entering the sheath. From the Bohm sheath criterion, this velocity is equal to the velocity of ions having energy corresponding to the electron temperature and is therefore referred to as the Bohm velocity u_B [9],

$$u_B = \sqrt{\frac{kT_e}{m_i}} \tag{2}$$

Another important assumption regarding Eq. 1 is that singly-charged ions and neutrals are thermalized with chamber wall in steady-state operation; in other words, $T_i = T_n \approx T_w$. In addition, from quasi-neutrality of the plasma, a uniform density profile ($n_e = n_i = n_0$) is assumed across discharge except near the wall, where densities drop sharply to some sheath edge density n_s. The effective plasma size can be written as [8]

$$d_{eff} = \frac{1}{2}\frac{Rl}{Rh_L + lh_R} \tag{3}$$

A similar parameter, the effective area for particle loss can also be defined as

$$A_{eff} = 2\pi R\left(Rh_L + lh_R\right) \tag{4}$$

, in which h_L and h_R are the normalized axial and radial sheath edge densities, respectively. The expressions of normalized axial and radial sheath edge densities are formulated by Lee and Lieberman [8]

$$h_L = \frac{n_{s,L}}{n_0} = \frac{0.86}{\left[3 + (l/2\lambda_i) + (0.86lu_B/\pi\gamma D_i)^2\right]^{1/2}} \approx 0.5 \tag{5}$$

$$h_R = \frac{n_{s,R}}{n_0} = \frac{0.8}{\left[4 + (R/\lambda_i) + (0.8Ru_B/2.405J_1(2.405)\gamma D_i)^2\right]^{1/2}} \approx 0.4 \tag{6}$$

where λ_i is the mean free path for ions usually much larger than the dimension of the thruster, γ is the ratio between electron and ion temperature and D_i is the ion diffusion coefficient. These three parameters are expressed as

$$\lambda_i = \frac{1}{n_n Q_{in}} \tag{7}$$

$$\gamma = \frac{T_e}{T_i} \tag{8}$$

$$D_i = \frac{kT_i}{m_i \nu_{in}} \tag{9}$$

In the expression of ion diffusion coefficient D_i shown in Eq. 9, the ion-neutral scattering frequency ν_{in} is found by the product of mean thermal velocity of ions, neutral particle density and ion-neutral scattering collision cross-section:

$$\nu_{in} = \bar{c}_i n_n \bar{Q}_{in} \tag{10}$$

The mean thermal velocity of ions are assumed to equal to the one of neutrals. The mean thermal velocities of ions and electrons are computed from their Maxwellian distributions:

$$\bar{c}_i = \bar{c}_n = \sqrt{\frac{8kT_i}{\pi m_i}}, \quad \bar{c}_e = \sqrt{\frac{8kT_e}{\pi m_e}} \tag{11}$$

The Maxwellain-averaged cross-section for Xenon ions scattering off a neutral background is taken from Banks' formula [10]

$$\bar{Q}_{in} = \frac{8.28072 \times 10^{-16}}{c_r} m^2 \tag{12}$$

where c_r is the relative velocity between two species. In this case, c_r is the relative velocity of singly-charged ions and background neutrals upon elastic collision. c_r is found by relating the mean thermal velocity of ions and neutrals with the reduced mass for the collision:

$$c_r = \sqrt{\frac{16kT_i}{\pi m_i}} \tag{13}$$

which is in the same order of the ion mean thermal velocity shown in Eq. 11. Now, by substituting Eqs. 11, 12 and 13 back into Eq. 10, the ion temperature is cancelled, which implies that the ion-neutral scattering frequency ν_{in} depends solely on background neutral density. This is a general feature of the "Maxwellian Collision" model adopted by Eq. 12.

The ionization frequency ν_i shown in the left-hand side of Eq. 1 is derived from the definition of ionization rate [9]

$$\dot{n}_e = \nu_i n_e = n_n \int_0^\infty f_e c \sigma_{ion.}(c) 4\pi c^2 dc \tag{14}$$

where f_e is the electron distribution function, c is the magnitude of the velocity and $\sigma_{ion.}(c)$ is the ionization cross-section. For T_e less than the first ionization energy (12.1 eV for Xenon), only a small group of electrons can have energy exceeding the ionization threshold [9]. For this condition, the integration of Eq. 14 needs to consider only the linear part of ionization cross-section near the threshold:

$$\sigma_{ion.}(E) = \sigma_0 (\frac{E}{eV_i} - 1) \tag{15}$$

where E represents the particle energy, eV_i represents the first ionization energy and the constant σ_0 relates to the linear slope of the ionization cross-section curve and is approximately the geometrical atomic cross-section. For Xenon, σ_0 is estimated as 3.63×10^{-20} m^2 from Figure 5. Now, since electrons are assumed to have a Maxwellian distribution

$$f_e = n_e (\frac{m_e}{2\pi k T_e})^{\frac{3}{2}} e^{-\frac{E}{kT_e}} \tag{16}$$

the integral in Eq. 14 can be carried out by integrating from the first ionization energy eV_i to infinity with respect to the kinetic energy $E = \frac{1}{2}mc^2$ to obtain

$$\dot{n}_e = \nu_i n_e = n_e n_n \sigma_0 \sqrt{\frac{8kT_e}{\pi m_e}} \left(1 + 2\frac{kT_e}{eV_i}\right) e^{-\frac{eV_i}{T_e}} \tag{17}$$

Having obtained Eq. 17, finally the ionization frequency can be shown as a function of electron temperature

$$\nu_i = n_n \sigma_0 \sqrt{\frac{8kT_e}{\pi m_e}} \left(1 + 2\frac{kT_e}{eV_i}\right) e^{-\frac{eV_i}{T_e}} \tag{18}$$

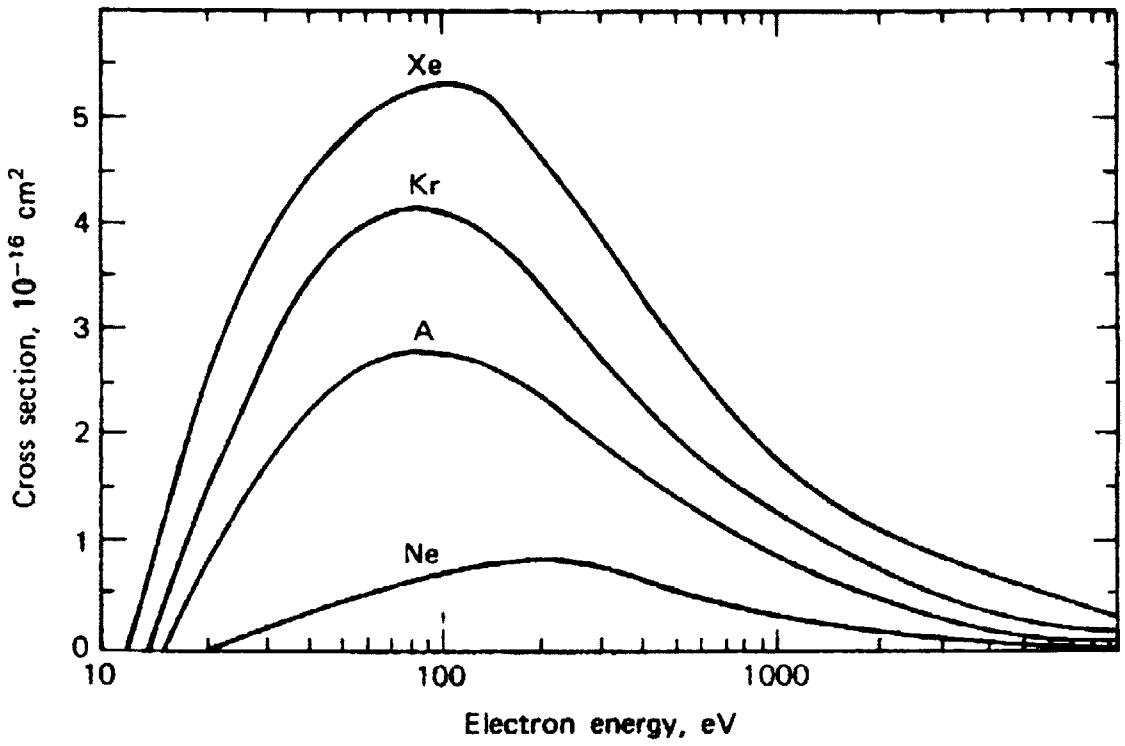

Figure 5: Total ionization cross-section of noble gases [12].

With the results of Eqs. 2, 3 and 18, it is now clear that if the wall temperature, chamber geometry and neutral particle density are specified, the electron temperature can be calculated from the ionization/diffusion relationship described in Eq. 1. Figure 6 shows this relationship between ionization and diffusion for a testing case described in Appendix C. In Figure 6, the

ionization curve represents the left-hand-side of Eq. 1 and the diffusion curve represents the right-hand-side. The intersection of the two curves indicates the solution for electron temperature. A solution of approximately 4 eV can be simply observed from Figure 6. A more accurate solution by the MATLAB computation code yields electron temperature of 3.98 eV. Operating conditions and calculated results for this particular test case can be found in Appendix C.

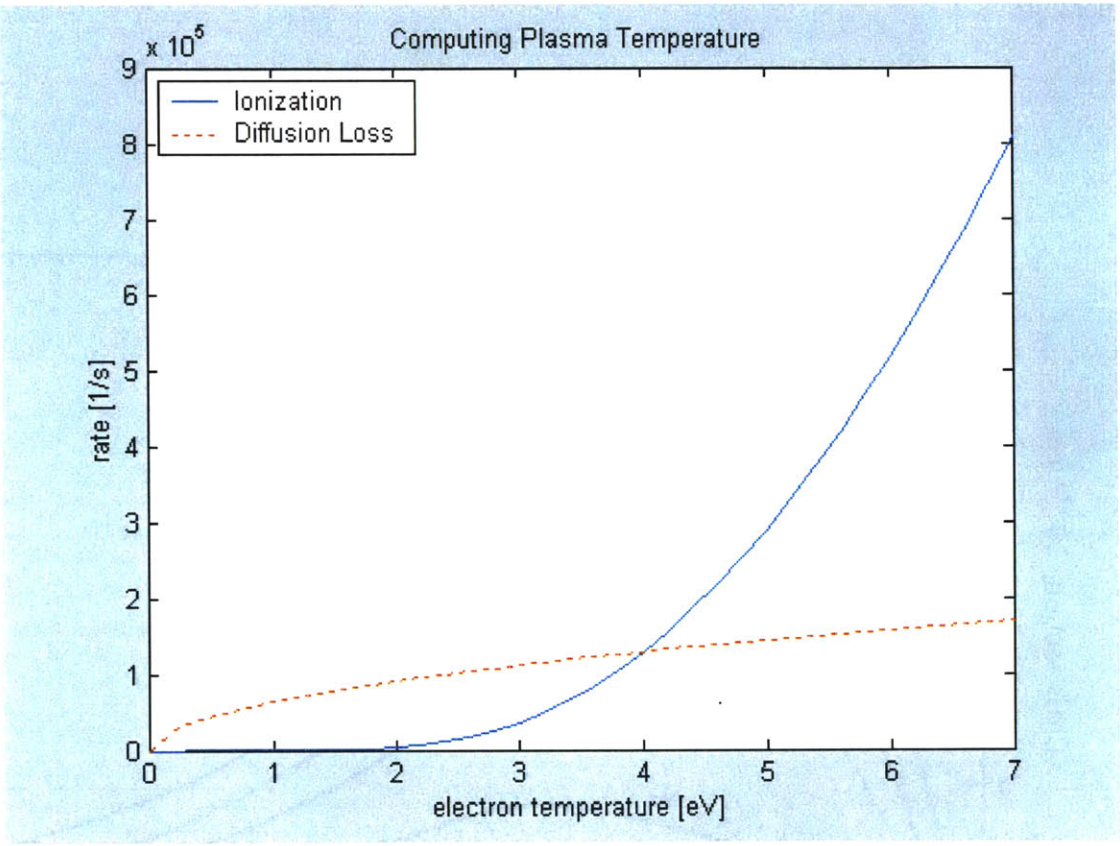

Figure 6: Solution for electron temperature from equating ionization and diffusion.

It should be noted that this solution method for electron temperature is not as straightforward as it may seem. First of all, it is not easy to relate the neutral particle density to adjustable operation parameters (i.e. mass flow rate or input power) since it is influenced by the ionization fraction. Adding to the difficulty, the neutral particle density in the ionization chamber cannot be measured directly in experiments because any pressure measurement made would be considered as total pressure:

$$p = n_e k(T_e + T_i) + n_n k T_n \tag{19}$$

Thus, even though the calculation of electron temperature may seem independent, it is actually coupled with many other variables. The equations shown in this section are useful only if the ionization fraction and chamber pressure are prescribed and the neutral density is known. In the computation code, this condition is satisfied by iterating ionization fraction and total chamber pressure.

2.2.2 Magnetic Field Penetration and Skin Effect

In ICP discharges, the magnetic field generated by the RF coil does not penetrate fully into the plasma except for conditions of low frequency (<< 1 MHz) or extremely low pressure (<< 1 mTorr) [9]. However, ICP discharges generally cannot be sustained under such conditions. The spatial decay constant of a normally incident electromagnetic wave within the plasma is defined as the "skin depth" of the plasma. The term "skin depth" does not refer to the absence of magnetic field beyond it; it merely characterizes the weakening of magnetic field in such high-frequency oscillation. Since the ICP discharge is ignited by the induced secondary electric field, a weakened magnetic field directly relates to insufficient ionization beyond the skin layer.

For high-pressure and high-density ICP discharges, the skin effect is strong and power is dissipated only within a thin ring of plasma near the wall. For ICP RF ion thrusters operating at low pressures (1~10 mTorr), the skin effect is weak and the skin depth is typically chosen to be about half of the inner radius. This particular size of skin layer makes intuitive sense; it indicates a balance between core plasma impeding the incident electromagnetic wave and ionization in the skin layer by the penetrating field. Calculation of the skin depth is made by modeling the core plasma as a conductor with conductivity

$$\sigma = \frac{e^2 n_e}{m_e \nu_{eff}} \tag{20}$$

where ν_{eff} is the effective elastic collision frequency. In a low-density plasma, where the ionization fraction is low, the effective elastic collision frequency is approximated by the electron-neutral elastic collision frequency,

$$\nu_{eff} \approx \nu_{en} = \bar{c}_e n_n \bar{Q}_{en} \tag{21}$$

where the mean electron thermal velocity of electrons $\bar{c}_e$ is defined in Eq. 11. The averaged electron-neutral cross-section for elastic collision, $\overline{Q}_{en}$, is calculated by taking the Maxwellian average of the atomic cross-section Q_{en} with respect to electron energy:

$$\overline{Q}_{en} = \frac{4}{3}\int_0^\infty e^{-\zeta^2}\zeta^5 Q_{en}\left(\zeta\sqrt{\frac{2kT_e}{m_e}}\right)d\zeta \tag{22}$$

The relationship between electron temperature and Q_{en} for a Xenon atom is obtained from Ref. 11 and is presented in Figure 7. It is observed that after Maxwellian-averaging, the temperature-dependent curve in Figure 7 flattens, and $\overline{Q}_{en}$ for Xenon approaches to the constant value of 1.933×10^{-19} m^2.

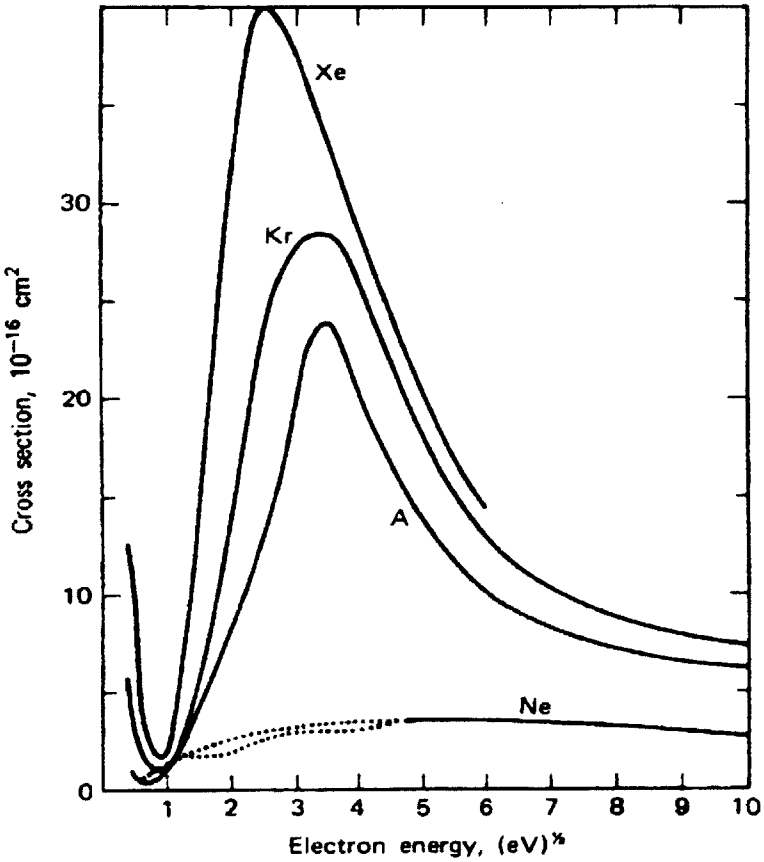

Figure 7: Atomic electron-neutral elastic collision cross-section of noble gases [11].

Assuming constant conductivity from the volume-averaged global discharge model and no Hall effect, the penetration of the magnetic field can be analyzed by solving the one-dimensional radial diffusion equation [9]

$$\frac{\partial \vec{B}}{\partial t} = D_m \nabla^2 \vec{B}, \quad D_m = \frac{1}{\sigma \mu_0} \tag{23}$$

where μ_0 is the permeability of free space. The factor D_m in Eq. 23 can be interpreted as a coefficient of diffusion of magnetic field into the plasma; sometimes it is also referred to as the magnetic viscosity [9].

In order to solve the above diffusion equation, a boundary condition must be established. By treating the coil current as a concentrated layer at the wall, the boundary condition at the surface can be derived from the solenoid field equation,

$$B_{r=R} = \mu_0 \frac{I_c N}{l} \tag{24}$$

where N is the number of turns, l is the coil length and I_c is the RMS current in the coil. Consider complex representations for the oscillating axial magnetic field and coil current,

$$B(r,t) = \mathrm{Re}\left\{\hat{B}(r)e^{i\omega t}\right\}, \quad I_c(t) = \mathrm{Re}\left\{\hat{I}_c e^{i\omega t}\right\} \tag{25}$$

Eqs. 23 and 24 can be rewritten as,

$$\begin{cases} \dfrac{1}{r}\dfrac{d}{dr}\left(r\dfrac{d\hat{B}}{dr}\right) - i\dfrac{\omega}{D_m}\hat{B} = 0 \\ \hat{B}_{r=R} = \mu_0 \dfrac{N}{l}\hat{I}_c \end{cases} \tag{26}$$

Expanding the first part of Eq. 26 yields the equation

$$\frac{d^2\hat{B}}{dr^2} + \frac{1}{r}\frac{d\hat{B}}{dr} - \frac{i\omega}{D_m}\hat{B} = 0 \tag{27}$$

With a change of variable, Eq. 27 becomes

$$\eta^2 \frac{d^2\hat{B}}{d\eta^2} + \eta\frac{d\hat{B}}{d\eta} - i\eta^2\hat{B} = 0, \quad \eta = \frac{r}{\sqrt{\dfrac{D_m}{\omega}}} \tag{28}$$

which can be related to the general form of a Kelvin function and does not require numerical solution. From Eq. 28, if considering the skin depth of plasma as a spatial decay constant for magnetic field penetration, then it makes sense to define the skin depth δ as

$$\delta = \sqrt{\frac{D_m}{\omega}} \tag{29}$$

The solution of Eq. 28 can then be written as [12]

$$\hat{B}(r) = \mu_0 \frac{N}{l} \hat{I}_c \frac{Mo\left(\frac{r}{\delta}\right)}{Mo\left(\frac{R}{\delta}\right)} e^{i\left[\theta\left(\frac{r}{\delta}\right) - \theta\left(\frac{R}{\delta}\right)\right]} \tag{30}$$

with

$$\text{Modulus, } Mo(x) = \sqrt{ber^2(x) + bei^2(x)}$$

$$\text{Phase, } \theta(x) = \tan^{-1}\left[\frac{bei(x)}{ber(x)}\right]$$

$bei(x)$ and $ber(x)$ shown in Eq. 30 are Kelvin functions and are defined as

$$\begin{aligned} ber(x) &\cong 1 - 64\left(\frac{x}{8}\right)^4 + 113.77777777\left(\frac{x}{8}\right)^8 - 32.36345625\left(\frac{x}{8}\right)^{12} + 2.64191397\left(\frac{x}{8}\right)^{16} \\ &- 0.08349609\left(\frac{x}{8}\right)^{20} + 0.00122552\left(\frac{x}{8}\right)^{24} - 0.0000901\left(\frac{x}{8}\right)^{28} \\ bei(x) &\cong 16\left(\frac{x}{8}\right)^2 - 113.77777777\left(\frac{x}{8}\right)^6 + 72.81777742\left(\frac{x}{8}\right)^{10} - 10.56765779\left(\frac{x}{8}\right)^{14} \\ &+ 0.52185615\left(\frac{x}{8}\right)^{18} - 0.01103667\left(\frac{x}{8}\right)^{22} + 0.00011346\left(\frac{x}{8}\right)^{26} \end{aligned} \tag{31}$$

valid for $-8 < x < 8$. The skin layer depth calculated from Eq. 29 is an important parameter because it affects electric resistance of the plasma, which couples with the coil current and can ultimately affect the percentage of RF power absorbed by the plasma. A model describing these relationships is presented in Section 2.3.

With the solution for magnetic field diffusion, the azimuthally induced secondary electric field can be easily calculated from Maxwell's Equation,

$$\nabla \times \vec{B} = \mu_0 \vec{j} = \mu_0 \sigma \vec{E} \tag{32}$$

where σ is the plasma conductivity defined in Eq. 20. For the one-dimensional case considered in this thesis, Eq. 32 can be simplified to

$$-\frac{dB_z}{dr} = \mu_0 \sigma E_\theta \tag{33}$$

Results of magnetic field $B_z(r)$ and induced secondary electric field $E_\theta(r)$ for the testing case described in Appendix C are plotted in Figure 8. The calculated depth of skin layer for this case is approximately 5.76 mm, which is 2/5 of the inner radius from the wall. From Figure 8, the skin depth can be observed in the profile of magnetic field penetration as a decaying characteristic. However, the presence of a skin layer is more obvious in the profile of the induced secondary electric field. Until about 6 mm distance from the wall, the induced electric field is strong and without significant decay, which validates the occurrence of ionization inside the skin layer.

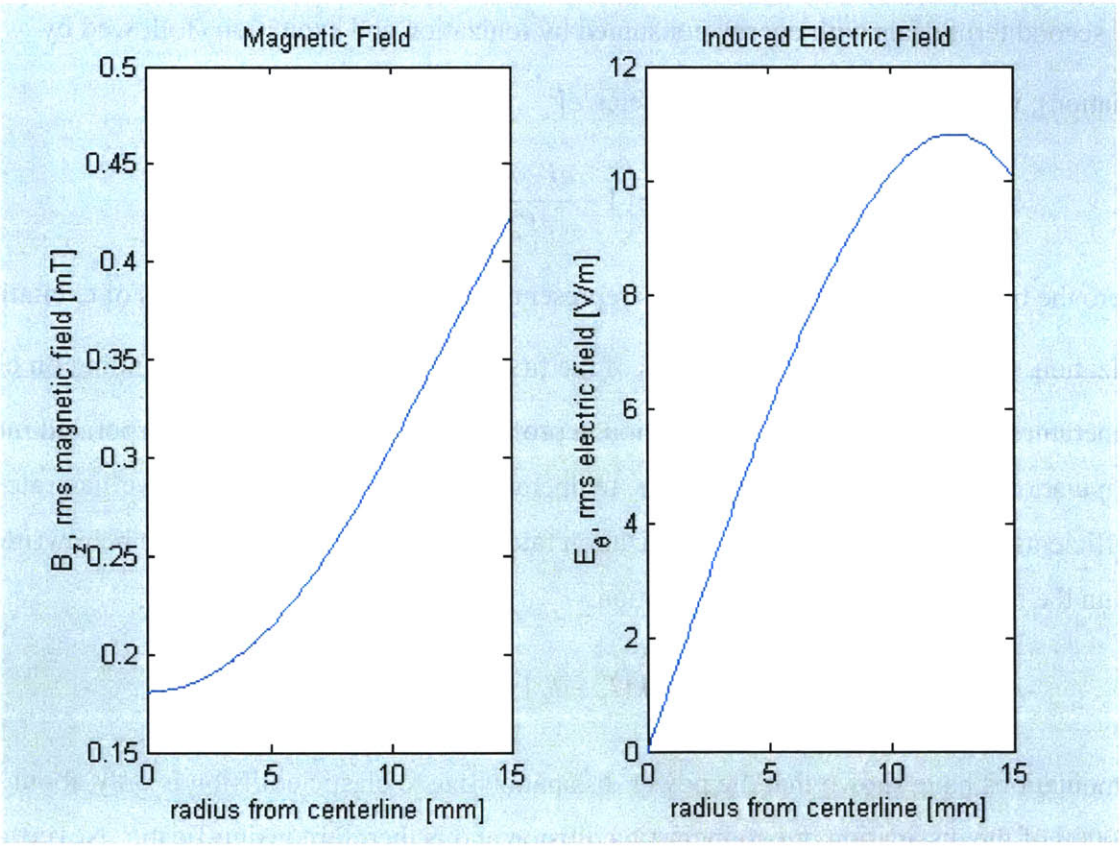

Figure 8: Profile of magnetic field and induced electric field inside an ICP discharge.

2.2.3 Energy Balance

In addition to the particle balance, an energy balance within the plasma is essential to describe the characteristics of an ICP discharge. The electron density, which does not appear in the particle balance equation, can be computed from this energy balance. Mitchner and Kruger [11] formulate an equation of energy balance by assuming that all the absorbed power is lost due to only elastic and inelastic collisions in the discharge,

$$\frac{P_{abs}}{V_{eff}} = n_e \nu_{en} \frac{3m_e}{m_n} k(T_e - T_n) + \dot{n}_e e V_i' \tag{34}$$

where ν_{en} is the electron-neutral collision frequency, $\dot{n}_e$ is the ionization rate, P_{abs} is the power absorbed by the plasma and V_{eff} is the effective discharge volume. Since the electron density is considered volume-averaged, the effective discharge volume is taken as the whole chamber volume. In Eq. 34, the first term of the right-hand-side describes power dissipation due to elastic collisions; in this case only the dominant electron-neutral elastic collisions are considered. The second term deals with energy consumed by ionization and excitation (followed by radiation); it is represented by the parameter eV_i' ,

$$eV_i' = \left(1 + \frac{eV_{exc}\langle \sigma c \rangle_{exc}}{eV_i \langle \sigma c \rangle_i}\right) eV_i \tag{35}$$

where the brackets inside the parenthesis represent Maxwellian rate coefficients of excitation and ionization. Generally eV_i' is 1.8~3 times of the first ionization energy eV_i depending on electron temperature. For more accurate calculation, a profile shown in Figure 9 is incorporated into the computation code to take into account the temperature dependence of the Maxwellian rate coefficients. From the derivation of ionization rate shown in Eq. 17, Eq. 34 can be rewritten to obtain the resultant energy balance equation,

$$\frac{P_{abs}}{V_{eff}} = n_e \nu_{en} \frac{3m_e}{m_n} k(T_e - T_n) + n_e \upsilon_i \left(1 + \frac{eV_{exc}\langle \sigma c \rangle_{exc}}{eV_i \langle \sigma c \rangle_i}\right) eV_i \tag{36}$$

Computations have shown that the power dissipation due to elastic collision is only about 1/10000 of the dissipation due to inelastic collision and is therefore insignificant. Nevertheless,

the elastic collision term shown in Eq. 36 is still carried out in the computation code for completeness.

With the use of Eq. 36, if the electron temperature and power are prescribed, the electron density can be calculated. The underlying problem is to calculate the power absorbed by the plasma, which can be influenced by both the electron temperature and density. In addition to an iterative method, a circuit analysis is needed in order to estimate the effect of chamber plasma on the primary circuit. By computing the plasma resistance and transforming such resistance into the primary circuit, its resistive power dissipation can be found. This particular resistive dissipation seen from the primary circuit is considered to be absorbed by the chamber plasma, and the computed value can be used in Eq. 36 for energy balance in the ICP discharge. The detailed description of this circuit analysis is presented in the next section.

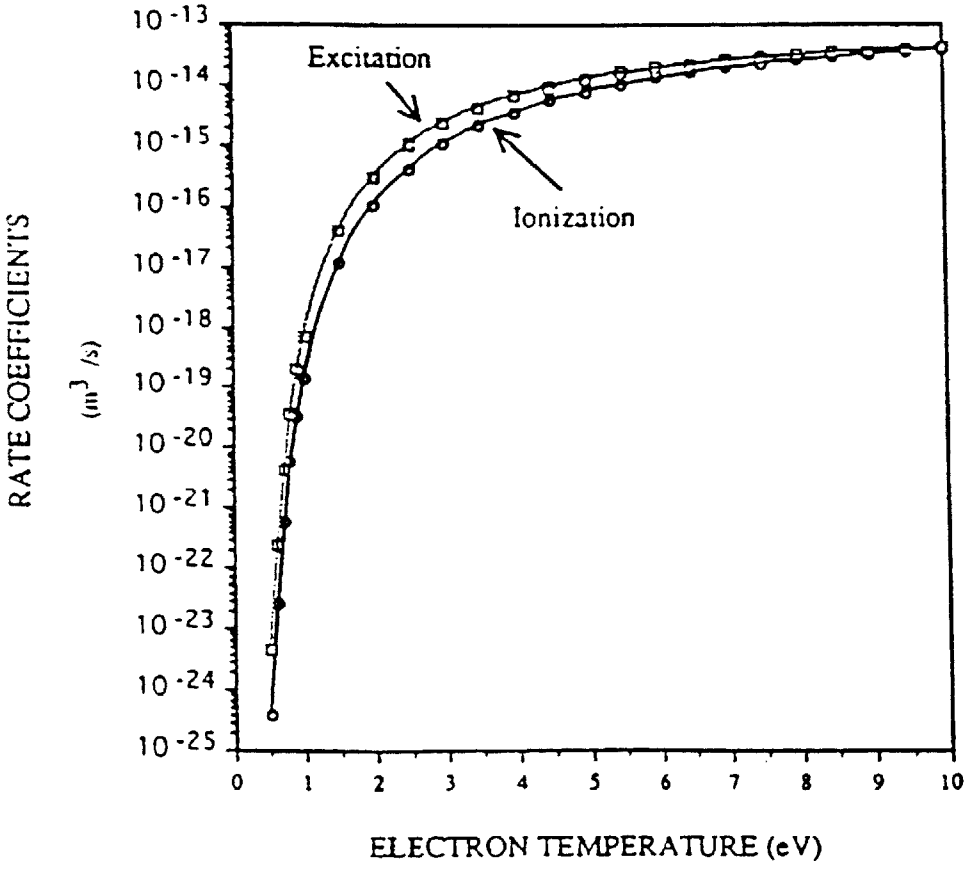

Figure 9: Maxwellian rate coefficients of Xenon [13].

2.3 Circuit Network Analysis

As discussed in the previous section, the purpose of the circuit analysis is to calculate the percentage of forward power that is absorbed by the plasma. This is done with a transformer model developed by Lieberman and Gottscho. Since some of the element properties for the cable, coil and capacitor are not given, a matching network analysis is developed to calculate the effect of these element properties on power reflection. In experiments, reflected power is measured instead of power absorbed by the plasma. Therefore, by comparing calculated power reflection with experimental data, circuit element properties can be estimated and the transformer model for computing absorbed power can be validated.

2.3.1 Transformer Model of an ICP Discharge

The idea of modeling an ICP discharge as a transformer with the plasma being a one-turn secondary coil is not new. A previous model developed by Lieberman and Gottscho is discussed in this section. Figure 10 shows the circuit diagram of such a model where a parallel LC network is used in the primary circuit for impedance matching. The main objective of this transformer model is to calculate the resistive power dissipation due to plasma loading, which is shown in Figure 11 as element R_2 in the equivalent circuit.

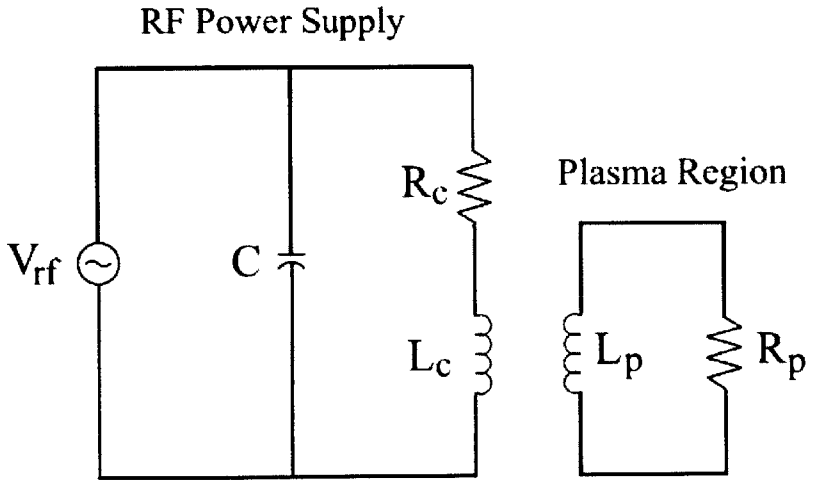

Figure 10: Circuit diagram of the transformer model. The primary circuit has capacitance C, coil resistance R_c and inductance L_c; the secondary circuit has plasma resistance R_p and plasma inductance L_p.

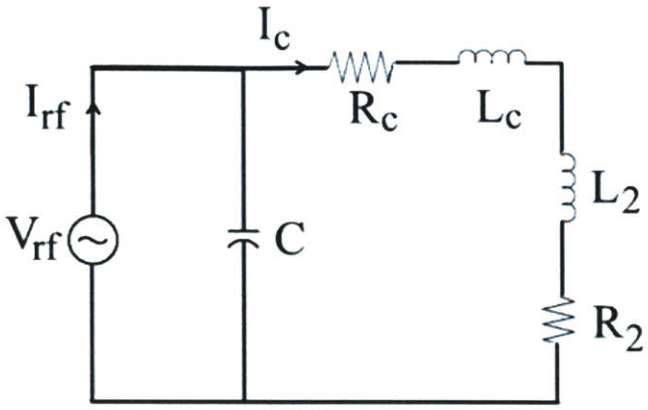

Figure 11: Equivalent circuit of the transformer model. The change of inductance in the primary circuit due to plasma loading is L_2 and the change of resistance is R_2.

In the transformer model described by Lierberman and Gottscho, the plasma resistance is related to the conductivity and skin depth [8]:

$$R_p = \frac{1}{\sigma}\frac{l_{path}}{A_{path}} = \frac{2\pi R}{\sigma l \delta} \tag{37}$$

where σ is the plasma conductivity, l_{path} and A_{path} are the effective circumference and cross-sectional area of the azimuthal current, respectively, and δ is the skin depth. The plasma self-inductance L_p consists of geometrical inductance and inductance arising from electron inertia; it can be approximated as [8]

$$L_p = L_{geometry} + L_{inertia} \cong \frac{\mu_0 \pi R^2}{l} + \frac{R_p}{\nu_{en}} \tag{38}$$

where ν_{en} is the electron-neutral elastic collision frequency for momentum transfer defined in Eq. 21. The definition of geometrical self-inductance has a N^2 term in the numerator; however, since the plasma is modeled as a one-turn secondary coil, $N^2 = 1$. Usually the inductance due to electron inertia is insignificant compared to the geometrical inductance because of the plasma's high electric conductivity. Assuming a perfect coupling between the primary coil and the secondary one-turn "air coil" of plasma, the mutual inductance can be expressed as [14]

$$L_m = \sqrt{L_c L_p} \tag{39}$$

where the self inductance of the N-turn primary coil is calculated as [15]

$$L_c = \frac{\mu_0 \pi R^2 N^2}{l} \tag{40}$$

By substituting Eq. 40 and Eq. 38 into Eq. 39 and ignoring the inertial inductance, the mutual inductance can be rewritten to obtain

$$L_m = \frac{\mu_0 \pi R^2 N}{l} \tag{41}$$

With the mutual inductance, the effects of plasma loading on the primary circuit can be evaluated by the transformer equations. The changes of resistance R_2 and inductance L_2 in the primary circuit due to plasma loading are given by [14]

$$R_2 = \frac{\omega^2 {L_m}^2 R_p}{{R_p}^2 + (\omega L_p)^2} \tag{42}$$

$$L_2 = -\frac{\omega^2 {L_m}^2 L_p}{{R_p}^2 + (\omega L_p)^2} \tag{43}$$

After the plasma loading is transformed to the primary circuit, the coil current I_c can be calculated from the impedance of the circuit elements. For the coil branch of the primary circuit, the complex impedance is expressed as

$$Z_1 = (R_c + R_2) + i\omega(L_c + L_2) \tag{44}$$

For the capacitor with capacitance C and equivalent series resistance (ESR), its impedance is written as

$$Z_2 = ESR - i\frac{1}{\omega C} \tag{45}$$

The RMS source voltage is then calculated by finding the total impedance Z of the primary circuit:

$$Z = \frac{Z_1 Z_2}{Z_1 + Z_2} \tag{46}$$

$$V_{s,RMS} = \frac{\sqrt{P_{rf}|Z|}}{\cos(\phi(Z))} \tag{47}$$

where P_{rf} is the forward power and $\phi(Z)$ is the phase of the total impedance.

Finally, the RMS power absorbed by the plasma can be estimated by calculating the resistive power dissipation due to element R_2 in Figure 11:

$$P_{abs} = I_{c,RMS}{}^2 R_2 = \left| \frac{V_{s,RMS}}{Z_1} \right|^2 R_2 \tag{48}$$

Having found the absorbed power, the energy balance equation for the ICP discharge model shown in Eq. 36 can be completed. Eq. 48 is ready for use if the coil resistance R_c and the ESR value of the capacitor are known. If these two values are not provided, more work is needed in order to calculate them. The procedure is shown in the next section.

2.3.2 Matching Network

The concept of impedance matching was originated by power companies for designing transmission lines, but it is valid for all devices that utilize an AC power source. The idea is to match the characteristic impedance of a transmission line to the load impedance in order to minimize standing waves and maximize deliverable power to the loads. The characteristic impedance of a transmission line is a property of the coaxial cable that describes both internal resistance and inductance. If there is a mismatch between the cable's characteristic impedance and the load impedance, a portion of the forward power is reflected back to the source. In experiments, this reflected power can be measured to examine the quality of the matching network.

As mentioned in the previous section, if the necessary coil resistance and capacitor ESR in the primary circuit are not known, they can still be calculated by measuring reflected power. The power reflection coefficient is defined as [16]

$$\rho = \frac{P_{reflected}}{P_{forward}} = \frac{V_{reflected}}{V_{forward}} = \frac{Z - Z_0}{Z + Z_0} \tag{49}$$

where Z_0 is the cable's characteristic impedance. By Eq. 49, the absent values along with Z_0 can be solved for after multiple entries of power reflection are recorded. This analysis ignores the effect of a possible mismatch of impedance between the source and the cable, which could send out a second reflection wave into the circuit. In this thesis, the power reflection measurement is assumed not severely influenced by the second reflection wave generated from

the source. The validity of this assumption would depend on how measurements are taken during the experiments.

2.4 Thruster Performance

Having obtained a global model for calculating bulk plasma properties in an ICP discharge, a model of ion extraction must be developed in order to predict the thruster's performance. A space-charge limited extraction model is presented in this section for predicting ion beam current. A separate subsection is devoted to equations for other performance parameters such as thrust, specific impulse and efficiencies. The ion extraction model is based on the configuration described in Section 1.5 with internal anode and floating screen; modifications are need for other anode placements.

2.4.1 Ion Extraction Capability

Since an ICP RF ion thruster relies on an electrostatic field for accelerating ions and generating thrust, it is essential to investigate the relationship between the applied grid potential and the extractable ion current. The objective is to develop a simple one-dimensional model that can predict such relationship. Figure 12 shows a simplified schematic of the two-grid acceleration system that is used in this project. Notice this system is a little different from the design of the German RIT-series thrusters, by placing anode internally instead of connecting to the screen. The screen is left floating in this configuration.

In Figure 12, the anode bias is also referred to as "net potential" because the electric field generated by this potential controls ion exit velocity. The role of the accelerator bias is to provide a negative potential with respect to the cathode in order to prevent electron back-streaming through the grids. The summation of the anode bias and the accelerator bias is often referred to as the "total potential" and it provides overall acceleration for ions before they are decelerated to the cathode potential. Total potential is a critical parameter for determining whether or not the ion beam current is saturated. The ratio between the net and total potential, denoted R, is also an important parameter for investigating ion extraction capability of the

acceleration grids. Typically the value of R is designed below 0.9 to prevent electron back-streaming, but above 0.5 in order to maintain satisfactory performance.

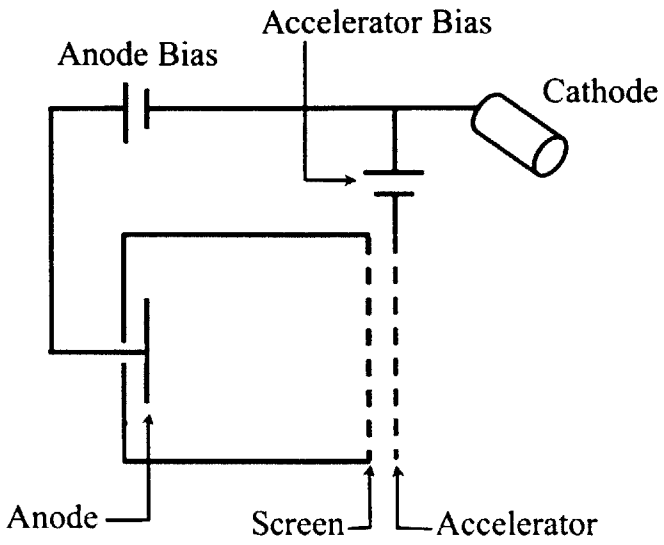

Figure 12: Simplified schematic of the acceleration system.

V_{net} = Anode Bias, V_{total} = Anode Bias + Accelerator Bias, and $R = \frac{V_{net}}{V_{total}}$

Child-Langmuir's theory states that the ion beam current is limited by the inter-grid space-charge. By this classical definition, the extractable ion current density of the two-grid acceleration system automatically reaches its maximum with any applied total potential. This current density can be found in numerous publications, such as Ref. 17:

$$j_{beam} = \frac{4\sqrt{2}}{9}\varepsilon_0\left(\frac{e}{m_i}\right)^{\frac{1}{2}}\frac{V_{total}^{\frac{3}{2}}}{l_g^{\ 2}} \tag{50}$$

where ε_0 is the permittivity of free space and l_g is the grid spacing. The classical Child-Langmuir theory is valid when there is sufficient ion production in the chamber. However, this condition is rarely satisfied in a typical ion thruster (DC or RF). Because of low ionization fraction, the ion density in the chamber of a typical ion thruster is almost always below the requirement for achieving the classical Child-Langmuir space-charge limited current. The data provided by Ref. 18 illustrates that even a high-power DC ion thruster designed by the Jet

Propulsion Laboratory (JPL) cannot produce such level of limited current. The exact level of exactable current depends on grid spacing as well as aperture size. It is worth mentioning that the density in a typical ion thruster is not extremely low as to be indifferent to extraction potential.

Being unable to apply the classical Child-Langmuir theory for predicting ion beam currents, an alternative approach is taken. From literature research, interesting experimental results published by Rovang and Wilbur of Colorado State University in the 1980s were found. For their experiments, Rovang and Wilbur utilized an 8 cm diameter DC ion thruster with various grid configurations to investigate ion extraction capabilities of two-grid acceleration systems. Figure 13 shows an example of their findings, in which perveance is plotted against grid spacing. Since perveance is defined to have the unit of $A/V^{3/2}$, it can serve as an indicator of space-charge effect by its resemblance to Eq. 48.

From the experimental results leading to Figure 13, Rovang and Wilbur concluded that although the physics of ion extraction is very complicated and nonlinear with closely-spaced grids, they do become much simpler when the grid spacing is above 0.6 (normalized by diameter of screen hole) [19, 20]. In fact, when the grid spacing is larger than 0.6 and the potential ratio R is above 0.5, the measured perveance approaches a constant, indicating the extracted ion current has saturated by some space-charge effect. In order to investigate this phenomenon, effects of grid geometry are also studied from other previous experimental findings.

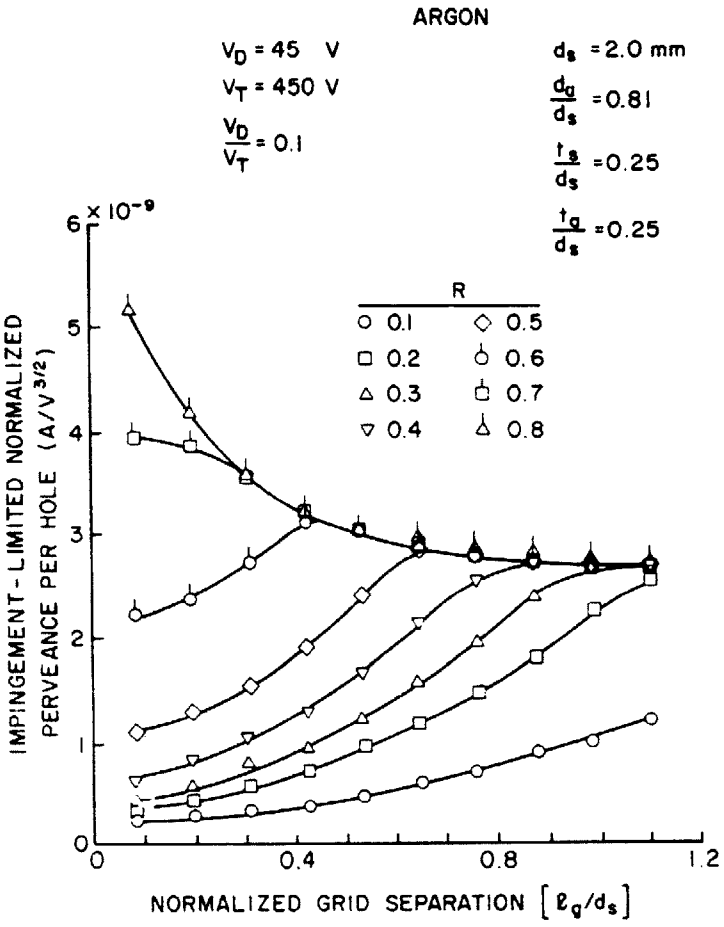

Figure 13: Experimental results regarding ion extraction capability of two-grid systems [20].

2.4.2 Modified Child-Langmuir Theory

During other experiments on the same DC ion thruster but with varying discharge-to-total voltage ratio, Rovang and Wilbur once again observed constant perveance, which implies space-charge limited current. The classical Child-Langmuir theory does not fully apply in this case because of low plasma density. However, the limitation on extractable beam current does somehow obey the classical theory, if a new spacing parameter is used in Eq. 50. Here, the name of "Modified Child-Langmuir Theory" is given to describe such technique and to distinguish from the original theory that uses physical grid spacing for calculating space-charge limited current.

Rovang and Wilbur noticed the level of limited ion beam current decreases with higher discharge-to-total voltage ratio [20]. This finding was furthermore investigated by Brophy in his research on DC ion thrusters. Brophy concluded that the level of beam current actually follows an inverse relationship with the potential drop between plasma and screen [21]. Brophy's conclusion is important because the plasma-to-screen potential drop is proportional to sheath size, suggesting that sheath size should take part in the effective length for the modified space-charge limitation theory.

It is apparent that the strength of electric field in closely spaced grids could reach breakdown value; therefore, there exit limits of applied grid voltage as well as grid spacing. Electric breakdown is highly undesirable because it not only damages grids but also impedes ion extraction. Before reaching the extreme values, increased accelerating voltage and decreased grid spacing generally increases the extracted ion beam current. In addition to these two parameters, grid geometry can also affect the level of space-charge limited current. According to Rovang and Wilbur, other effects of grid geometry on ion extraction capability can be summarized as [19, 20]:

- Ion beam current is directly related to the ratio of accelerator-to-screen hole diameter, d_a/d_s, until the ratio approaches unity. However, increasing d_a/d_s ratio would increase beam divergence as well.
- The diameter of the screen holes by itself does not have significant effect on ion beam current, as long as it is within reasonable size compared to the sheath size.
- The thickness of the accelerator grid has no apparent effect on ion extraction.
- There exists a consistent trend of decreased ion beam current with increased thickness of the screen grid.

Combining the findings of Brophy, Rovang and Wilbur, a new spacing parameter that is applicable to Eq. 50 is hypothesized to exist between the sheath edge of the chamber plasma and the upstream-side of the accelerator grid. Figure 14 illustrates such geometry. This effective length is expressed as

$$l_e = \beta l_s + t_s + l_g \tag{51}$$

where l_s is the sheath size, t_s is the screen thickness, l_g is the parallel grid spacing and β is a "shape factor" that represents the effective distance between the screen grid and the edge of the chamber plasma. The size of the sheath is calculated by assuming that $n_e << n_i$ in the sheath and the ions are being space-charge limited by the plasma-to-screen potential drop $\Delta\phi_s$:

$$j_i = \frac{4\sqrt{2}}{9}\varepsilon_0\left(\frac{e}{m_i}\right)^{\frac{1}{2}}\frac{\Delta\phi_s^{\frac{3}{2}}}{l_s^{\,2}} \tag{52}$$

The ion current density is provided by the chamber plasma,

$$j_i = e(h_L n_e)u_B \tag{53}$$

By equating Eq. 52 and 53 and rearranging, the sheath size can be expressed as

$$l_s = \left[\frac{4\sqrt{2}}{9}\frac{\varepsilon_0 kT_e}{e^2 h_L n_e}\left(\frac{e\Delta\phi_s}{kT_e}\right)^{\frac{3}{2}}\right]^{\frac{1}{2}} \tag{54}$$

The potential drop between plasma and the floating screen grid is calculated with the theory of floating probes. Because a floating probe collects no charge, the fluxes of electrons and ions are equal:

$$\gamma_e = \gamma_i = h_L n_e u_B \tag{55}$$

The floating screen is charged negatively with respect to the plasma due to high thermal energy of electrons; therefore, electrons are repelled from the wall and the flux is expressed as [13]

$$\gamma_e = \frac{n_e \bar{c}_e}{4} e^{\frac{-e\Delta\phi_s}{kT_e}} \tag{56}$$

Equating Eq. 55 and 56 and rearranging, the potential drop is obtained:

$$\Delta\phi_s = \frac{kT_e}{e}\ln\left(\frac{\sqrt{8/\pi}}{4h_L}\sqrt{\frac{m_i}{m_e}}\right) \tag{57}$$

and the calculation of sheath size in Eq. 54 is completed.

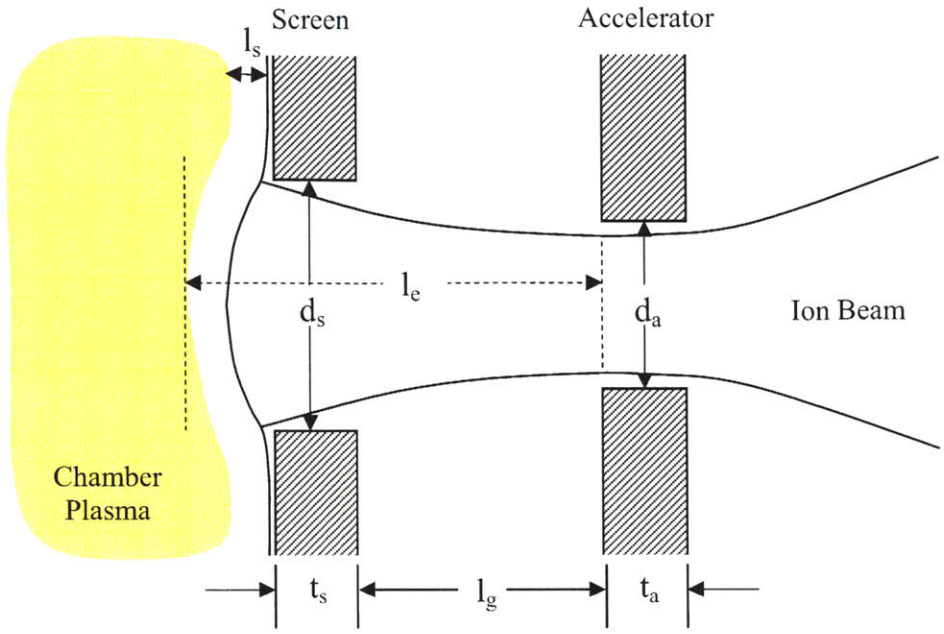

Figure 14: Ion beam optics and grid geometry.

In Eq. 51, since density distribution at the sheath edge is highly non-uniform and non-linear, it is necessary to define the shape factor β in order to take into account the influence of sheath size while maintaining accuracy of the 1-D extraction model. The shape factor β is estimated as 2.5 from experimental data for the internal anode configuration. It may take on different value with other anode placements that result in different shapes of the plasma sheath. For the purpose of simplicity, the shape factor is assumed to be constant regardless of applied accelerating potential. This assumption is a little crude since the sheath shape does change with respect to accelerating potentials. However, by defining the shape factor in the operational range of accelerating potential, the approximation of constant shape factor is not too far off. With the effective length found, the modified Child-Langmuir theory of space-charge limited ion beam current can now be written as

$$J_{beam} = \frac{4\sqrt{2}}{9}\varepsilon_0\left(\frac{e}{m_i}\right)^{\frac{1}{2}}\frac{V_{total}^{\frac{3}{2}}}{l_e^{\,2}}(\pi\frac{d_a^{\,2}}{4})N_{holes} \tag{58}$$

where d_a is the diameter of accelerator hole and N_{holes} means the number of grid holes.

2.4.3 Calculation of Propulsive Performance

Having obtained the ion beam current from the modified Child-Langmuir theory, total ion flux Γ_i and grid transparency ϕ_i can be calculated by their definition:

$$\Gamma_i = \frac{J_{Beam}}{e}, \quad \phi_i = \frac{J_{Beam}}{e\left(h_L n_e u_B A_{grid}\right)} \tag{59}$$

where A_{grid} is the screen area and $h_L n_e$ is the ion density at the sheath edge. The total ion flux can be used to calculate utilization efficiency with the equation [13]

$$\eta_u = \frac{\Gamma_i}{\Gamma_n + \Gamma_i} \tag{60}$$

where Γ_n is the total flux of neutral particles leaving the grids and is related to the Maxwellian neutral density as well as the mean thermal velocity of neutral particles:

$$\Gamma_n = \frac{n_n \bar{c}_n}{4} \phi_n A_{grid} \tag{61}$$

In Eq. 61, ϕ_n represents the overall grid transparency for neutrals. It is a physical property of the grids and can be designed to minimize loss of neutral propellant gas. The overall neutral transparency is calculated as

$$\phi_n = \frac{1}{1/\phi_s + 1/\phi_a - 1} \tag{62}$$

where ϕ_s and ϕ_a are the physical open area fractions of the screen and accelerator, respectively. Since utilization efficiency refers to the fraction of the discharge propellant flow that leaves as beam ions, it can be used to calculate the required input flow rate for sustaining the discharge pressure [13]:

$$\dot{m} = \frac{m_i J_{beam}}{e \eta_u} \tag{63}$$

The purpose of calculating this "required mass flow rate" is to ensure consistency between mass flows in and out of the thruster for the condition of constant chamber pressure.

Since the neutral particles are not affected by the electrostatic field generated by the accelerating grids, they escape from the system through random motion carrying an exit velocity equivalent

to their mean thermal velocity. Thrust, symbolized as T, is therefore contributed by both the ion beam and the escaped neutral particles:

$$T = m_i \Gamma_i C_i + m_n \Gamma_n \bar{c}_n \tag{64}$$

where C_i is the exit velocity of the accelerated ions and is related to the anode bias (net potential):

$$C_i = \sqrt{\frac{2eV_{net}}{m_i}} \tag{65}$$

Specific impulse, $Isp = C_{eff}/g$, is calculated with the use of a simple rocket equation,

$$T = \dot{m} C_{eff} \tag{66}$$

where C_{eff} is the effective exit velocity. The value of C_{eff} is lower than the ion exit velocity C_i due to the presence of slow neutral particles in the exit jet stream. Since the exit mass flow rate consists of both ion and neutral flows, the effective exit velocity can be computed from Eq. 64 as

$$C_{eff} = \frac{T}{\left(m_i \Gamma_i + m_n \Gamma_n\right)} \tag{67}$$

2.4.4 Calculation of Thruster Efficiencies

Four efficiencies of the RF ion thruster are defined in this section: ultimate propulsive efficiency, electrical efficiency, overall electrical efficiency and coupling efficiency. The ultimate propulsive efficiency defined here is different than the propulsive efficiency defined for air-breathing jet engines; it is calculated by assuming no power consumption by circuit elements and a perfect coupling between the RF power source and the plasma (100% power delivery). The ultimate propulsive efficiency is the best possible efficiency of a RF ion thruster because it does not account for any energy loss outside of the ionization chamber. It is expressed as the ratio between the beam power and the sum of beam power and absorbed power:

$$\eta_{up} = \frac{P_{beam}}{P_{beam} + P_{abs}} \tag{68}$$

where the beam power is calculated by

$$P_{beam} \cong J_{beam} \times V_{net} \tag{69}$$

Even if the resistive dissipation by circuit elements is minimized to negligible amount, the ultimate propulsive efficiency is still difficult to obtain because of the matching problem. Perfect matching can only be achieved for fixed values of forward power, frequency and flow rate. Any deviation from these fixed values would change the resistance and inductance of the plasma, causing an impedance mismatch. Since adjustability is a desirable feature of such a propulsion device, it makes no sense to pursue absolutely perfect matching and therefore the ultimate propulsive efficiency is not very practical.

Electrical efficiency is a more useful quantity because it accounts for the inevitable power reflection as well as the resistive loss in the capacitor and RF coil. It is expressed as

$$\eta_e = \frac{P_{useful}}{P_{total}} = \frac{P_{beam}}{P_{beam} + P_{rf}} \tag{70}$$

where P_{rf} is the forward RF power of which P_{abs} is only a fraction. The electrical efficiency is sometimes expressed in terms of energy cost per beam ion production, ΔV_{loss} (often denoted as ε_B),

$$\eta_e = \frac{V_{net}}{V_{net} + \Delta V_{loss}} \tag{71}$$

in which the ion production cost is found by

$$\Delta V_{loss} = \frac{P_{total} - P_{useful}}{J_{beam}} = \frac{P_{rf}}{J_{beam}} \tag{72}$$

ΔV_{loss} (or ε_B) is a commonly used parameter for characterizing thruster efficiency. It has the energy units of V or W/A. Values of ΔV_{loss} below 400 V are generally considered acceptable, if not satisfactory. In this thesis, the ion production cost is related to the electrical efficiency. However, sometimes it can also be related to overall electrical efficiency. The overall electrical efficiency is a measure of all power consumption within the system that does not contribute to propulsion. In addition to power reflection due to impedance mismatch, non-propulsive energy is consumed by the circuit elements, the neutralizer and the accelerator grids. Power loss due to DC/RF conversion in the RF power generator is sometimes considered as well. The coupling efficiency simply describes the percentage of forward power that is delivered to the plasma.

As mentioned before, the general problem of obtaining high efficiency in a RF ion thruster is the difficulty of delivering power to the plasma. For example, the highest electrical efficiency observed in the Phase I experiments was no more than 60%. Maximum power delivery to plasma (coupling efficiency) is around 50% of the forward power by calculation. The rest of forward power is either reflected back to the source due to circuit mismatch, or lost to resistive dissipations in the capacitor and RF coil. By inspection, if the matching network can deliver 80% of the forward power to the plasma, the electrical efficiency can be increased to 68%. Notice these efficiency values are not fixed as they can be increased with optimization. Further discussion on efficiency can be found in Chapter 4.

Chapter 3

Computation Code

3.1 Overview

This chapter outlines the flow of the MATLAB computation code that was developed to solve the performance model described in Chapter 2. The main executable function is named "RF_Model.m" and is included in Appendix B along with other sub-functions, which appear in the order of their usage. "RF_Model.m" takes flow rate, wall temperature, forward power, source frequency, anode bias and accelerator bias as input and outputs bulk plasma properties and thruster performance. A manual for using "RF_Model.m" is included in Appendix A and an example of output is shown in Appendix C. Geometrical parameters of the experimental setup are set as default in this code.

3.2 Calculation of Plasma Properties

In all parts of the computation code, electron temperatures are presented in energy units. Therefore, equations involving electron temperature may look slightly different than the ones in the theory section because of the difference in electron temperature's units. A simple conversion is used

$$T_e[eV] = \frac{kT_e[K]}{e} = \frac{T_e[K]}{11594} \tag{73}$$

where k is the Boltzmann's constant and e is the electron charge.

In "RF_Model.m," an iterative method is used to achieve overall particle and energy balance for the chamber plasma. Ion extraction is also incorporated in this iterative process. The outcome of the iterations is simultaneous solutions for chamber plasma properties and thruster performance. Figure 15 shows the computation scheme that is used to solve for the three major plasma properties: electron temperature, ionization fraction and chamber pressure. Other important properties such as particle density and wall-loss rate are calculated subsequently after these three

major values are found. In Figure 15, red color indicates the major concepts described in Chapter 2, and blue color indicates the path of iteration. An iterative process is needed because the three desired plasma properties cannot be directly related to adjustable operational parameters. It should be noticed that the order of the iterative loops must be the same as the one shown in Figure 15; otherwise the iterations could fail. This observation is the result of numerous trials and debugging for failures in convergence. It should also be advised that the code does not work too well for extremely low flow rates (i.e. below 0.1 sccm). This limitation is caused by the initial value of chamber pressure. Since the thruster does not usually operate in such low flow rates, no further debugging was conducted.

Iterations are terminated at some tolerance between two consecutive iterative results. The default tolerance for electron temperature convergence is 0.01 eV and for ionization fraction is 0.0005 (0.05%). Since ionization fraction is iterated at the outermost loop, the difference between two consecutive iterations in ionization fraction is referred to as the "convergence index" and is outputted to monitor the overall convergence. In the innermost loop of the iterative process, chamber pressure is updated via an algorithm that takes into account the difference between input and required mass flow rate. During each turn, an initial chamber pressure is guessed and the computation is carried out all the way through an ion extraction model shown in Figure 16, where a required flow rate for sustaining such chamber pressure is calculated. This "required flow rate", shown in blue color in Figure 16 to represent an iterative quantity, is then compared with the input mass flow rate, and the chamber pressure is updated until the difference between these two flow rates is less than 0.01 sccm. Decreasing the default tolerance values could result in increased iteration time or possible non-convergence.

3.3 Solution for Electron Temperature

Computation of electron temperature, as discussed in Section 2.2.1, is done with the use of Newton's method. Newton's method, written as

$$x_{n+1} = x_n - \frac{f(x_n)}{f'(x_n)} \tag{74}$$

is an iterative process for finding an accurate root of an equation $f(x_n) = 0$. In this case, the desired function is derived from the ionization/diffusion relationship seen in Eq. 1:

$$f(T_e) = \nu_i(T_e) - \frac{u_B(T_e)}{d_{eff}(T_e)} \tag{75}$$

In order to prevent convergence to other possible roots, the initial guess is set at 5 eV because the electron temperature in a typical ion thruster is around the vicinity of 5 eV. Accuracy of convergence is verified visually with plots similar to Figure 6. Codes for the Newton iteration, the convergence function and the function derivative are presented in Appendix B.2 through B.4.

3.4 Collision Cross-Section and Maxwellian Rate Coefficient

Although this computation scheme is supposed to work with all kind of propellants, the coded version is limited to Xenon only. The main limitations are the predefined and temperature-dependent functions of electron-neutral collision cross-section and Maxwellian rate coefficient (Appendix B.5 and B.7). These sub-functions are specifically made for Xenon and need to be replaced if other type of propellant is chosen. The Maxwellian rate coefficient refers to the ratio between excitation and ionization rate, and it is temperature-dependent. The basis for calculating the Maxwellian rate coefficient for Xenon is presented in Figure 9, Section 2.2.3. For electron temperatures above 9 eV, the Maxwellian rate coefficient is approximately equal to the ratio between first excitation energy and first ionization energy. The source for finding the electron-neutral scattering cross-section for Xenon is from Figure 7, Section 2.2.2. The data of atomic cross-sections in Figure 7 are used to calculate the Maxellian-averaged scattering cross-sections.

3.5 Calculation of Thruster Performance

Calculations for ion beam current are made in the sub-function named "Extraction.m" through a choice of extraction model depending on the level of ion source density. Performance values such as thrust, specific impulse and electric efficiency are calculated in the main program after the ion beam current is found in the sub-function. As discussed in Section 3.2, these performance values are coupled with calculations of plasma properties through the "required flow rate" and are therefore included in the iterative process. This coupling relationship can be

found in the flowcharts shown in Figure 15 and 16. As a result, thruster performance is automatically calculated when the iterations in "RF_Model.m" are terminated and the plasma properties are determined.

In the sub-function "Extraction.m," choices of ion extraction model shown in Figure 16 include both classical and modified space-charge limited current models. The classical model refers to the Child-Langmuir space-charge limited law between two parallel plates with applied potential. This model is rarely used because it implies that the beam current is space-charge limited by the physical grid spacing; ion density in a typical ion thruster is not high enough to satisfy such condition. Instead, the modified space-charge limited current model described in Section 2.4.2 is used most of the time. Nevertheless, both extraction models are included in this sub-function. Codes for "Extraction.m" are attached in Appendix B.8.

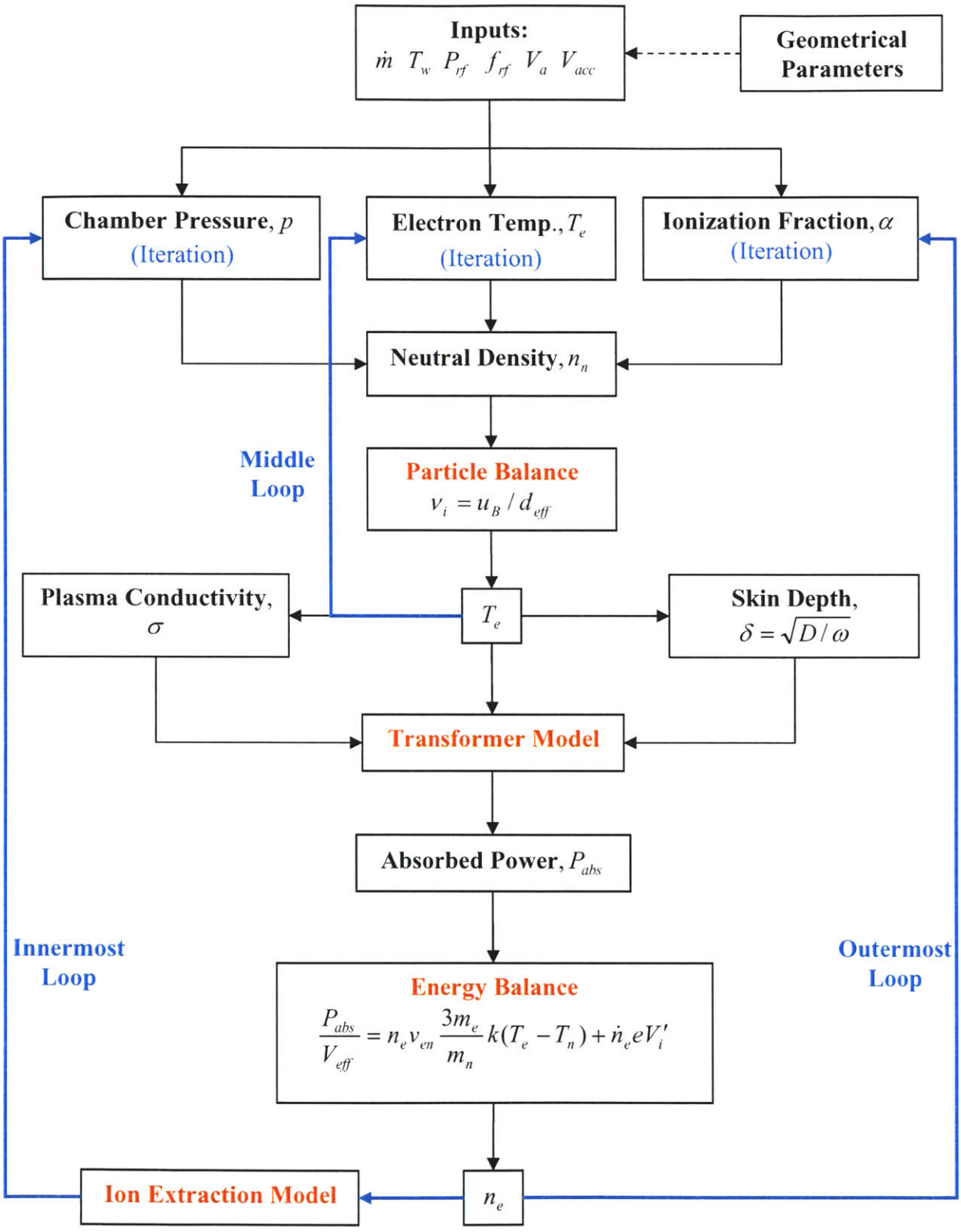

Figure 15: Flowchart of ICP discharge model in RF_Model.m.

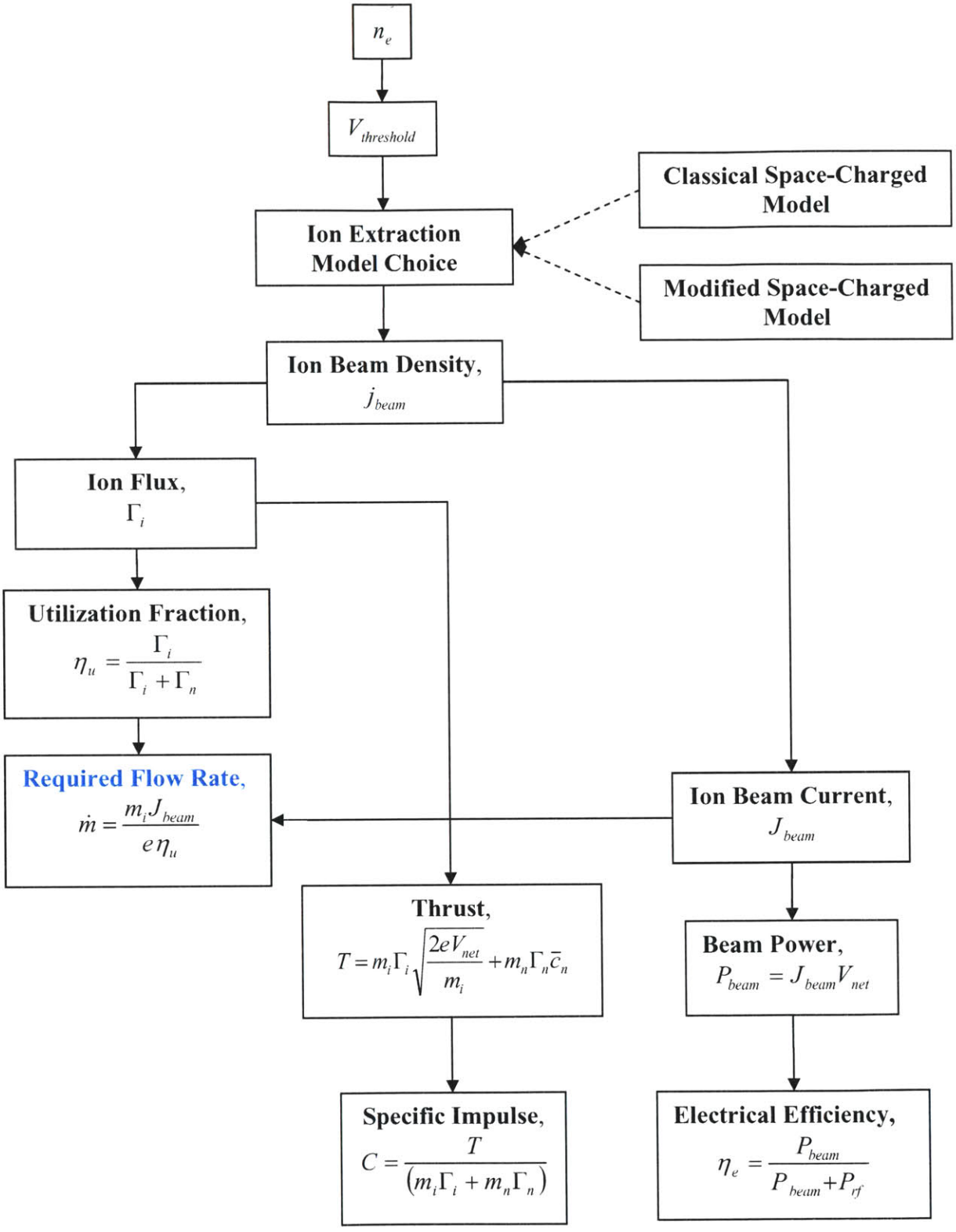

Figure 16: Flowchart of the ion extraction model.

Chapter 4

Results

4.1 Overview

Computation results are compared with available experimental data obtained from Busek Co. in this chapter. These data were generated with varying anode-bias voltages under fixed accelerator bias of 175 V, flow rate of 1 sccm Xenon, driving power of 27 W and source frequency of 1.41 MHz. Although separate power supplies were used for ionization and acceleration in the experiments, the micro thruster in whole does not consume more than 100 W of power. After validating the computation code, more computation results as well as prediction of thruster performance are presented. Discussions on the findings are included at the end of the chapter.

4.2 Comparison with Experiments

One set of experimental data of anode current, beam power and utilization efficiency were provided by Busek Co. During the experiments, measurements on electron density and temperature were not taken, thus plasma properties calculated by the ICP discharge model cannot be fully validated. In addition, the temperature of the chamber wall was not measured and is only estimated between 350 K and 500 K. Since ions and neutrals are assumed to attain wall temperature in the computation code, a preliminary estimation on the wall temperature must be made in order to carry out the calculations. Computation results seen in this section, unless noted, are obtained with the assumption of 400 K wall temperature. The validity of this assumption will be investigated by examining the sensitivity of the computation result to changes of wall temperature within the estimated temperature range.

4.2.1 Ion Beam Current

The performance of an ion thruster, such as thrust and specific impulse, can be characterized by its ion beam current because the accelerated ions carry much more exit momentum than the escaped neutrals (Eq. 59 to Eq. 67 in Section 2.4.3). However, measuring the ion beam current

directly is not an easy task; instead, anode current is measured during experiments. Ideally the anode current is equal to the extracted ion beam current. This condition is not satisfied when there is significant current being collected at the accelerator grid as the result of ion impingement. If the accelerator current is observed, then the anode current is equal to the sum of the exit beam current and the accelerator current as shown in the circuit connection in Figure 12, Section 2.4.1.

The classical Child-Langmuir beam current is plotted in Figure 17 in comparison with the experimental and the computation results. It is clear that the plasma density in the ionization chamber is not sufficient to produce the limited ion current calculated by the classical Child-Langmuir definition. Figure 18 shows the close-up comparison between the experimental and the theoretical anode currents under a fixed accelerator bias of 175 V. The experimental data, shown in blue color, are limited at the highest anode bias of 900 V due to the presence of inter-grid dielectric breakdown. The two small peaks at 600 V and 800 V are deemed experimental glitches and are not further discussed. The theoretical anode current, shown in red color, is assumed the same as the beam current and is calculated by the ion extraction model described in Eq. 51 and Eq. 58. The "shape factor" β in Eq. 51 for this thruster configuration takes the value of 2.5; it is derived by deliberately placing the theoretical current approximately 5% below the measured value in the anode-bias range between 800 V and 900 V. This shift is included to account for the experimental observation of electron back-streaming that may cause a slight over-measurement. Electron back-streaming in this case refers to electrons finding their way into the circuit through unprotected bolts of the accelerator grid that are exposed to the downstream electrons. No electron back-streaming through the grids is apparent, because the potential at the accelerator gird is sufficiently lower than the potential at the external cathode.

Similarity in trends between the experimental and theoretical anode currents can be observed in Figure 18, which validates the modified Child-Langmuir theory described in Section 2.4.2. However, some discrepancy is noticed toward the low end of anode-bias voltages (200 V to 400 V). This discrepancy is due to the presence of the accelerator current, caused by low-velocity and unfocused ions impinging on the accelerator grid. Ion impingement not only impedes overall extracted beam current, but also dislodges atoms from the surface of the accelerator grid

and causes grid erosion. The amount of accelerator current collected during the experiments is shown in Figure 19.

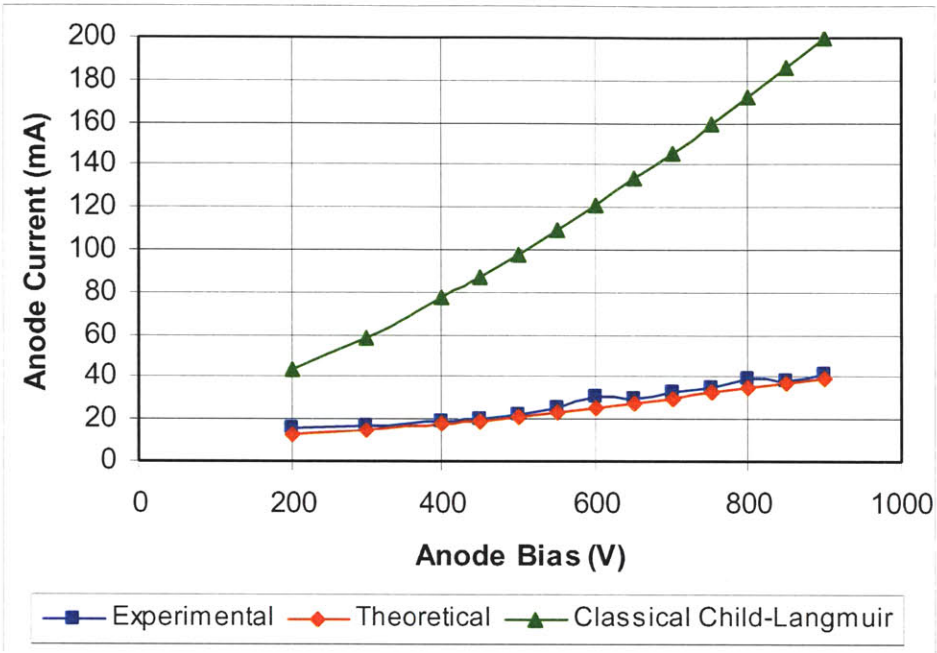

Figure 17: First comparison between theoretical and experimental anode currents.

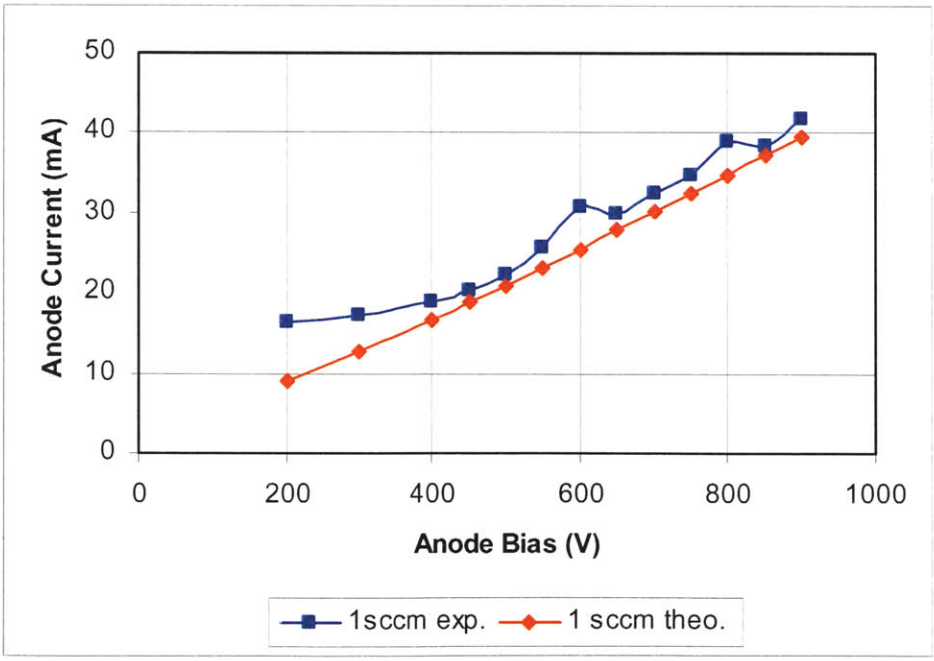

Figure 18: second comparison between experimental and theoretical anode currents. Theoretical anode current is obtained by assuming equality with theoretical ion beam current.

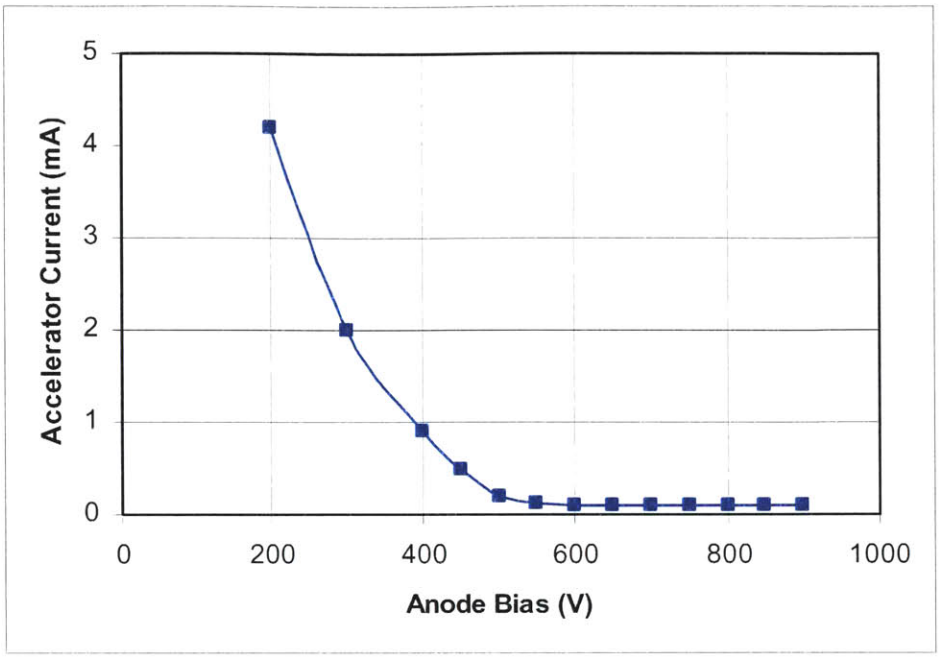

Figure 19: Accelerator currents measured during experiments.

Combining the ion impingement current shown in Figure 19 and the theoretical beam current from Figure 18, a new theoretical anode current is plotted against experimental values in Figure 20. The theoretical anode current is now within 10% of the experimental values, and the trends between these two curves are now in good agreement. If the problem of electron back-streaming is solved, increased accuracy can be expected. It should be noted that the anode current does not relate to thrust directly; the thruster performance is determined by the extracted ion beam current. The theoretical anode current shown in Figure 20 is only used to validate the theory with the experiments; it does not factor in the performance calculation.

The ion extraction model in this case is generally accurate in comparison with the experiments. Prediction of the beam current, combined with the observable accelerator current, yields a satisfactory resemblance to the experimental anode current. However, since the "shape factor" for Eq. 51 is derived from some part of the experimental data, it is desirable to have an additional set of data to compare with. From the concern of minimizing grid erosion, the operational range of this thruster configuration is between 675 V and 1075 V inter-grid potentials; below which

erosion by sputtering becomes significant and above which damages from dielectric breakdown (sparking) is prominent.

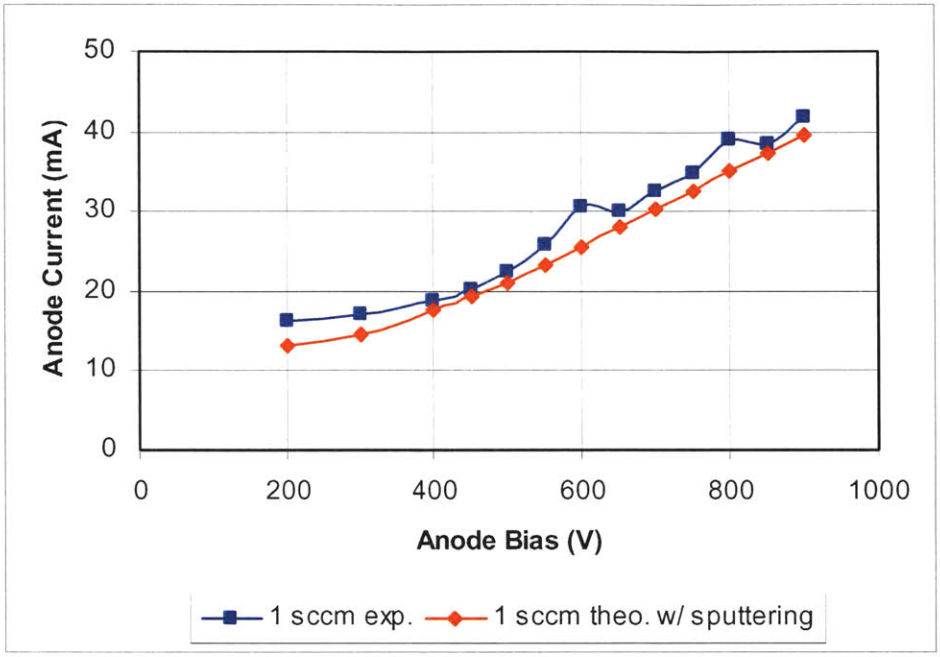

Figure 20: Final comparison between experimental and theoretical anode currents. Theoretical anode current is now the sum of theoretical beam current and observed accelerator current.

4.2.2 Beam Power and Utilization Efficiency

Comparisons between experimental and theoretical values for beam power and utilization efficiencies are shown in Figure 21 and 22, respectively. These experimental values were calculated in the same trial that generated the data of anode current, therefore the same glitches at 600 V and 800 V anode bias are observed. Besides these two glitches, an almost perfect resemblance to the theoretical beam power is found in Figure 21. Since the acceleration system utilized a different power unit, it is possible that the beam power is higher than the forward power of 27 W to the RF coil.

Both of the experimental beam power and utilization efficiency were calculated from the anode current measurements instead of the beam current. As a result, discrepancies toward the left-end

of the curves are observed in Figure 21 and Figure 22, although the one in Figure 22 is more obvious. This discrepancy is similar to the one presented in Figure 18 for the reason discussed in the previous section. Overall, the theory predicts higher propellant utilization with respect to the total applied potential, which corresponds to the experimental findings. Figure 22 suggests that within the operational range, it is always better to operate the thruster with the highest possible accelerating potential in order to minimize propellant loss.

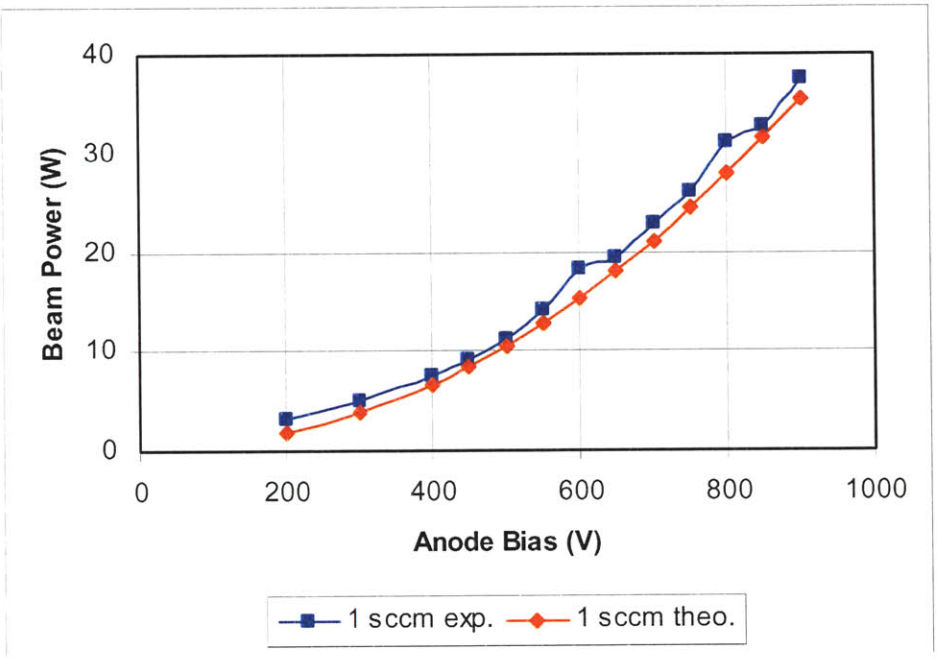

Figure 21: Comparison between experimental and theoretical beam powers.

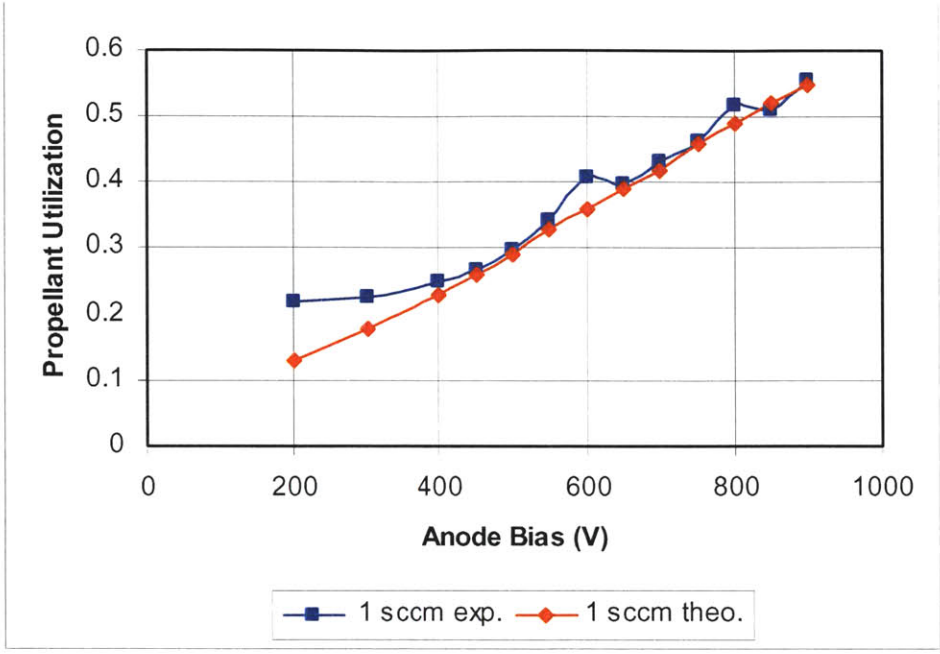

Figure 22: Comparison between experimental and theoretical utilization efficiencies.

4.3 Plasma Properties

4.3.1 Power Loading and Ionization

Although no data are available for comparison, plasma properties are calculated for the same experiments shown in the previous section for the purpose of general analysis. In Figure 23, chamber pressure is seen decreasing with respect to increasing extraction voltage under the same input flow rate. This trend is obvious because the extracted beam current is not purely production-limited, but rather increases with increasing extraction potential. Particles leaving the system cause the chamber pressure to decrease as a result. In the same figure, ionization fraction is also plotted against the extraction voltage and an increasing trend is observed. As seen in Figure 23, the inverse relationship between ionization fraction and chamber pressure is plotted in Figure 24 with the condition of constant RF forward power and flow rate. The relationship between ionization and pressure, however, is not strictly one-to-one because many factors can alter the chamber pressure. A more meaningful indicator of ionization fraction is power loading, as shown in Figure 25, in which an almost linear trend between ionization and

power per unit flow can be observed regardless of chamber pressure. This relationship is not surprising because electrons having high thermal energy tend to collide with neutrals fast and frequent, causing high ionization fraction. The direct relationship between electron temperature and power loading, plotted in Figure 26, is also apparent.

The trend of ionization fraction in Figure 23 can now be explained by the concept of power loading (power per unit flow) discussed above. As extraction voltage increases, more ions fall through the screen grid and get accelerated to higher velocity. The results are decreases in the plasma density and total chamber pressure. With fixed input flow rate and little variation in RF power absorption, the remaining electrons now attain higher energy per particle and therefore become more ionizing. The increased ionization fraction does not outweigh the effect of decreased chamber pressure, thus the plasma density decreases with respect to the extraction voltage as illustrated in Figure 27. The electron density is calculated in the order of 10^{18} particles per cubic meter, which seems quite reasonable for an ion thruster. The profile of electron temperature, ranging from 3 eV to 4 eV, is also plotted in Figure 27. The increasing trend is directly related to the increased power loading. The calculated values of electron temperature are also deemed reasonable.

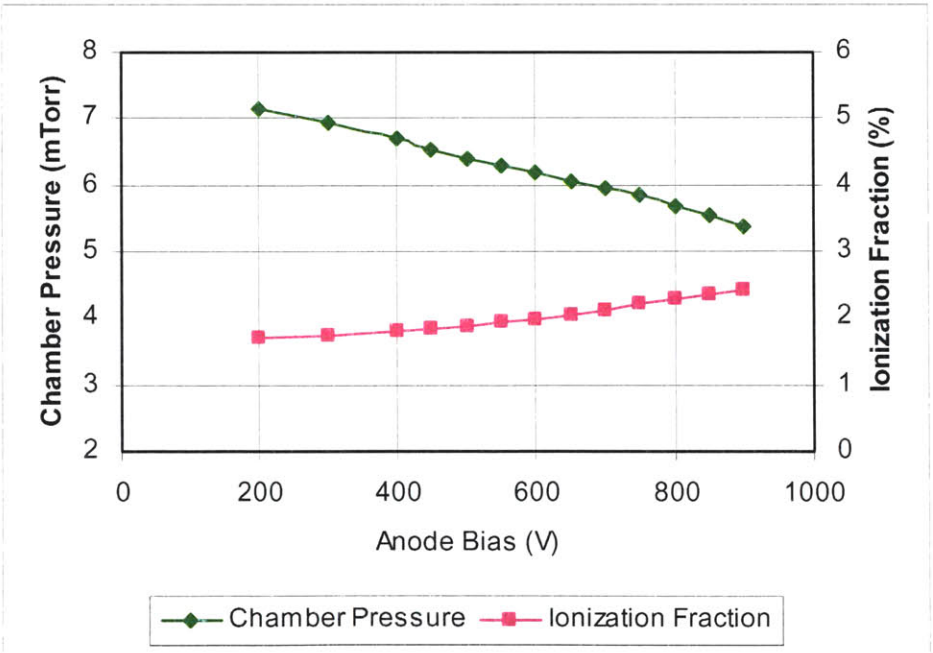

Figure 23: Chamber pressure and ionization fraction as a function of extraction voltage.

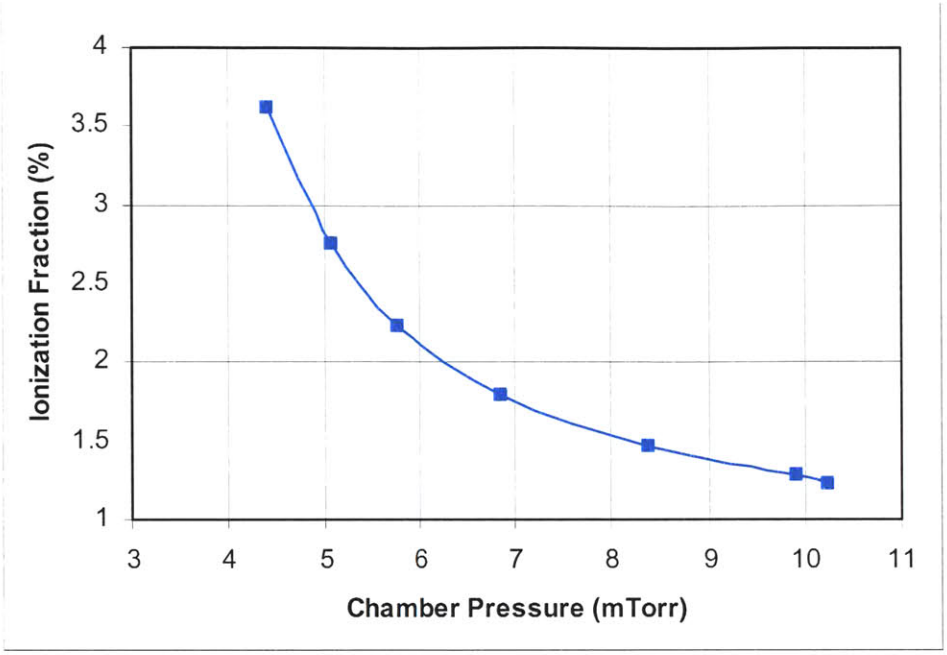

Figure 24: Ionization versus chamber pressure with fixed RF power and flow rate. 27 W RF power, 1.41 MHz and 1 sccm Xenon.

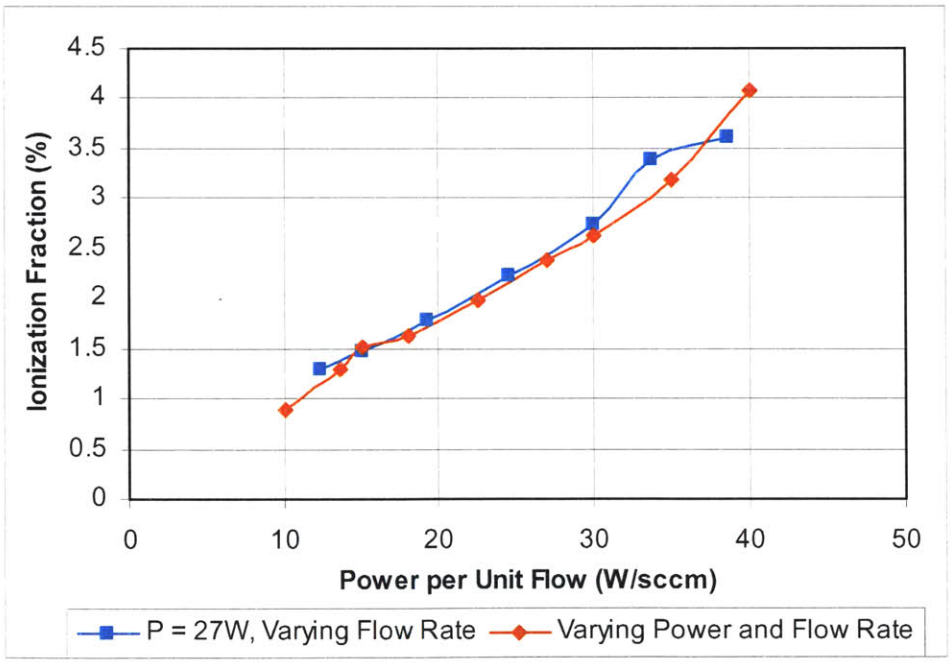

Figure 25: Example of ionization fraction as a function of power loading. Frequency is 1.41 MHz.

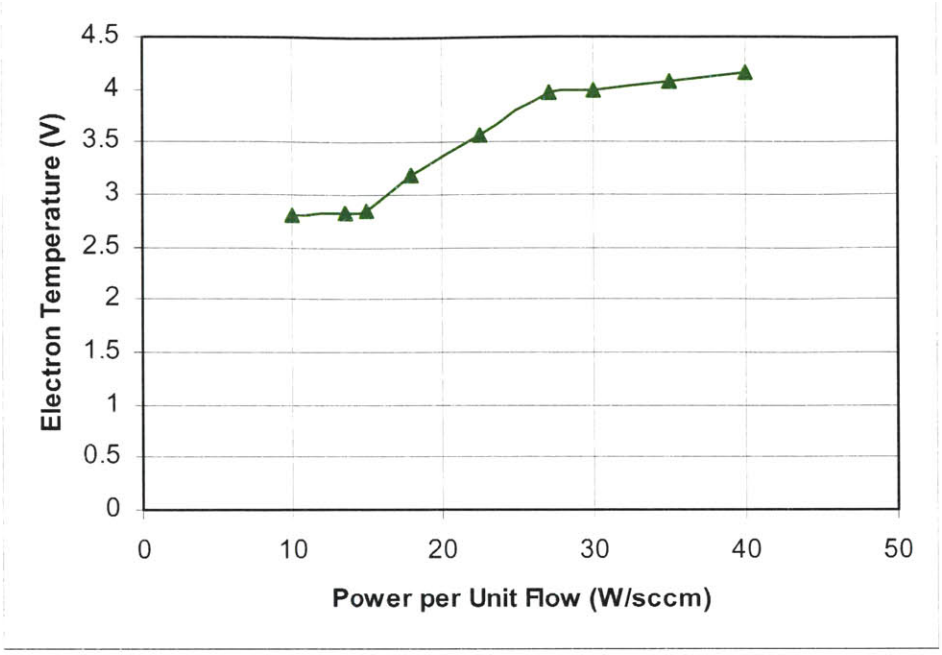

Figure 26: Example of electron temperature as a function of power loading. Frequency is 1.41 MHz.

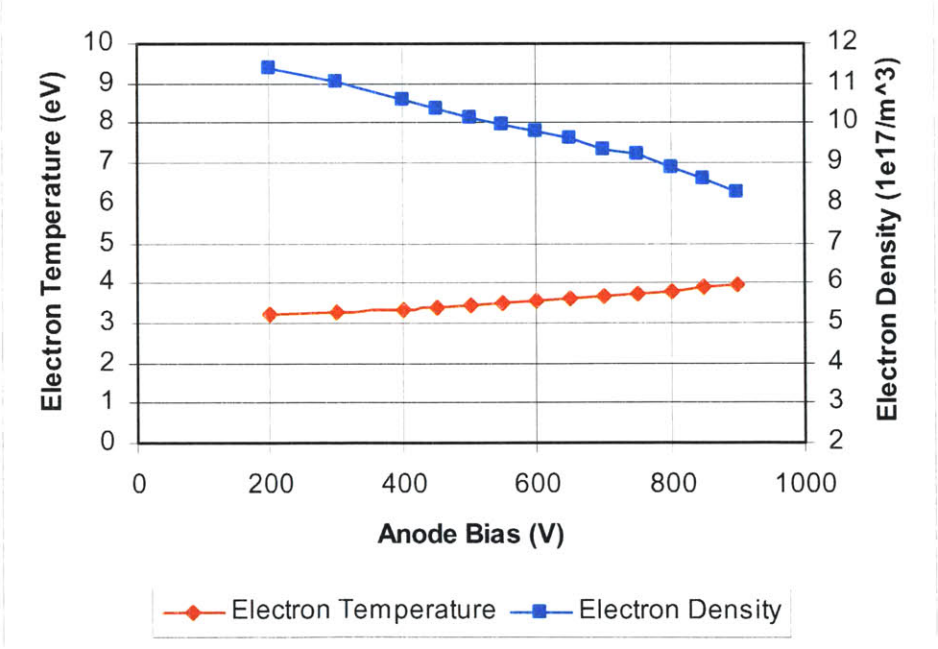

Figure 27: Electron temperature and density as functions of extraction voltage. 27 W forward power, 1.41 MHz, 175 V accelerator bias and 1 sccm Xenon.

4.3.2 Ion Transparency of the Screen Grid

Ion transparency is calculated from its definition described in Eq. 59 and is plotted as a function of extraction voltage in Figure 28. Ion transparency does not refer to the actual grid open fraction, which is 0.38 for the screen grid used in the experiments. It is interesting that the ion transparency drops below the physical open fraction for anode-bias voltages below 600 V, which indicates more ions are lost in the grid plate than through the apertures when the applied potential is low. The maximum ion transparency of 0.58 at 900 V anode bias suggests that the plasma density is quite sufficient to produce space-charge limited current. If the calculated beam current yielded an ion transparency above unity, it would mean that it is impossible to obtain such level of extraction with the available chamber plasma. The beam current in this extreme case would become purely production limited and would remain at the same level regardless of the applied potential.

Although the increasing trend of ion transparency with respect to the extraction voltage in Figure 28 seems predictable, ion transparency actually increases through the effect of enlarged plasma sheath in front of the screen holes. Ions in the chamber do not feel the extraction voltage directly; instead, they roam around freely and fall into the sheath in front of the screen holes by accident. Therefore, changes in ion transparency due to applied potential indicate changes in sheath characteristics (size or shape), which could contradict the assumed constant value of the "shape factor" that appears in the modified Child-Langmuir theory in Eq. 51, Section 2.4.2. The concept of shape factor assumes a constant proportionality between the sheath size in front of the screen hole and the screen grid plate. This assumption may not hold true if the applied potential deviates from the value at which the shape factor is calculated. The safest approach for using the simplified 1-D ion extraction model is to define a fixed range of applied potentials, then calculate the shape factor for best fit to current data. Since the shape factor depends primarily on the applied potential, other parameters such as flow rate, RF power, or frequency can be varied and the extraction model would still be valid. For example, a suitable range of applied anode bias for the Phase I RF micro ion thruster is between 800 V to 900V, where the performance seems to be the highest.

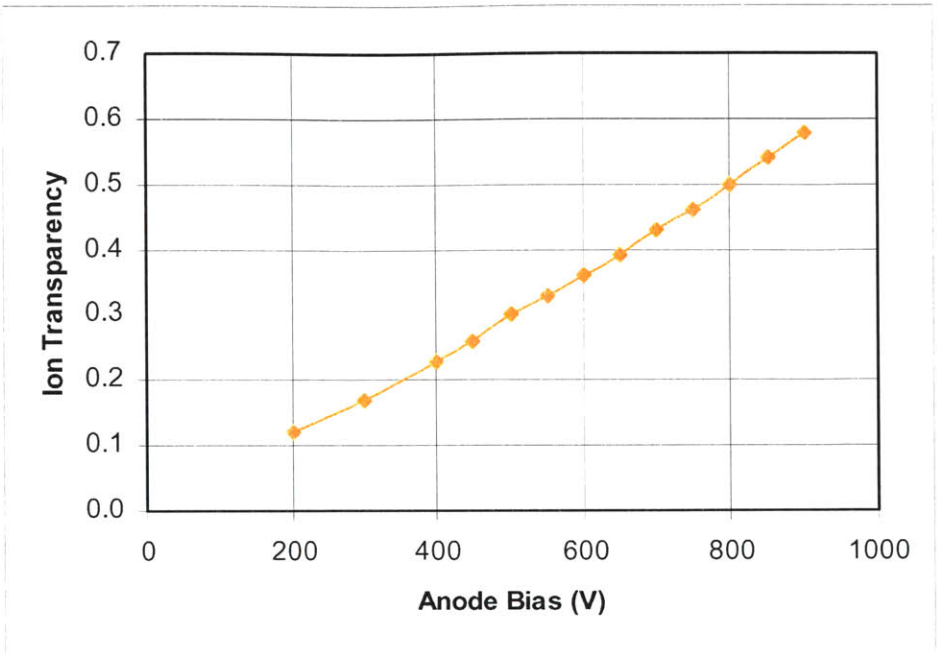

Figure 28: Ion transparency of the screen grid. 27 W forward power, 1.41 MHz, 175 V accelerator bias and 1 sccm Xenon.

4.4 Thruster Performance

4.4.1 Propulsive Performance

Thrust and specific impulse for the Phase I RF ion thruster are calculated and plotted in Figure 29. Input operating condition is the same as in the experiments: 27 W forward power, 1.41 MHz frequency, 175 V accelerator-bias potential, 0.305 mm grid spacing and 1 sccm Xenon. As shown in Figure 29, the maximum performance occurs at the highest possible applied potential, where thrust is about 2 milli-Newton and specific impulse reaches above 2000 seconds. Total power consumption at this operating point is approximately 73 W (27 W for RF generator, 36 W for ion beam and 10 W for neutralizer). The maximum thruster performance is limited by inter-grid dielectric breakdown, and the breakdown limit is calculated as 3.52×10^6 V/m. If the grid spacing is relaxed to 0.4 mm, the maximum allowable total potential becomes 1410 V, under which thrust and Isp can be increased to 2.66 mN and 2800 sec, respectively. The performance can also be improved with the addition of a third or even fourth acceleration grid rather than

adjusting grid spacing. However, grid addition increases structure complexity and may not be necessary for thrusters of such small scale.

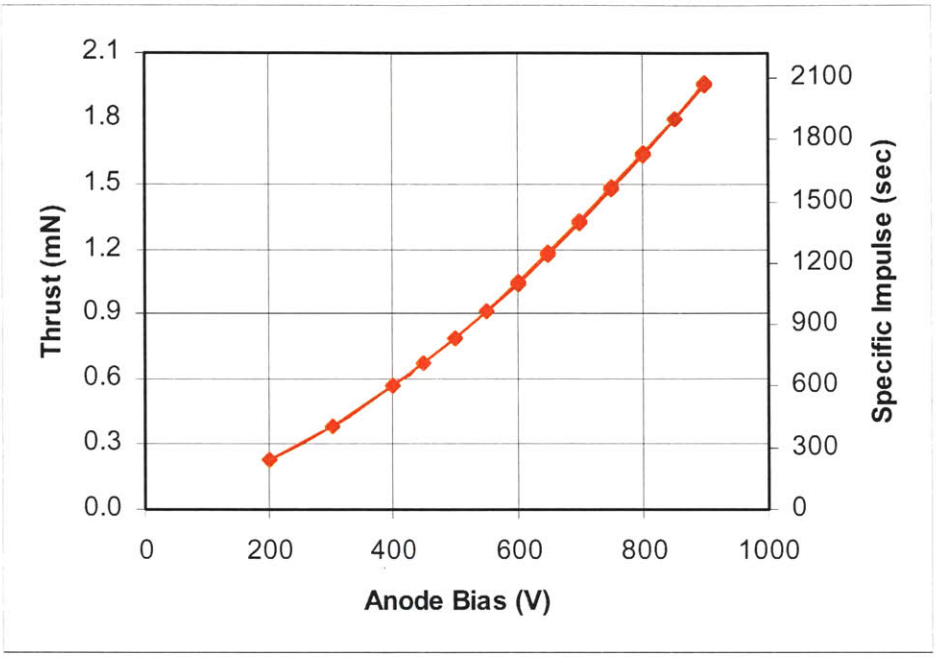

Figure 29: Propulsive performance of the Phase I RF ion thruster.

Figure 30 relates the propulsive performance to the RF forward power and it is apparent that higher forward power would generate higher thrust for a fixed beam power. The available forward power is controlled by the RF generator and therefore there exists an obvious limitation. Under a fixed beam power, the improvement in thrust from increasing RF power is the result of increased plasma density, which decreases the sheath size and increases the level of space-charge limited beam current. Consideration in constant beam power is not very meaningful because usually total power is the one being limited.

In the case of limited total power, diverting more power into the RF coil is a very inefficient way for generating thrust. Power should be concentrated on accelerating the beam ions in order to maximize the performance. Figure 31 shows the effect of power distribution on the thrust performance (neutralizer not included in the total power). For a fixed total power, diverting as much power as possible to acceleration instead of ionization would produce the highest thrust. For example, if the total power is 50 W, distributing only 20 W to the RF circuit yields the best

performance of 1.7 mN. Caution should be exercised in minimizing the RF forward power as lack of ionization power would result in insufficient plasma production, which can cause premature ion beam saturation. Calculations show that ion beam saturation is reached at forward power less than 14 W for the operating condition of 1.41 MHz, 1 sccm Xenon and 1075 (maximum) inter-grid potential. This value can be further reduced with the improvement in impedance matching since a large portion of the 14 W forward power is not absorbed by the plasma.

The effect of flow rate on the thrust performance was also investigated. Figure 32 demonstrates the thrust advantage of having high flow rate. Increasing flow rate increases thrust by two means: first is by pushing more neutral particles out of the chamber, and second by increasing the ion density in the chamber and thus shortening the effective spacing for producing the space-charge limited beam current. Jettisoning slow neutrals is a poor way for generating thrust because it lowers propellant utilization and penalizes specific impulse. Figure 32 also shows that although the extractable ion beam current is automatically saturated with the applied potential, the level of saturation can still vary depending on the flow rate. This change in saturation level is related to the shortening of the effective distance, mainly the parameter βl_s, in Eq. 51, Section 2.4.2. As the flow rate increases, the ion density increases and the sheath size decreases. The end result is an increased level of extractable beam current according to the modified Child-Langmuir theory. More on the effect of flow rate on the thruster performance can be found in the next section.

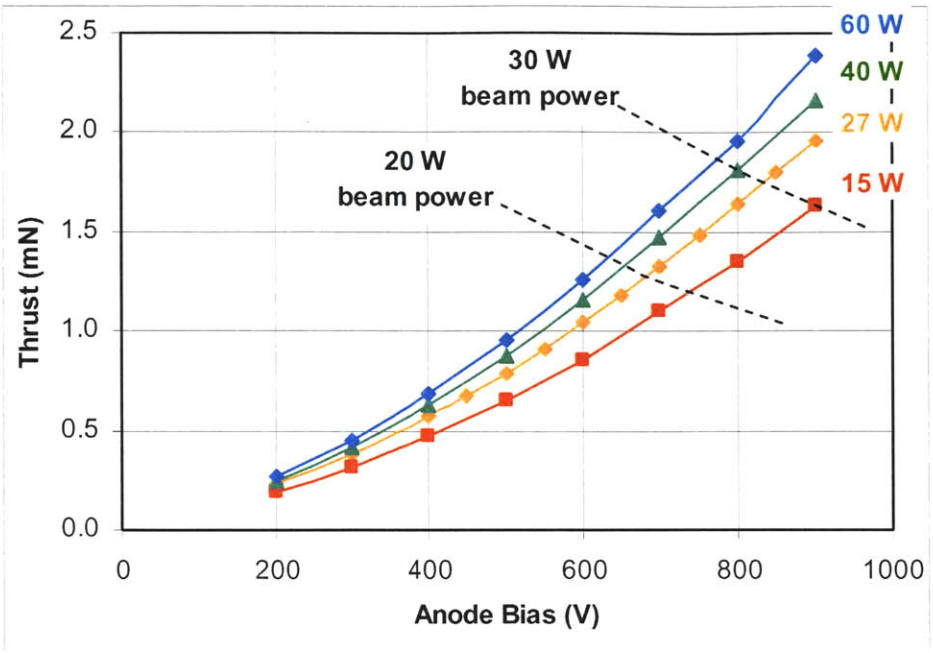

Figure 30: Thrust performance with respect to RF forward power. Colored lines represent constant RF forward power but variable total power. 1 sccm Xenon and 1.41 MHz.

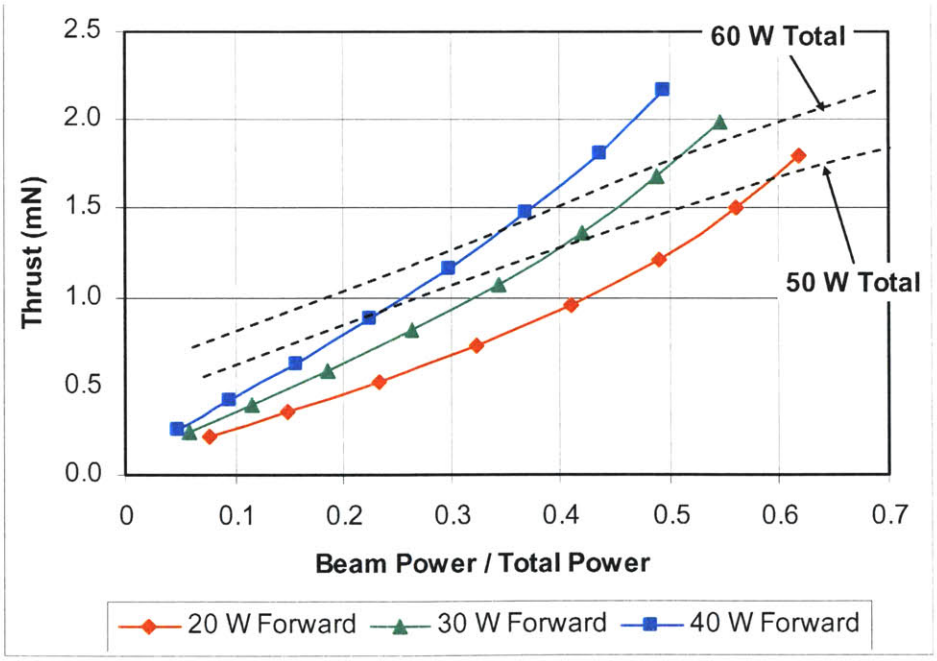

Figure 31: Effect of power distribution on thrust performance. Colored lines represent constant RF forward power but variable total power. 1 sccm Xenon and 1.41 MHz.

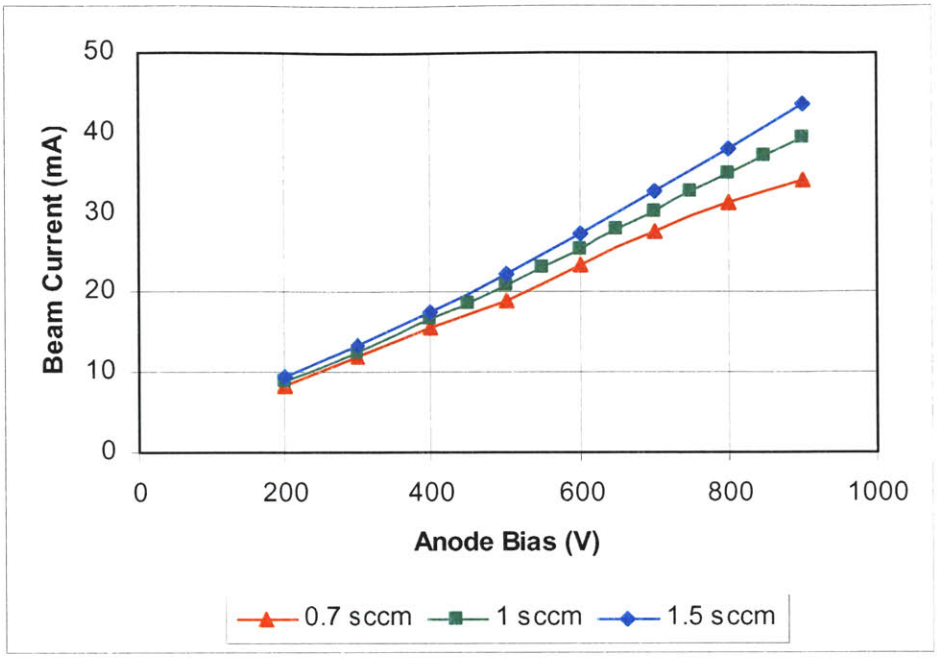

Figure 32: Effect of Xenon flow rate on ion beam current.

4.4.2 Efficiency and Performance Map

Electrical efficiency and production cost are calculated and plotted in Figure 33. The definition of electrical efficiency can be found in Section 2.4.4. In Figure 33, a maximum electrical efficiency of 0.57 is observed at the highest applied potential, where the energy cost is at the lowest value of 685 V per beam ion. This ion production cost is quite high compared to the German RIT-XT RF ion thruster, which requires less than 300 V of ion production energy [4]. The low efficiency and high production cost are mainly the result of poor coupling between the RF generator and the plasma; only about 50% of forward power is delivered to the plasma. The ion production cost is plotted with respect to specific impulse in Figure 34. The production cost decreases with increasing thrust and specific impulse; this is a general characteristic of an ion thruster.

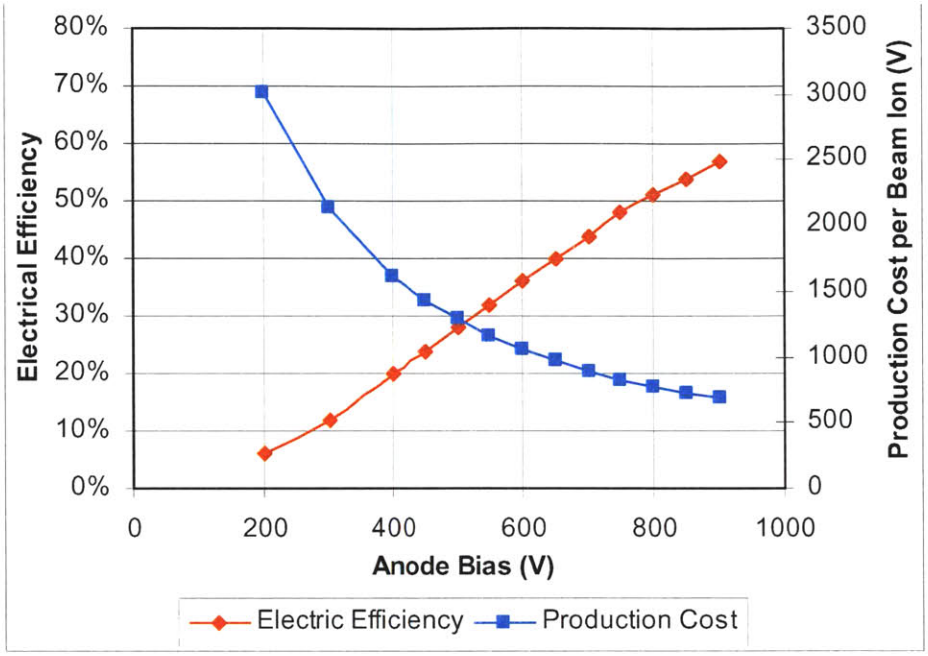

Figure 33: Efficiency parameters of the Phase I RF ion thruster. 1 sccm Xenon and 1.41 MHz.

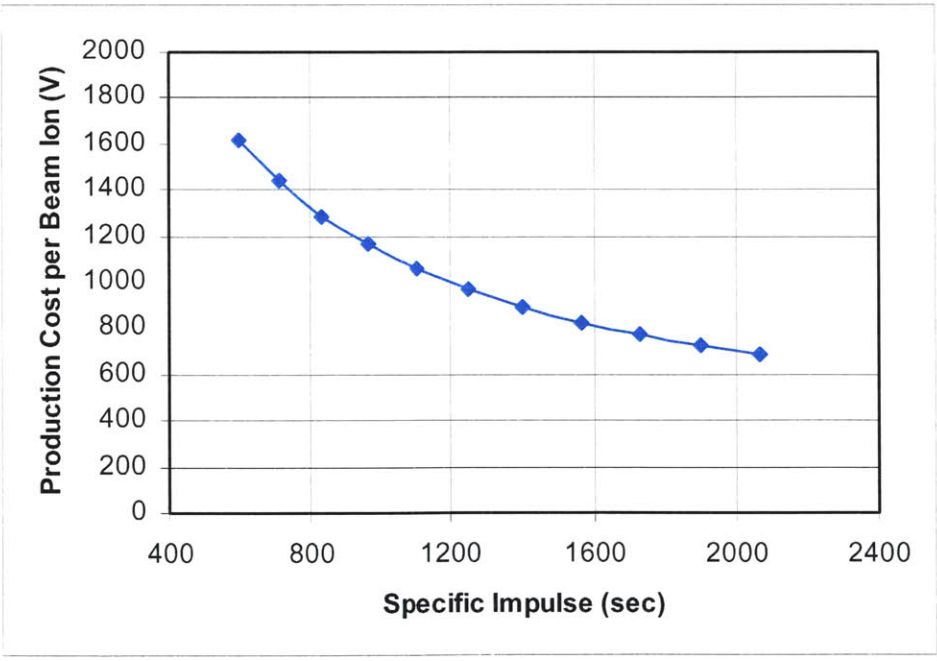

Figure 34: Ion production cost as a function of Isp. 1 sccm Xenon and 1.41 MHz.

Two performance maps are shown in Figures 35 and 36 to illustrate the fundamental tradeoff between electrical efficiency and propellant utilization. From Figure 35, if electrical efficiency is chosen for optimization, then the highest level of flow rate and applied acceleration potential are required. These conditions would also produce the highest thrust but a huge penalty in propellant utilization becomes inevitable. Generally increasing the flow rate increases not only thrust but also the escape rate of neutral particles, which results in a decrease of propellant utilization. Choosing which aspect to optimize is difficult because obviously it depends on the mission type. If the mission requires higher propulsive performance and is less strict on the propellant quantity, then optimizing electrical efficiency seems a good choice. If the wet mass of the spacecraft is the main design consideration, then perhaps optimizing propellant utilization is a more reasonable way. A balance point can be observed on the intersection of 0.7 sccm flow rate and 900 V anode bias. At this point, the electrical efficiency is 53%, just slightly below the obtainable maximum. The utilization efficiency of 0.69 at this operating point is quite satisfactory, considering 1.7 mN of thrust can be generated.

Figure 36 shows performance map B where the ion production cost is presented. The steep climb in the production cost above 0.7 utilization efficiency is very similar to the performance characteristics of a typical DC ion thruster. Changes in utilization efficiency in Figure 36 are generated with varying flow rates. When flow rate is reduced, utilization efficiency goes up, but the total ion beam current decreases because fewer ions are produced. As a result, the ratio between forward power and beam current (the production cost) increases.

As discussed in the previous section, minimizing the RF forward power for a fixed total power minimizes the production cost and maximizes the electrical efficiency. However, Figure 36 illustrates that solely minimizing RF power would decrease the power loading to the plasma and hence decreases ionization and propellant utilization. Optimization of both electrical efficiency and utilization therefore involves both minimizing the RF power and maximizing the power loading with the minimum acceptable flow rate. In Figure 36, intersections of 0.7 sccm – 27 W and 0.7 sccm – 15 W curves can be considered as optimum design locations. The calculated performance results for these design points are listed in Table 1. Notice the driving frequency is not optimized.

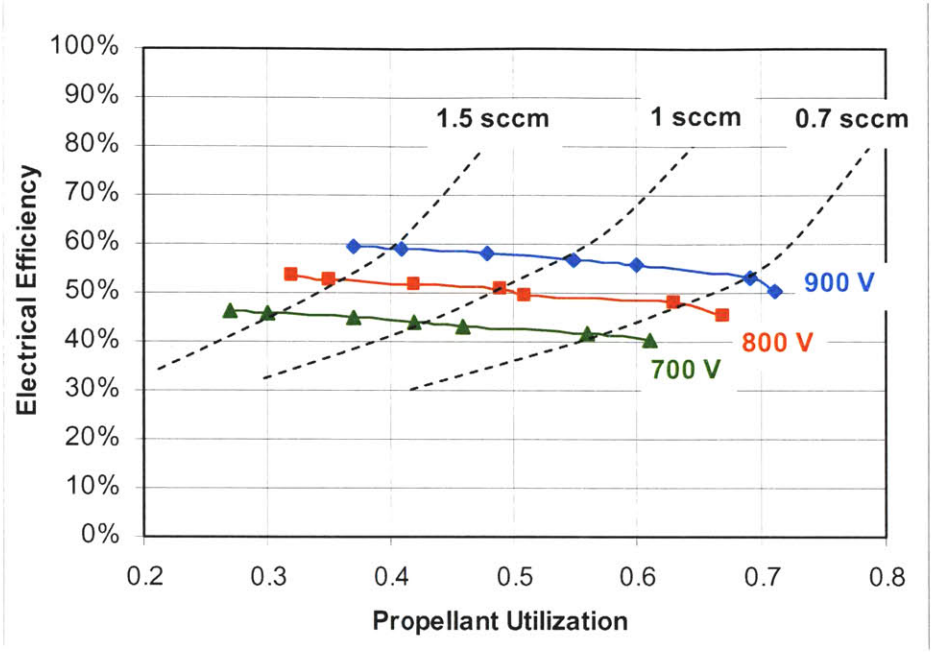

Figure 35: Performance map A of the RF ion thruster. Colored lines represent constant anode-bias potentials. Theoretical values with 27 W forward power and 1.41 MHz. Frequency not optimized.

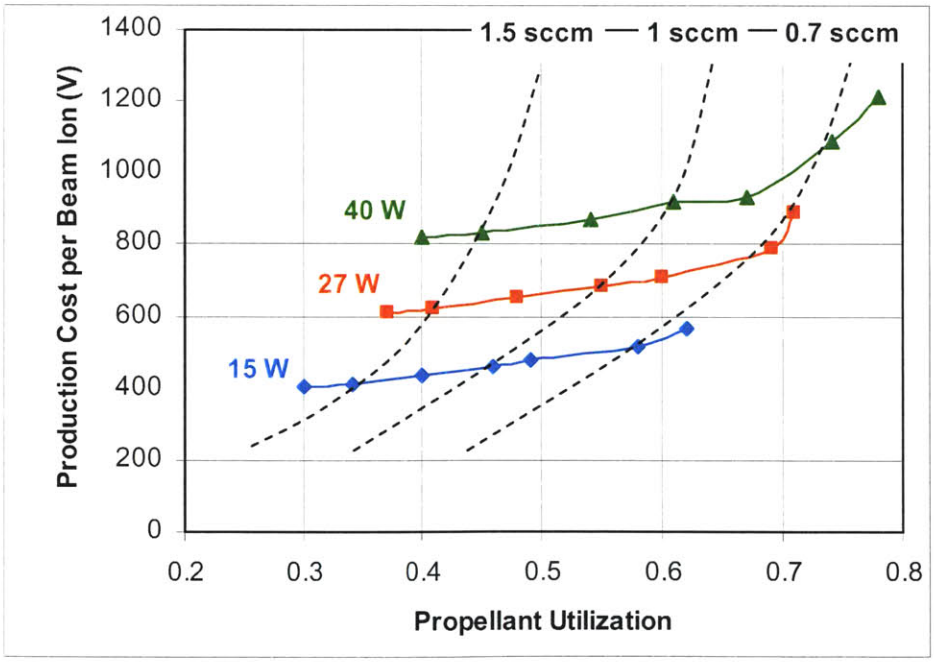

Figure 36: Performance map B of the RF ion thruster. Colored lines represent constant RF power. Theoretical values with 900 V anode bias and 175 V accelerator bias. 1.41 MHz frequency not optimized.

Table 1: Performance results of optimum design points from performance map B.

	0.7 sccm – 27 W forward power	0.7 sccm – 15 W forward power
Electrical Efficiency	0.53	0.63
Utilization Efficiency	0.69	0.58
Thrust *	1.69 mN	1.44 mN
Estimated Total Power †	72 W	56 W

* 900 V anode bias and175 V accelerator bias. 1.41 MHz frequency not optimized.

† Assumes 10 W neutralizer power, 90% DC/RF conversion efficiency and 1 W accelerator power loss.

4.4.3 Performance Comparison with DC Ion Thruster

Overall performance of the Phase I RF ion thruster can be compared with the miniature Xenon ion thruster (MiXI) developed by JPL, shown in Figure 37. Both thrusters are compact with grid diameter of 3 cm and can produce thrust in the range of milli-Newtons. MiXI is a 100 W Kaufman-type DC ion thruster with ring-cusp applied magnetic field, and it was designed for optimum performance [22, 23]. Since MiXI is very similar to the Phase I RF ion thruster in every aspect, it is a good subject for performance comparison. The comparison is shown in Table 2 below. The performance of the RF ion thruster changes with different operating conditions and its utilization efficiency is able to reach above 0.7 as shown in Table 1 in the previous section. Thrust would decrease if higher utilization efficiency were desired.

Efficiency comparison between the two thrusters is shown in Figure 38. In nominal operations MiXI wins this comparison with much lower ion production cost. However, the RF micro ion thruster has its potential. If assuming 100% power delivery (perfect coupling) from the RF generator, the RF thruster requires much less energy to produce a beam ion and the general tradeoff between efficiency and utilization diminishes. Of course, obtaining perfect coupling is difficult, if not impossible. Nevertheless, an 80% coupling efficiency should at least bring the RF ion thruster within a very competitive range of operation compared to a DC ion thruster.

Figure 37: MiXI 3cm ion thruster by JPL [23].

Table 2: Comparison between the Phase 1 RF thruster and MiXI [22, 23].

	Phase I RF ion thruster	MiXI
Thrust	2 mN *	1 – 5 mN
Isp	2100 sec †	1700 – 3200 sec
Total Power Consumption	77 W **	100 W
Propellant Utilization	0.55	> 0.75
Applied Magnetic Field	None	Permanent Magnet

* The thruster is operated with 27 W RF forward power and 1 sccm Xenon flow.

† Applied potentials include 900 V anode bias and 175 V accelerator bias.

** Assumes 10 W neutralizer power, 90% DC/RF power conversion efficiency of the generator and 1 W accelerator power loss.

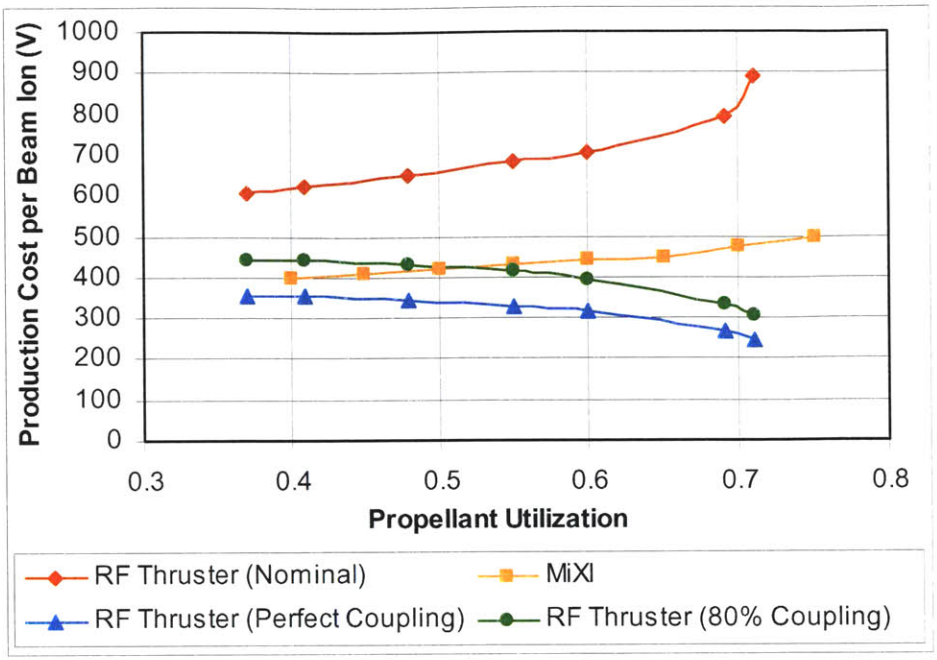

Figure 38: Efficiency comparison between the Phase 1 RF thruster and MiXI. Theoretical values with 1 sccm Xenon. 1.41 MHz driving frequency not optimized.

It is also noticed in Figure 38 that during nominal operations, the coupling efficiency decreases as the propellant utilization increases, which is the main reason for the high ion production costs. In other words, the RF coupling degrades when the flow rate is reduced. This phenomenon was also observed in the experiments, shown in Figure 42 in Section 4.6, as flow rates under 1 sccm could induce large increases in the reflected power. The decrease in coupling efficiency is the result of reduced plasma density, hence the reduced plasma resistance and resistive power consumption.

4.5 Effect of Wall Temperature

Chamber wall temperature of 400 K is assumed in the computation code since no measurement data are available. This particular value was estimated by the experimenters and should not to be taken as exact. Due to this uncertainty, it is necessary to investigate how changes of wall temperature can affect the outcome of computation. Figure 39 and 40 demonstrate the performance results with different wall temperature that is 100 K away from the estimated value.

No significant effect is observed, which indicates that the computation results are not sensitive to changes of wall temperature within a small range.

Decreases in performance, although subtle, are associated with increasing wall temperature as shown in Figure 39 and 40. The reduction of performance is essentially caused by the assumption of neutrals being thermalized with the wall. Because hotter neutrals are more energetic and can escape from the chamber more easily than cold neutrals, it is no mystery that the utilization efficiency is low with a hot wall. In the same process, the escaped neutrals decrease the density of the chamber plasma as shown in Figure 41. Thrust and specific impulse are also affected negatively as more neutrals escape. However, these reductions are not very apparent since the escaped neutrals (hot or cold) carry relatively low velocity and momentum compared to the accelerated ions.

The conclusion is that even though cooling the chamber wall can help retain the neutrals and therefore improve the performance by some fraction, it is not worth the extra design complexity. It is interesting that one would expect a different result for a classical DC ion thruster. In a DC ion thruster, the decreasing utilization efficiency associated with increasing wall temperature is rather significant because the utilization suffers not only from the escaped hot neutrals, but also from the decreased ionization fraction. As more neutrals escape, more primary electrons are lost to the anode without ionizing. Without the usage of primary electrons, an RF ion thruster definitely possesses an advantage when concerning energetic neutrals.

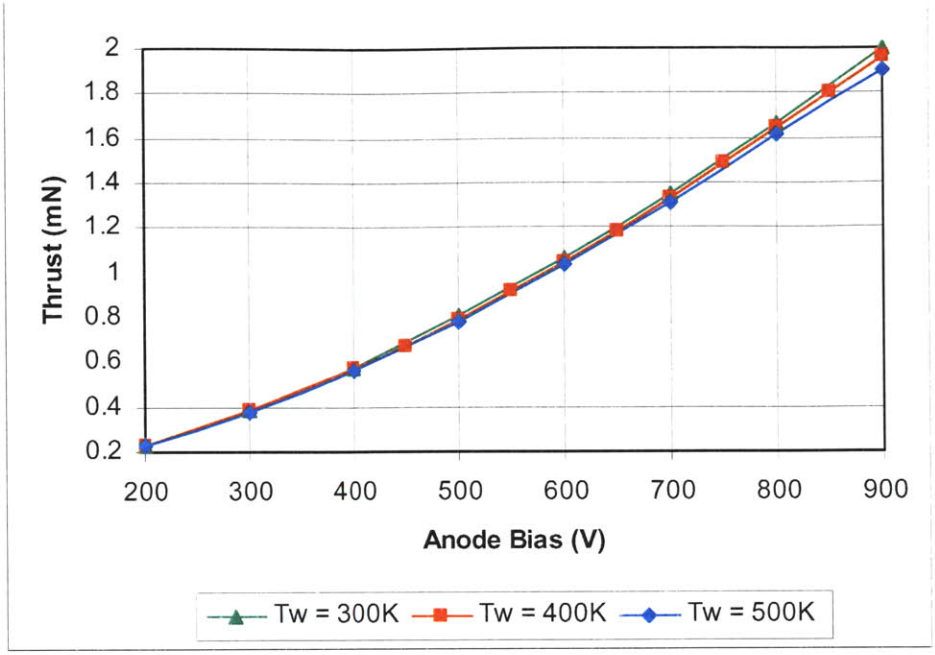

Figure 39: Effect of wall temperature on thrust performance.

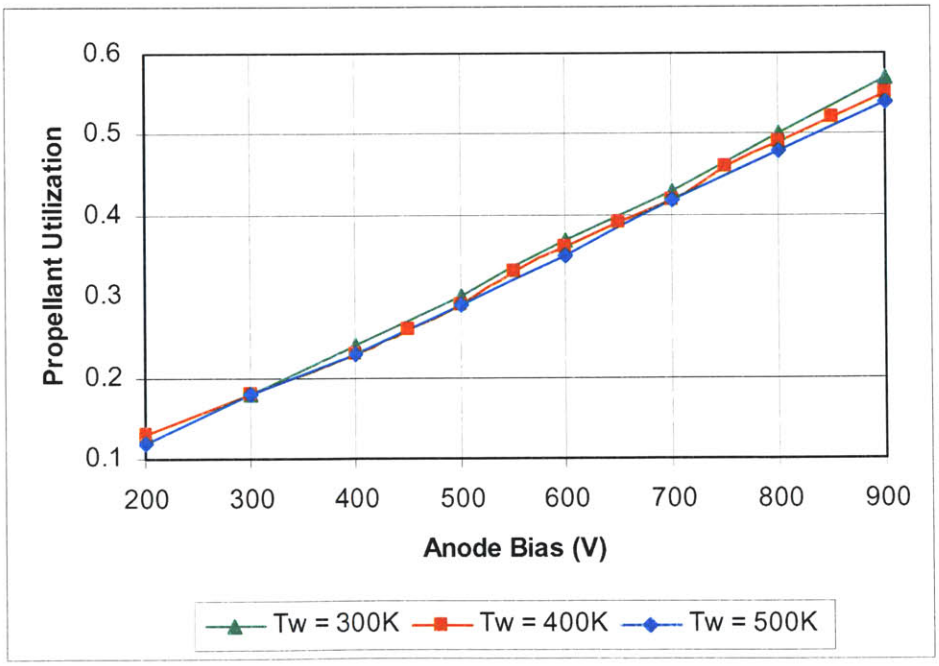

Figure 40: Effect of wall temperature on propellant utilization.

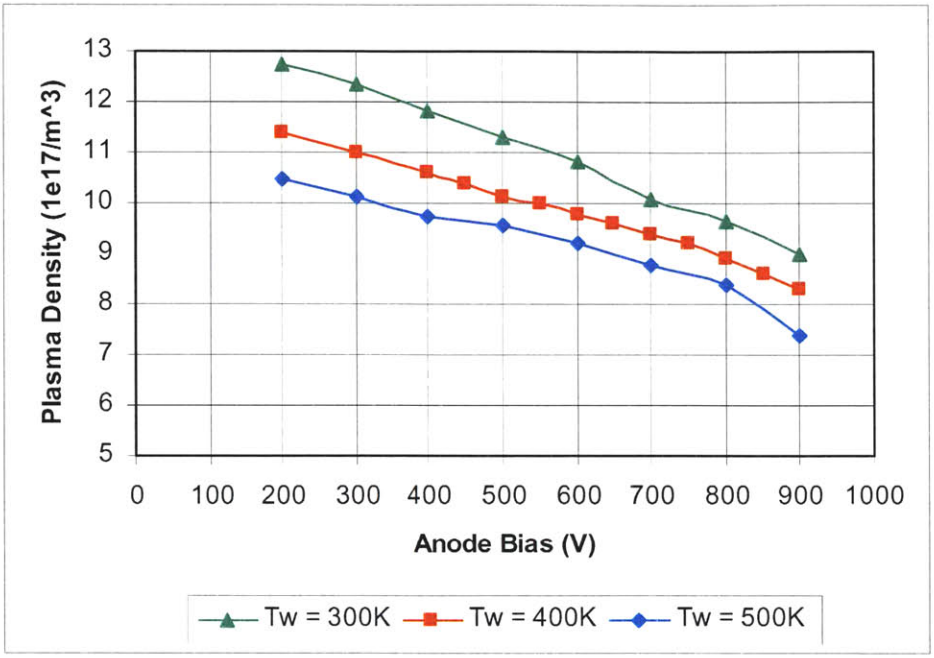

Figure 41: Effect of wall temperature on plasma density.

4.6 Effect of Driving Frequency

The properties of circuit elements seen in the computation code are calculated with the use of the experimental data presented in Figure 42. From the experiments, it was concluded that impedance matching can almost be achieved (minimum reflected power of 5%) with1.68 MHz driving frequency and fixed capacitance of 30,000 pF. The matching condition is sustained above 1 sccm Xenon flow. The data of minimum power reflection shown in Figure 42 are a little misleading, because a large portion of the non-reflected power is consumed by the capacitor and the coil instead of the plasma. Therefore, even though the matching frequency of 1.68 MHz guarantees maximum power delivery to the resistive loads, it does not necessarily guarantee maximum power delivery to the plasma because the resistive loads in this case consist of the RF coil, the plasma and the internal resistance of the capacitor.

In Figure 42, the rises of reflected power under low flow rates are caused by rapid decreases in plasma resistance and power absorption. This phenomenon was also discussed at the end of Section 4.4. Although the computation code can simulate the reduced power absorption

associated with the decreasing flow rates, it cannot produce the steep rises of the reflected power as seen in Figure 42. One concern is the absence of Coulomb collision frequency in the collision model, which could become significant when the pressure is decreased and the ionization fraction is increased. However, computations confirmed that the Coulomb collision frequency is always 4~10 times lower than the dominant electron-neutral scattering frequency. Failure to reproduce the rise of reflected powers in low flow rates is puzzling, and it obviously requires future work for clarification. Errors on the calculation of the reflected power, Eq. 49 in Section 2.3.2, are speculated. Nevertheless, the calculation of the absorbed power should be accurate enough to characterize the properties of the plasma.

As mentioned before, the maximum power delivery to the plasma does not necessarily occur at the matching frequency because power is consumed by other circuit elements as well. Distribution of power consumption among the circuit elements changes with respect to the frequency; therefore, predicting the optimum driving frequency for plasma power absorption is difficult. Figure 43 shows the computed percentage of the forward power being absorbed by the plasma, and the maximum power absorption actually occurs at 1.84 MHz, a little higher than the matching frequency of 1.68 MHz. This phenomenon suggests that even though the total power consumption by all the circuit elements decreases (because power reflection increases) when the frequency is increased from 1.68 MHz to 1.84 MHz, the shift in power distribution actually causes an increase of deliverable power to the plasma. Such shift in power distribution depends on the plasma resistance, which generally increases with increasing frequency. However, if the frequency is increased further to 2.06 MHz, the plasma resistance becomes too high and the power distribution shifts to other circuit elements. As a result, the absorbable power decreases. High level of power absorption is desirable because an increase in power loading increases the ionization fraction and hence the thruster performance. The computed result, plotted in Figure 44, is maximized ion beam current at the optimum frequency of 1.84 MHz under a given applied potential.

It can also be observed in Figure 43 that increasing acceleration potential decreases not only chamber pressure and plasma density (discussed in Section 4.3.1), but also power absorption by the plasma. This result resembles to the rises of the reflected power shown in Figure 42 when

the plasma density is reduced. Because less plasma is present, power absorption decreases and power reflection increases. Notice in Figure 43 the power absorption at the optimum frequency decreases from a high percentage of 78% to a moderate 62% as the applied potential increases toward the maximum. This observation demonstrates that, if the plasma density is sufficient, good coupling efficiency is indeed possible with the use of optimum frequency.

Combining the optimum frequency of 1.84 MHz and the optimum design points found in the two performance maps, Figures 35 and 36, a comparison is made with the performance using optimum design points but non-optimum frequency (1.41 MHz). This comparison is shown in Table 3. Notice that the low power absorptions seen in Table 3 are the result of low flow rates. It is observed from Table 3 that operating with the optimum frequency can improve the power absorption by approximately 10%. The improvements in efficiency and propulsive performance are not as great, which indicates that the increase in plasma density facilitates higher ion extraction to only a limited extent. Therefore, choosing whether or not to optimize the frequency for improving the performance depends more on the restrictions of the power unit.

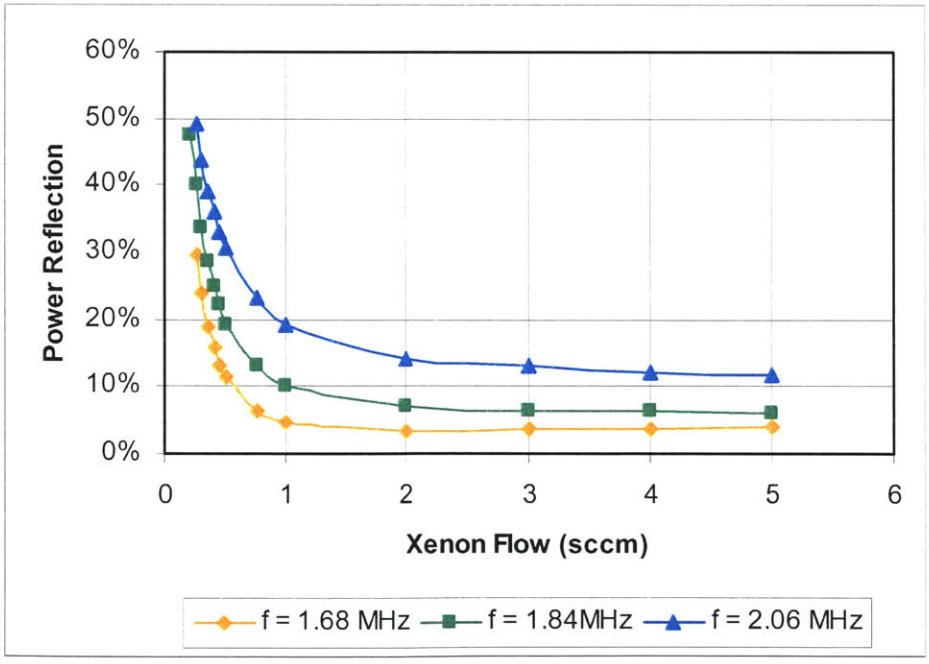

Figure 42: Experimental data on impedance matching. Plasma load is present. 30 W forward power and no extraction potential.

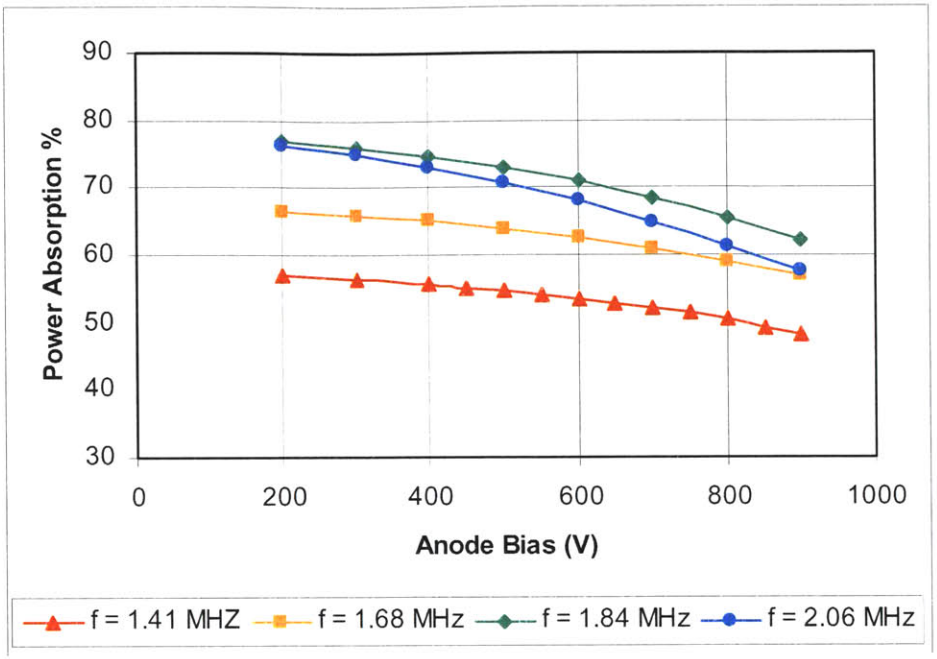

Figure 43: Effect of frequency on RF power absorption by plasma. Theoretical results computed with 27 W forward power and 1 sccm Xenon.

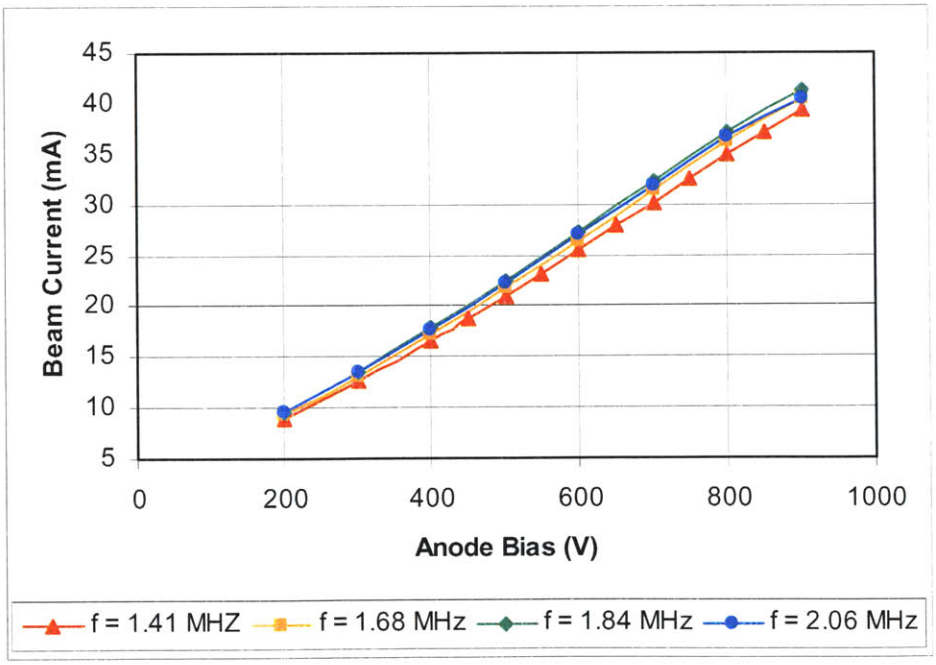

Figure 44: Effect of frequency on ion beam current. 27 W forward power and 1 sccm Xenon

Table 3: Performance comparison between optimized and non-optimized driving frequency.

Xenon Flow Rate	0.7 sccm			
Forward Power	27 W		15 W	
Frequency	1.41 MHz	1.84 MHz	1.41 MHz	1.84 MHz
Power Absorption	33%	42%	35%	47%
Electrical Efficiency	0.53	0.56	0.63	0.66
Utilization Efficiency	0.69	0.78	0.58	0.65
Thrust *	1.70 mN	1.91 mN	1.44 mN	1.60 mN
Required Total Power †	72 W	74 W	54 W	57 W

* 900 V anode bias and175 V accelerator bias.

† Assumes 10 W neutralizer power, 90% DC/RF conversion efficiency and 1 W accelerator power loss.

4.7 Discussion

It is unfortunate that the experimental results provided by Busek Co. are solely performance data and therefore can only be used to validate the ion extraction model. Although the calculations of ion density can demonstrate whether or not the plasma production is sufficient for generating the computed beam current, the actual value of ion density cannot be verified because it is not measured during the experiments. The calculations of electron temperature seem to be within reasonable ranges, but they are not verified either due to the same reason. Because of this lack of actual measurements, further refinement on the ICP discharge model is not possible. In addition, the steep increase of reflected power for flow rates below 0.7 sccm, observed in experiments and shown in Figure 42, cannot be correctly predicted by the computation. Discussion on this problem can be found in Section 4.6. Caution should be exercised when running the code with low flow rates.

Chapter 5

Summary

5.1 ICP Discharge Model

The global ICP discharge model developed from particle and energy balance equations yields satisfactory results. The calculated values of electron temperature (< 5 eV) and density (10^{17}~10^{18} ions/m^3) correspond to the usual values for a typical DC ion thruster. The general ionization fraction is below 4%, which is also similar to the one in a DC ion thruster. The validity of the transformer model used for calculating plasma power absorption is not verified, due to the lack of density measurements. However, the idea of using a transformer model in an ICP discharge has been around for some time without being challenged; it should bear some degree of accuracy. The radial non-uniformity of an ICP discharge is not considered in this global model, but should have minimum impact on the propulsive performance as long as the averaged density is sufficient for producing the modified Child-Langmuir beam current. Nevertheless, future work on modeling ICP discharges would have to include the effect of non-uniformity for more accurate simulation of the plasma properties.

5.2 Ion Extraction Model

The 1-D ion extraction model developed from the concept of the modified Child-Langmuir theory is simple and easily understood. It has been partially validated with the experimental data, and its accuracy would increase if more experimental data were given. The concept of using an effective spacing for calculating the space-charge limited current is not new, but its calculation varies with publications. The use of a shape factor to describe the effective distance between the plasma sheath and the screen grid is based on crude assumptions. Nevertheless, the computations demonstrate satisfactory results.

Special attention must be paid when using the 1-D extraction model. It is emphasized in Section 2.4.1 that if the ratio between grid spacing and screen aperture diameter is less than 0.6, the

characteristics of ion extraction become complicated and the extractable current can reach beyond the space-charge limitation. For such condition, the simplified 1-D ion extraction model is invalid. This restriction does not apply to micro ion thrusters because the screen holes used are usually small, with aperture diameter in the range of a few microns. The normalized spacing limit of 0.6 is difficult to break because grids with spacing in this scale are very susceptible to dielectric breakdowns. However, if the dimensions of the thruster are increased with increased screen aperture size, than it is possible to place grids more closely together for extracting more ion current. In this case, the 1-D extraction model would underestimate the beam current and therefore cannot be used.

5.3 Performance Characteristics of a RF Ion Thruster

It is shown in Chapter 4 that the performance characteristics of an inductively-coupled RF ion thruster resemble to the ones of a bombardment-type DC ion thruster. For the 3 cm diameter RF ion thruster used in the Phase 1 experiments, the thrust is in the range of milli-newtons and the specific impulse can easily reach above 2000 seconds. The calculated electrical efficiency ranges from 0.53 to 0.68, and the propellant utilization ranges from 0.58 to 0.78. Performance in nominal operations can be improved by optimizing the driving frequency and by better impedance matching. Total power consumption in general is below 80 W, which is very good for the listed performance. In comparison with a DC ion thruster of same scale, the RF thruster requires more energy to produce a beam ion and therefore is less efficient. However, it is observed that if the coupling efficiency can be improved beyond 80%, the RF thruster can outperform its counterpart in the efficiency category. In addition, as the coupling efficiency improves, the usually-inevitable tradeoff between electrical and utilization efficiency diminishes, because the usually increase of ion production cost near full utilization is entirely due to the degraded coupling.

5.4 Sources of Error

It is apparent that the computation code is susceptible to potential errors without validation from sufficient experimental data. The code is modified to the author's best ability with the use of available data, but there are still theories that require verification; for example, the global ICP

discharge model used for calculating the electron temperature and density. In addition to the transformer model, calculations of circuit element properties made from the measurements of reflected power are not 100% reliable as the second reflection wave is not considered. Discussion on this uncertainty can also be found in Section 2.3.2. Non-convergence during the calculations is rarely observed, although it does appear. The source of this type of error is unknown. Input of flow rate for this code is limited above 0.3 sccm by the initial guess of chamber pressure. As discussed in Section 4.7, results obtained from flow rates below 0.7 sccm might not be accurate.

5.5 Conclusion

Although the zero-th order global model does not fully describe the plasma properties in an ICP discharge, it does capture some essential characteristics of such discharge. The effect of coupling efficiency on thruster efficiencies is reproduced and is deemed very significant as better coupling can achieve both better electrical and utilization efficiency. From the comparison between the miniature RF and DC ion thrusters, it is observed that the performance advantage of a RF ion thruster exists only when the coupling efficiency is high. It is also concluded that optimizing frequency can increase power absorption and ionization tremendously. The propulsive performance cannot be greatly improved by utilizing the optimum frequency because the increased plasma density has a limited effect on increasing the maximum extractable ion beam current.

Appendix A

Manual for MATLAB Computation Codes

To execute the computation code, simply type in the function name and the input parameters in the MATLAB command window as follows:

RF_Model (flow rate, wall temperature, power, frequency, anode bias, accelerator bias)

The units:

1) Flow rate: sccm
2) Wall temperature: Kelvin
3) Power: Watts
4) Frequency: Mega-Hz
5) Anode bias: Volts
6) Accelerator bias: Volts

Example:

RF_Model(1, 400, 27, 1.41, 900, 175)

Operation parameters in RF_Model.m are predefined for the configuration of:

1) 30 mm diameter and 30 mm length discharge chamber
2) 2-turn coil with approximate 0.02 Ohms coil resistance
3) 30,000 pF capacitor in the matching network with 0.3 Ohms ESR
4) 10 Ohms line impedance
5) 300 micron screen and 200 micron accelerator grid with 0.012" spacing
6) 0.38 screen transparency and 0.17 accelerator transparency with total of 3650 grid holes

For other thruster configurations, these values can be easily updated in the first block of RF_Model.m.

The second block in RF_Model.m deals with propellant properties. Default propellant choice is Xenon with properties of:

1) 131.3 g/mole molecular mass
2) 12.1 eV first ionization energy

3) 10.2 eV first excitation energy

4) 3.63e-20 m^2 ionization cross-section coefficient.

For other propellant choices, these data will need to be updated in RF_Model.m before execution. In addition, sub-functions regarding collision cross-section and Maxwellian rate coefficient will need to be modified or replaced if other type of propellant is used because these temperature-dependent sub-functions are written specifically for Xenon. It is recommended that the code is used for Xenon only.

Appendix B

MATLAB Computation Codes

B.1 RF_Model.m (Executable File)

```
function RF_Model(flow_rate, wall_temperature, power, frequency, Anode_bias, Accelerator_bias)
% This is a 1-D performance model for a radio-frequency micro ion thruster
% Developed by Michael Tsay at MIT Space Propulsion Lab on 04/12/2005
% Final version was updated on 04/11/2006

% Units of Function Inputs:
% flow_rate            - [sccm], propellant volume flow rate
% wall_temperature     - [K], wall temperature of the chamber
% power                - [W], rms RF power
% frequency            - [MHz], RF frequency
% Anode_bias           - [V], anode-cathode voltage
% Accelerator_bias     - [V], anode-accelerator voltage

global e epsilon_0 mu_0 V_i V_ex Q_in sigma_0 lambda_i D_i
global OD R l l_c N l_g l_s t_s d_a N_holes
global m_i m_e sigma nu_en delta T_i mu_i n_n

%% Operation Variables and Nomenclature
%%%%%%%%%%%%%%%%%%%%%%%%%%%%%%%%%%%%%%%%%%%%%%%%%%%%%%%%%%%%%

% ID       - [m], chamber inner diamter
% OD       - [m], chamber outer diamter
% l        - [m], chamber length
% l_c      - [m], length of coil
% N        - number of turns of the coil
% P_rf     - [W], RF source power
% f        - [Hz], frequency
% C        - [f], capacitance of the matching network
% T_w      - [K], wall temperature (estimated from experiment)
% d_s      - [m], screen aperture size
% d_a      - [m], accelerator aperture size
% phi_s    - physical sreen grid transparency
% phi_a    - physical accelerator grid transparency
% l_g      - [m], grid seperation distance
% t_s      - [m], screen grid thickness
% N_holes - number of grid holes
% R_c      - [Ohm], resistance of coil
% ESR      - [Ohm], Equivalent Series Resistance of capacitor
% Z_0    - [Ohm], Characteristic impedance of lines
ID = 30e-3;
OD = 33e-3;
l = 30e-3;
l_c = 9.52e-3;    % 3/8 inches
N = 2;
P_rf = power;
```

```
f = frequency*1e6;
C = 30000e-12;
T_w = wall_temperature;
d_s = 300e-6;    % 300 microns
d_a = 200e-6;    % 200 microns
phi_s = 0.3791;
phi_a = 0.1685;
l_g = 0.305e-3;  % 0.012 inches
t_s = 200e-6;
N_holes = 3650;
R_c = 0.02;
ESR = 0.3;
Z_0 = 10;
%%%%%%%%%%%%%%%%%%%%%%%%%%%%%%%%%%%%%%%%%%%%%%%%%%%%%%%%%%%%%


%% Propellant Inputs (Xenon)
%%%%%%%%%%%%%%%%%%%%%%%%%%%%%%%%%%%%%%%%%%%%%%%%%%%%%%%%%%%%%

% M          - [g/mole], molecular mass
% V_i        - [V], first ionization energy
% V_ex       - [V], first excitation energy
% sigma_0  - [m^2], ionization cross-section coefficient

M = 131.3;
V_i = 12.1;
V_ex = 10.2;
sigma_0 = 3.63e-20;
%%%%%%%%%%%%%%%%%%%%%%%%%%%%%%%%%%%%%%%%%%%%%%%%%%%%%%%%%%%%%


%% Universal Constants
%%%%%%%%%%%%%%%%%%%%%%%%%%%%%%%%%%%%%%%%%%%%%%%%%%%%%%%%%%%%%

h = 2*pi*1.05e-34;              % [Js], Planck's constant
k = 1.38e-23;                   % [J/K], Boltzmann's constant
e = 1.6e-19;                    % [C] or [J/eV], electron chargeconstant
m_e = 9.1e-31;                  % [kg], electron mass
mu_0 = 4*pi*1e-7;               % [Tm/A], permeability of free space
epsilon_0 = 8.85e-12;           % [C/m/V], permittivity of free space
%%%%%%%%%%%%%%%%%%%%%%%%%%%%%%%%%%%%%%%%%%%%%%%%%%%%%%%%%%%%%


%% Assume ions and neutrals are thermalized with wall temperature
T_i = T_w/11594;                % [eV], ion temperature
T_n = T_w/11594;                % [eV], neutral temperature

m_n = M/1000/6.022e23;          % [kg], atom mass
m_i = m_n;                      % [kg], ion mass
R = ID/2;                       % chamber inner radius

Q_in = 8.28072e-16/sqrt(16*e*T_i/pi/m_i);
   % ion-neutral collision cross section

tolerance_Te = 0.01;
   % tolerance in electron temperature iteration
```

```
alpha = 0.0005;
   % initial guess of ionization fraction

tolerance_alpha = 0.0005;
   % tolerance in ionization fraction iteration

for x = 1:1000
   T_e_0 = 2;
      % initial guess of electron temperature [eV]
   clear m_dot

   for iter = 1:1000
      clear p
      p =0.1;
         % initial guess of chamber pressure [mTorr]
      clear a
      a = 3*flow_rate;
      for y = 2:1000
         m_dot(1) = 0;
         m_dot(2) = 0.05;
            % initialize flow rate [sccm]

         if abs(flow_rate - m_dot(y)) < 0.01
            break
         end
         if (sign(flow_rate-m_dot(y)) + sign(flow_rate-m_dot(y-1))) == 0
            a = 0.5 *a;
         end

         p = p + a *(flow_rate-m_dot(y))/flow_rate;
            % update chamber pressure

         n_n = (p*1e-3*133.32237)/((alpha/(1-alpha))*e*(T_e_0+T_i) + e*T_n);
            % neutral particle density

         n_e = (alpha/(1-alpha))*n_n;
            % electron number density

         nu_in = sqrt(8*e*T_i/pi/m_i)*n_n*Q_in;
            % ion-neutral collison frequency

         mu_i = e/m_i/nu_in;
            % ion mobility

         D_i = e*T_i/m_i/nu_in;
            % ion diffusion coefficient

         lambda_i = 1/n_n/Q_in;
            % ion mean free path

         %% Plot the profile of ionization rate and diffusion loss rate
         Te(1) = 0;
         n_i(1) = 0;
         loss(1) = 0;
         if flow_rate >= 0.5
```

```
    limit = 51;
else
    limit = 201;
end
for i=2:limit

    Te(i)= (i-1)*0.2;
    u_B = sqrt(e*Te(i)/m_i);
    g = Te(i)/(T_i);
    h_L = 0.86/sqrt(3 + (l/2/lambda_i) + (0.86*l*u_B/pi/g/D_i)^2);
    h_R = 0.8/sqrt(4 + (R/lambda_i) + (0.8*R*u_B/2.405/bessel(1,2.405)/g/D_i)^2);
    d_eff = 0.5*R*l/(R*h_L + l*h_R);
    n_i(i)= n_n*sigma_0*sqrt(8*e*Te(i)/pi/m_e)*(1+2*Te(i)/V_i)*exp(-V_i/Te(i));
        % ionization rate
    loss(i) = u_B/d_eff;
        % loss rate
end
T_e = Newton_Iteration(1e-10,1e-10,50);
    % solve the above profile for electron temperature with Newtown iteration [eV]

u_B = sqrt(e*T_e/m_i);
    % Bohm velocity

g = T_e/T_i;
    % ratio between electron and ion temperature

h_L = 0.86/sqrt(3 + (l/2/lambda_i) + (0.86*l*u_B/pi/g/D_i)^2);
    % normalized axial sheath edge density

h_R = 0.8/sqrt(4 + (R/lambda_i) + (0.8*R*u_B/2.405/bessel(1,2.405)/g/D_i)^2);
    % normalized radial sheath edge density

d_eff = 0.5*R*l/(R*h_L + l*h_R);
    % effective plasma size

A_eff = 2*pi*R*(R*h_L + l*h_R);
    % effective area for particle loss

V_eff = d_eff*A_eff;
    % effective discharge volume

Q_en = Avg_CS(T_e);
    % Maxwellian electron-neutral momentum transfer cross-section

nu_en = sqrt(8*e*T_e/pi/m_e)*n_n*Q_en;
    % electron-neutral momentum transfer collision frequency

omega = 2*pi*f;
    % angular frequency

sigma = (e^2)*n_e/m_e/nu_en;
    % electric conductivity

D = 1/sigma/mu_0;
    % diffusivity
```

```
delta = sqrt(D/omega);
    % skin depth

nu_i = n_n*sigma_0*sqrt(8*e*T_e/pi/m_e)*(1+2*T_e/V_i)*exp(-V_i/T_e);
    % ionization frequency


%% Calculate current in the RF coil by a transformer model
if delta >= R
    skin = R;
else
    skin = delta;
end

[P_abs, Z, I_c] = Transformer(skin, omega, P_rf, R_c, ESR, C);
    % power absorbed within plasma

R_xi = Maxwellian_rate_coefficient(T_e);
    % ratio between excitation work and ionization work

 n_e_new = (P_abs/V_eff)/(nu_en*3*(m_e/m_n)*e*(T_e-T_n) + nu_i*(1+R_xi)*e*V_i);
    % update ionization fraction by energy balance

alpha_new = n_e_new/(n_e_new + n_n);
    % update ionization fraction

V_total_applied = Anode_bias + Accelerator_bias;
    % applied total potential

[phi_i, flux_i, J_beam, delta_V] = Extraction(h_L, T_e, n_e, V_total_applied);
    % calculate beam current, ion transparency and ion flux

phi_n = 1/((1/phi_s) + (1/phi_a) - 1);
    % grid open fraction for neutrals

c_n = sqrt(8*e*T_n/pi/m_n);
    % mean thermal velocity for ions and neutrals

flux_n = (c_n*n_n)/4*phi_n*(pi*R^2);
    % neutral flux

eta_u = flux_i/(flux_i+flux_n);
    % utilization efficiency

m_dot(y+1) = m_i*J_beam/e/eta_u;
    % required flow rate to sustain discharge

 m_dot(y+1) = m_dot(y+1)*1.0236e7;
    % convert flow rate from kg/s to sccm (of Xenon)
end

if abs(T_e - T_e_0) <= tolerance_Te
   break
else
   T_e_0 = (T_e_0 + T_e)/2;
end
```

```
    end
    fprintf(1, 'convergence index = %1.4f \n', abs(alpha-alpha_new));
      % monitor convergence for alpha = alpha_new
    if abs(alpha_new - alpha) <= tolerance_alpha
      break
    else
      alpha = (alpha + alpha_new)/2;
    end
end
fprintf('\n');

rho = abs((abs(Z)-Z_0 ) / (abs(Z) + Z_0));
    % power reflection coefficient

Loss_Rate = n_e*u_B*A_eff;
    % wall-loss rate of ion due to ambipolar diffusion

V_net = Anode_bias;
V_beam = V_net;
P_beam = J_beam*V_beam;
    % beam power

eta_p = P_beam / (P_beam + P_abs);
    % ultimate propulsive efficiency

eta_e = P_beam /(P_beam + P_rf);
    % electric efficiency

eta_B = P_rf / J_beam;
    % [V], energy cost per beam ion production

C_i = sqrt(2*e*V_net/m_i);
    % accelerated ion exit velocity

C_n = c_n;
    % neutral exit velocity

Thrust = m_i*(J_beam/e)*C_i + m_n*flux_n*C_n;
    % [N], thrust

C = Thrust/(m_i*(J_beam/e) + m_n*flux_n);
    % [m/s], exit velocity

Isp = C/9.81;
    % [sec], specific impulse

fprintf('\n')

fprintf(1, '---------------------------------Plasma Properties---------------------------------\n\n');

fprintf(1, 'Electron temperature = %1.2f eV \n', T_e);
fprintf(1, 'Average electron density = %1.2d particles/m^3 \n',n_e);
fprintf(1, 'Power (RMS) absorbed within the plasma = %1.2f W \n', P_abs);
fprintf(1, 'Power reflection = %1.1f percent \n', rho*100);
if delta >= R
    fprintf(1, 'No dominant skin effect \n');
```

```
else
   fprintf(1, 'Skin depth = %1.2f mm \n', delta*1000);
end
fprintf(1, 'RMS current in the coil = %1.2f A \n', I_c);
fprintf(1, 'Wall-loss rate = %1.2d particles/s \n',Loss_Rate);
fprintf(1, 'Overall neutral density = %1.2d particles/m^3 \n',n_n);
fprintf(1, 'Ionization fraction = %1.4f \n',alpha);
fprintf(1, 'Total chamber pressure = %1.2f mTorr\n\n', p)

fprintf(1, '--------------------------------Thruster Performance----------------------------------\n\n');

fprintf(1, 'Beam current = %1.2f mA \n', J_beam*1000);
fprintf(1, 'Ion transparency = %1.2f \n', phi_i);
fprintf(1, 'Utilization efficiency = %1.2f \n',eta_u);
fprintf(1, 'Ultimate propulsive efficiency = %1.2f \n', eta_p);
fprintf(1, 'Electrical efficiency = %1.2f \n', eta_e);
fprintf(1, 'Energy cost per beam ion production = %1.2f  V\n', eta_B);
fprintf(1, 'Beam power = %1.2f W \n', P_beam);
fprintf(1, 'Specific impulse = %1.0f seconds \n', Isp);
fprintf(1, 'Thrust = %1.3f milli-Newtons (mN) \n\n', Thrust*1000);

fprintf(1, '-------------------------------------------------------------------------------------\n\n');

%% Plot magnetic field diffusion and induced electric field
for i = 1:101
    r(i) = (i-1)*R/100;
    B(i) = mu_0*(N/l)*I_c*(KModulus(r(i)/delta)/KModulus(R/delta))*cos(KPhase(r(i)/delta)-
           KPhase(R/delta))/sqrt(2);
    E(i) = D*mu_0*(N/l)*I_c/KModulus(R/delta)*(dModulus(r(i)/delta)*cos(KPhase(r(i)/delta)-KPhase(R/delta)) -
           dPhase(r(i)/delta)*KModulus(r(i)/delta)*sin(KPhase(r(i)/delta)-KPhase(R/delta)))/sqrt(2);
end

figure
plot(Te,n_i,Te,loss,':r')
xlim([0 ceil(T_e)+2])
h = legend('Ionization','Diffusion Loss',2);
xlabel('electron temperature [eV]')
ylabel('rate [1/s]')
title('Computing Plasma Temperature')
figure
subplot(2,2,[1 3]);
plot(r*1000, B/1e-3);
xlabel('radius from centerline [mm]')
ylabel('B_z, rms magnetic field [mT]')
title('Magnetic Field')
subplot(2,2,[2 4]);
plot(r*1000, E);
xlabel('radius from centerline [mm]')
ylabel('E_\theta, rms electric field [V/m]')
title('Induced Electric Field')
```

B.2 Newton_Iteration.m

```
function [x0] = newton_iteration(delta,epsilon,maxiter)
% This is a traditional Newton's iteration method used to solve Te
% Initial guess is set at Te = 5 eV

% Input  - delta is the tolerance for x0 (Te)
%              - epsilon is the tolerance for the function value f(x)
%              - maxiter is the maximum number of iterations
%       - need to develop f and df functions


x0 = 5;

for iter = 1:1:maxiter
   x1 = x0-(f(x0)/df(x0));
   error = abs(x1-x0);
   relerror = 2*error/(abs(x1)+delta);
   x0 = x1;
   f_final = f(x0);
   if (error<delta)|(relerror<delta)|(abs(f_final)<epsilon)
      break
   end
end
```

B.3 f.m

```
function f = f(Te)
% This is the function used to solve for Te in the Newton iteration

global R l  m_i T_i mu_i e m_e n_n sigma_0 lambda_i D_i V_i

u_B = sqrt(e*Te/m_i);
g = Te/T_i;
h_L = 0.86/sqrt(3 + (l/2/lambda_i) + (0.86*l*u_B/pi/g/D_i)^2);
h_R = 0.8/sqrt(4 + (R/lambda_i) + (0.8*R*u_B/2.405/bessel(1,2.405)/g/D_i)^2);
d_eff = 0.5*R*l/(R*h_L + l*h_R);

f = n_n*sigma_0*sqrt(8*e*Te/pi/m_e)*(1+2*Te/V_i)*exp(-V_i/Te) - (u_B/d_eff);
```

B.4 df.m

```
function df = df(Te)
% This is the derivative function used to solve for Te in the Newton iteration

global R l  m_i T_i mu_i e m_e n_n sigma_0 lambda_i D_i V_i


u_B = sqrt(e*Te/m_i);
g = Te/T_i;
h_L = 0.86/sqrt(3 + (l/2/lambda_i) + (0.86*l*u_B/pi/g/D_i)^2);
h_R = 0.8/sqrt(4 + (R/lambda_i) + (0.8*R*u_B/2.405/bessel(1,2.405)/g/D_i)^2);
d_eff = 0.5*R*l/(R*h_L + l*h_R);

du_B = 0.5*e/m_i/u_B;
dh_L = -0.86*0.5/((3 + (l/2/lambda_i) +
(0.86*l*u_B/pi/g/D_i)^2)^1.5)*2*(0.86*l*u_B/pi/g/D_i)*(0.86*l/pi/D_i)*(T_i)*((Te*du_B-u_B)/(Te^2));
dh_R = -0.8*0.5/((4 + (R/lambda_i) +
(0.8*R*u_B/2.405/bessel(1,2.405)/g/D_i)^2)^1.5)*2*(0.8*R*u_B/2.405/bessel(1,2.405)/g/D_i)*(0.8*R/2.405/bessel
(1,2.405)/D_i)*(T_i)*((Te*du_B-u_B)/(Te^2));
dd_eff = -0.5*R*l/((R*h_L + l*h_R)^2)*(R*dh_L +l*dh_R);

df = n_n*sigma_0*sqrt(8*e/pi/m_e)*(0.5/sqrt(Te)*(1+2*Te/V_i)*exp(-V_i/Te) + sqrt(Te)*(2/V_i)*exp(-V_i/Te) +
sqrt(Te)*(1+2*Te/V_i)*exp(-V_i/Te)*V_i/(Te^2)) - ((d_eff*du_B - u_B*dd_eff)/(d_eff^2));
```

B.5 Xenon Collision Cross-Sections

Avg_CS.m Xe_CS.m

```
function Q_en = Avg_CS(T_e)
% This function calculates the Maxwellian-averaged value of electron-neutral collision cross-section for a given
  averaged temperature

e = 1.6e-19;
m_e = 9.1e-31;

G(1)=0;
for i = 2:51
   x = 0.1*(i-1);
   G(i) = exp(-(x^2))*(x^5)*Xe_CS(x*sqrt(2*e*T_e/m_e));
   T(i-1) = (G(i) + G(i-1))*0.1/2;
end
Q_en = 4/3*sum(T);
```

```
function  Q_en = Xe_CS(T_e)
% This function extracts data of electron-neutral collision cross-section of a single Xenon atom from a given
  temperature
% Linear interpolation is used between data points

if T_e < 0
   fprintf(1,'\n');
   fprintf(1,'No collision cross-section data \n\n');
end
if T_e == 0
   Q_en = 0;
end
if T_e > 0 & T_e < 1
   Q_en = T_e*(-18e-20) + 20e-20;
end
if T_e >= 1 & T_e < 2.25
   Q_en = ((T_e - 1)/(2.25 - 1))*(14e-20 - 2e-20) + 2e-20;
end
if T_e >= 2.5 & T_e < 4
   Q_en = ((T_e - 2.5)/(4 - 2.5))*(32e-20 - 14e-20) + 14e-20;
end
if T_e >= 4 & T_e < 6.25
   Q_en = ((T_e - 4)/(6.25 - 4))*(40e-20 - 32e-20) + 32e-20;
end
if T_e >= 6.25 & T_e < 9
   Q_en = ((T_e - 6.25)/(9 - 6.25))*(37.5e-20 - 40e-20) + 40e-20;
end
if T_e >= 9 & T_e < 12.25
   Q_en = ((T_e - 9)/(12.25 - 9))*(33.5e-20 - 37.5e-20) + 37.5e-20;
end
if T_e >= 12.25 & T_e < 16
   Q_en = ((T_e - 12.25)/(16 - 12.25))*(29e-20 - 33.5e-20) + 33.5e-20;
```

```
end
if T_e >= 16 & T_e < 20.25
   Q_en = ((T_e - 16)/(20.25 - 16))*(24.5e-20 - 29e-20) + 29e-20;
end
if T_e >= 20.25 & T_e < 25
   Q_en = ((T_e - 20.25)/(25 - 20.25))*(20e-20 - 24.5e-20) + 24.5e-20;
end
if T_e >= 25 & T_e < 30.25
   Q_en = ((T_e - 25)/(30.25 - 25))*(17e-20 - 20e-20) + 20e-20;
end
if T_e >= 30.25 & T_e < 36
   Q_en = ((T_e - 30.25)/(36 - 30.25))*(14.5e-20 - 17e-20) + 17e-20;
end
if T_e >= 36
   Q_en = 14.5e-20;
end
```

B.6 Transformer.m

```
function [P_abs,Z,I_c] = Transformer(skin, omega, P_rf, R_c, ESR, C)
% This function calculates the power absorbed within plasma with the use of a transformer model
% It also returns the total network impedance and rms coil current

global mu_0 sigma nu_en OD R N l l_c

L_c = mu_0*pi*(OD/2)^2 * N^2 / l_c;
   % [H], inductance of the coil

R_p = (2*pi*R)/sigma/(l*skin);
   % plasma resistance

L_p = mu_0*pi*(R^2)/l + R_p/nu_en;
   % plasma inductance

L_m = mu_0*pi*(R^2)*N/l;
   % mutual inductance

R_2 = (omega^2)*(L_m^2)*R_p/(R_p^2 + (omega*L_p)^2);
   % transformed plasma resistance

L_2 = -((omega)*(L_m^2)*L_p/(R_p^2 + (omega*L_p)^2));
   % transformed plasma inductance

Z1 = complex((R_c + R_2), (omega*(L_c + L_2)));
Z2 = complex(ESR, -1/omega/C);
Z = Z1*Z2/(Z1+Z2);
   % total impedance

V_s = sqrt(P_rf*abs(Z)/cos(phase(Z)));
   % rms source voltage

I_c = V_s/abs(Z1);
   % rms coil current

P_coil = (I_c)^2 * (R_c);
   % rms power dissipation in the coil

P_abs = (I_c)^2 * (R_2);
   % rms power absorbed within the plasma
```

B.7 Maxwellian_rate_coefficient.m

```
function R_xi = Maxwellian_rate_coefficient(T_e)
% This function extracts Maxwellian rate coefficient data for Xenon  for a given electron temperature.
% It also calculates the ratio between excitation and ionization rate coefficient.
% Linear interpolation is used between data points.

global mu_i T_i V_i V_ex e m_e delta

if T_e < 1
   fprintf(1,'Electron temperature too low, not practical\n');
   fprintf(1,'No Maxwellian collision rate coefficient data\n\n');
   break
end

if T_e >= 9
   R_xi = (V_ex/V_i)*1;
   break
end

if T_e >= 1 & T_e < 1.5
   c_sigma_ex = ((T_e - 1)/0.5)*(5.2e-17 - 6e-19) + 6e-19;
   c_sigma_i = ((T_e - 1)/0.5)*(1.5e-17 - 1.5e-19) + 1.5e-19;
end
if T_e >= 1.5 & T_e < 2
   c_sigma_ex = ((T_e - 1.5)/0.5)*(4e-16- 5.2e-17) + 5.2e-17;
   c_sigma_i = ((T_e - 1.5)/0.5)*(1.5e-16 - 1.5e-17) + 1.5e-17;
end
if T_e >= 2 & T_e < 2.5
   c_sigma_ex = ((T_e - 2)/0.5)*(1.2e-15 - 4e-16) + 4e-16;
   c_sigma_i = ((T_e - 2)/0.5)*(5e-16 - 1.5e-16) + 1.5e-16;
end
if T_e >= 2.5 & T_e < 3
   c_sigma_ex = ((T_e - 2.5)/0.5)*(3e-15 - 1.2e-15) + 1.2e-15;
   c_sigma_i = ((T_e - 2.5)/0.5)*(1.2e-15 - 5e-16) + 5e-16;
end
if T_e >= 3 & T_e < 3.5
   c_sigma_ex = ((T_e - 3)/0.5)*(5e-15 - 3e-15) + 3e-15;
   c_sigma_i = ((T_e - 3)/0.5)*(2e-15 - 1.2e-15) + 1.2e-15;
end
if T_e >= 3.5 & T_e < 4
   c_sigma_ex = ((T_e - 3.5)/0.5)*(8e-15 - 5e-15) + 5e-15;
   c_sigma_i = ((T_e - 3.5)/0.5)*(3.5e-15 - 2e-15) + 2e-15;
end
if T_e >= 4 & T_e < 4.5
   c_sigma_ex = ((T_e - 4)/0.5)*(1.1e-14 - 8e-15) + 8e-15;
   c_sigma_i = ((T_e - 4)/0.5)*(6e-15 - 3e-15) + 3e-15;
end
if T_e >= 4.5 & T_e < 5
   c_sigma_ex = ((T_e - 4.5)/0.5)*(1.3e-14 - 1.1e-14) + 1.1e-14;
   c_sigma_i = ((T_e - 4.5)/0.5)*(8.5e-15 - 6e-15) + 6e-15;
end
if T_e >= 5 & T_e < 5.5
   c_sigma_ex = ((T_e - 5)/0.5)*(1.7e-14 - 1.3e-14) + 1.3e-14;
   c_sigma_i = ((T_e - 5)/0.5)*(1e-14 - 8.5e-15) + 8.5e-15;
```

```
end
if T_e >= 5.5 & T_e < 6
   c_sigma_ex = ((T_e - 5.5)/0.5)*(2e-14 - 1.7e-14) + 1.7e-14;
   c_sigma_i = ((T_e - 5.5)/0.5)*(1.4e-14 - 1e-14) + 1e-14;
end
if T_e >= 6 & T_e < 6.5
   c_sigma_ex = ((T_e - 6)/0.5)*(2.5e-14 - 2e-14) + 2e-14;
   c_sigma_i = ((T_e - 6)/0.5)*(1.8e-14 - 1.4e-14) + 1.4e-14;
end
if T_e >= 6.5 & T_e < 7
   c_sigma_ex = ((T_e - 6.5)/0.5)*(3e-14 - 2.5e-14) + 2.5e-14;
   c_sigma_i = ((T_e - 6.5)/0.5)*(2e-14 - 1.8e-14) + 1.8e-14;
end
if T_e >= 7 & T_e < 7.5
   c_sigma_ex = ((T_e - 7)/0.5)*(3.1e-14 - 3e-14) + 3e-14;
   c_sigma_i = ((T_e - 7)/0.5)*(2.3e-14 - 2e-14) + 2e-14;
end
if T_e >= 7.5 & T_e < 8
   c_sigma_ex = ((T_e - 7.5)/0.5)*(3.2e-14 - 3.1e-14) + 3.1e-14;
   c_sigma_i = ((T_e - 7.5)/0.5)*(2.8e-14 - 2.3e-14) + 2.3e-14;
end
if T_e >= 8 & T_e < 8.5
   c_sigma_ex = ((T_e - 8)/0.5)*(3.8e-14 - 3.2e-14) + 3.2e-14;
   c_sigma_i = ((T_e - 8)/0.5)*(3.5e-14 - 2.8e-14) + 2.8e-14;
end
if T_e >= 8.5 & T_e < 9
   c_sigma_ex = ((T_e - 8.5)/0.5)*(4e-14 - 3.8e-14) + 3.8e-14;
   c_sigma_i = ((T_e - 8.5)/0.5)*(3.9e-14 - 3.5e-14) + 3.5e-14;
end

R_xi = (V_ex*c_sigma_ex)/(V_i*c_sigma_i);
```

B.8 Extraction.m

```
function [phi_i,flux_i,J_beam, delta_V] = Extraction(h_L, T_e, n_e, V_total_applied)
% This function calculates ion beam current with the use of either classical or modified
% space-charge limited current model

global e epsilon_0 m_i m_e l_g l_s t_s d_a N_holes R

u_B = sqrt(e*T_e/m_i);

%% Calculate threshold of applied inter-grid potential
j_beam = e*u_B*h_L*n_e;
  % limited beam current density from the source into screen

V_threshold = (j_beam*(l_g^2)*9/(4*sqrt(2))/epsilon_0/sqrt(e/m_i))^(2/3);
  % threshold potential for using classical Child-Langmuir space-charge limited current model

if V_total_applied < V_threshold  % current is space-charge limited by inter-grid potential

  J_beam = 4*sqrt(2)/9*epsilon_0*sqrt(e/m_i)*(V_total_applied)^1.5 / l_g^2 *(d_a/2)^2 * pi * N_holes;

  flux_i = J_beam/e;
    % total ion flux into the screen grid

  phi_i = flux_i/(u_B*h_L*n_e*pi*R^2);
    % ion transparency of the screen grid

  else if V_total_applied > V_threshold  % modified space-charge limited current model

      delta_V = T_e *log(sqrt(8/pi)/(4*h_L)*sqrt(m_i/m_e));
        % potential drop between plasma and screen

      l_s = sqrt(4*sqrt(2)/9*epsilon_0*T_e/e/(n_e*h_L)*(delta_V/T_e)^1.5);
        % approximated sheath size between plasma and screen

      l_e = 2.5*l_s + t_s + l_g;
        % modified effective distance for space-charge limited current

      J_beam = 4*sqrt(2)/9*epsilon_0*sqrt(e/m_i)*(V_total_applied)^1.5 / l_e^2 *(d_a/2)^2 * pi * N_holes;

      flux_i = J_beam/e;

      phi_i = flux_i/(u_B*h_L*n_e*pi*R^2);

      if phi_i > 1

        phi_i = 1;

        flux_i = phi_i*u_B*h_L*n_e*pi*R^2;

        J_beam = flux_i * e;

      end
  end
end
```

B.9 Kelvin Functions

KModulus.m **dModulus.m** **KPhase.m** **dPhase.m**
bei.m **dbei.m** **ber.m** **dber.m**

```
function M_o = KModulus(x)
% This function calculates the modulus of the Kelvin Function

if abs(x) > 8
   fprintf(1,'Error in using the Kelvin Function\n')
   break
end

M_o = sqrt(ber(x)^2 + bei(x)^2);
```

```
function dModulus = dModulus(x)
% This function calculates the derivative of modulus of the Kelvin Function

global delta

dModulus = (0.5/delta)/sqrt(ber(x)^2 + bei(x)^2)*(2*ber(x)*dber(x) + 2*bei(x)*dbei(x));
```

```
function Phase = KPhase(x)
% This function calculates the phase of the Kelvin Function

Phase = atan(bei(x)/ber(x));
```

```
function dPhase = dPhase(x)
% This function calculates the derivative of phase of the Kelvin Function

global delta

dPhase = (1/delta)*(1/(1+(bei(x)/ber(x))^2))*((ber(x)*dbei(x)-bei(x)*dber(x))/(ber(x)^2));
```

```
function bei = bei(x);
% This is part of the Kelvin Function

X = x/8;
bei = 16*X^2 - 113.77777777*X^6 + 72.81777742*X^10 - 10.56765779*X^14 + 0.52185615*X^18 -
0.01103667*X^22 + 0.00011346*X^26;
```

```
function dbei = dbei(x)
% This is part of the Kelvin Function

X = x/8;
```

```
dbei = 4*X - 85.33333333*X^5 + 91.022178*X^9 - 18.49340113*X^13 + 1.174176338*X^17 -
0.0303508425*X^21 + 3.68745e-4*X^25;
```

```
function ber = ber(x)
% This is part of the Kelvin Function

X = x/8;
ber = 1 - 64*X^4 +113.77777777*X^8 - 32.36345625*X^12 + 2.64191397*X^16 - 0.08349609*X^20 +
0.00122552*X^24 - 0.00000901*X^28;
```

```
function dber = dber(x)
% This is part of the Kelvin Function

X = x/8;
dber = -32*X^3 + 113.77777777*X^7 - 48.54518438*X^11 + 5.28382794*X^15 - 0.208740225*X^19 +
0.00367656*X^23 - 3.1535e-5*X^27;
```

Appendix C

Sample Output

Testing Case:

- 1 sccm Xenon flow
- 400 K wall temperature
- 27 W forward power
- 1.41 MHz frequency
- 900 V anode bias
- 175 V accelerator bias

```
>> RF_Model(1, 400, 27, 1.41, 900, 175)
convergence index = 0.0041
convergence index = 0.0096
convergence index = 0.0099
convergence index = 0.0083
convergence index = 0.0058
convergence index = 0.0039
convergence index = 0.0025
convergence index = 0.0016
convergence index = 0.0010
convergence index = 0.0007
convergence index = 0.0004

----------Plasma Properties----------

Electron temperature = 3.98 eV
Average electron density = 8.29e+017 particles/m^3
Power (RMS) absorbed within the plasma = 13.02 W
Power reflection = 38.3 percent
Skin depth = 5.76 mm
RMS current in the coil = 7.83 A
Wall-loss rate = 2.25e+018 particles/s
Overall neutral density = 3.34e+019 particles/m^3
Ionization fraction = 0.0242
Total chamber pressure = 5.37 mTorr

----------Thruster Performance----------

Beam current = 39.41 mA
Ion transparency = 0.58
Utilization efficiency = 0.55
Ultimate propulsive efficiency = 0.73
Electrical efficiency = 0.57
Energy cost per beam ion production = 685.05 V
Beam power = 35.47 W
Specific impulse = 2066 seconds
Thrust = 1.963 milli-Newtons (mN)
----------
```

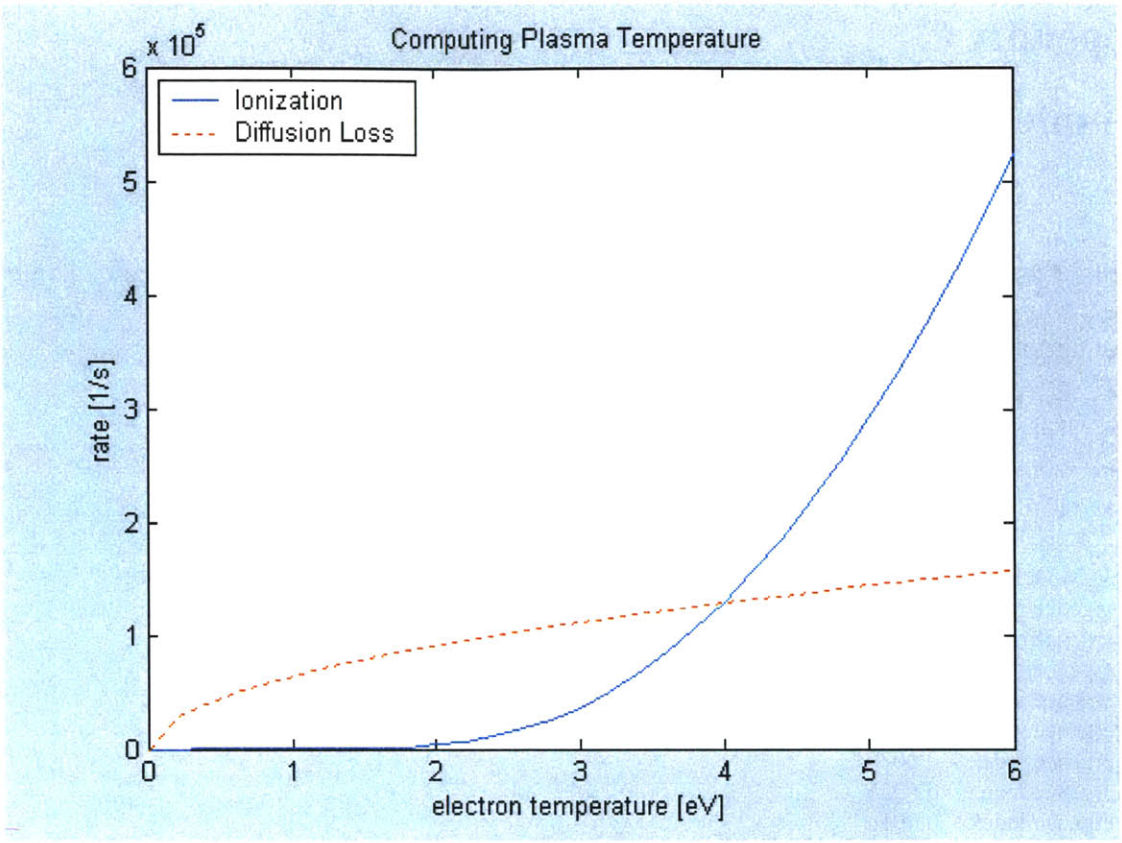
Computing Plasma Temperature
x 10^5
Ionization
Diffusion Loss
rate [1/s]
electron temperature [eV]
0
1
2
3
4
5
6

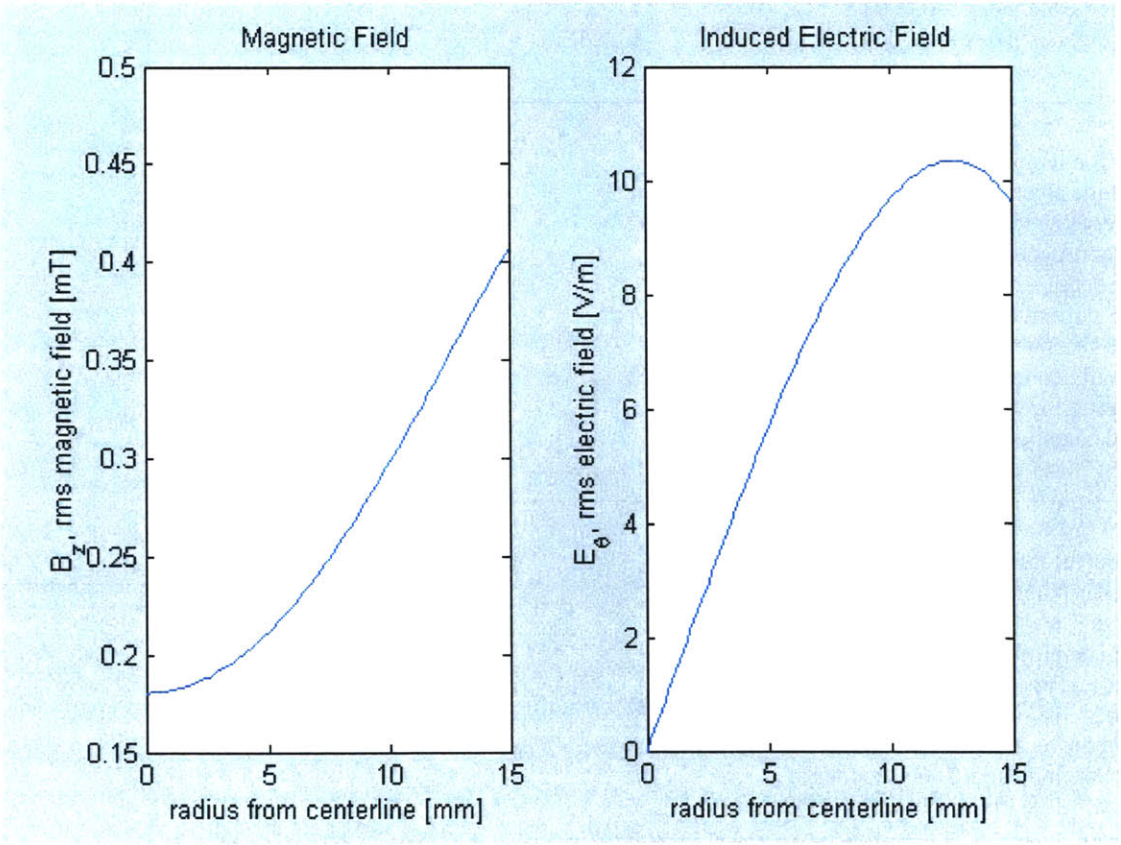
Magnetic Field
B_z, rms magnetic field [mT]
radius from centerline [mm]
0.15
0.2
0.25
0.3
0.35
0.4
0.45
0.5
0
5
10
15

Induced Electric Field
E_θ, rms electric field [V/m]
radius from centerline [mm]
0
2
4
6
8
10
12
0
5
10
15

References

[1] Leiter, H.J. and Feili, D., "RIT 15S – A Radio Frequency Ion Engine for High Specific Impulse Operation," AIAA 2001-3491, 37th AIAA/ASME/SAE/ASEE Joint Propulsion Conference & Exhibit, July 8-11, 2001.

[2] Jahn, R.G. and Choueiri, E.Y., "Electric Propulsion," Encyclopedia of Physical Science and Technology, 3rd ed., Vol. 5, 2002 Academic Press, pp 125-141.

[3] "RF Ion Propulsion," EADS Space Transportation website, accessed 04/10/2006. http://cs.space.eads.net/sp/SpacecraftPropulsion/IonPropulsion.html

[4] Leiter, H., Killinger, R., Bassner, H. Muller, J., Kukies, R. and Frohlich, T., "Evaluation of the Performance of the Advanced 200mN Radio Frequency Ion Thruster RIT-XT," AIAA 2002-3836, 38th AIAA/ASME/SAE/ASEE Joint Propulsion Conference & Exhibit, July 7-10, 2002.

[5] Leiter, H., Killinger, R., Kukies, R. and Frohlich, T., "Extended Performance Evaluation of EADS ST's 200mN Radio Frequency Ion Thruster," AIAA 2003-5010, 39th AIAA/ASME/SAE/ASEE Joint Propulsion Conference & Exhibit, July 20-23, 2002.

[6] Reichbach, J.G., Sedwick, R.J. and Martinez-Sanchez, M., "Micropropulsion System Selection for Precision Formation Flying Satellites," AIAA 2001-3646, 37th AIAA/ASME/SAE/ASEE Joint Propulsion Conference & Exhibit, July 8-11, 2001.

[7] Brophy, J.R. and Wilbur, P.J., "Simple Performance Model for Ring and Line Cusp Ion Thrusters," AIAA Journal 1985 0001-1452, Vol. 23, No. 11, pp 1731-1736.

[8] Gudmundsson, J.T. and Lieberman, M.A., "Magnetic Induction and Plasma Impedance in a Cylindrical Inductive Discharge," The Institute of Physics Electronic Journals, accessed on April 4, 2005. http://stacks.iop.org/0963-0252/6/540

[9] Fridman, A. and Kennedy, L.A., *Plasma Physics and Engineering*, Taylor & Francis Books, Inc., 2004, pp. 17-27, 199-200, 335-342 and 593-604.

[10] Szabo, J., Martinez-Sanchez, M. and Batishichev, O., "Fully Kinetic Hall Thruster Modeling," IEPC-01-341, 27th International Electric Propulsion Conference, Pasadena, CA, 2001.

[11] Mitchner, M. and Kruger Jr., C.H., *Partially Ionized Gases*, John Wiley & Sons, Inc., 1973, Reprint 1993, pp. 101-124 and 214-230.

[12] Abramowitz, M. and Stegun, I., *Handbook of Mathematical Functions with Formulas, Graphs, and Mathematical Tables*, U.S. Government Printing Office, 1972, pp 379-389.

[13] Martinez-Sanchez, M., "16.522 Space Propulsion Lecture Notes," Massachusetts Institute of Technology, spring 2005, accessible on MIT Open Course Ware. http://ocw.mit.edu/OcwWeb/Aeronautics-and-Astronautics/16-522Spring2004/CourseHome/index.htm

[14] "Transformer circuits," Hyperphysics website, copyrighted by C.R. Nave, Georgia State University, 2005, accessed on 04/2005. http://hyperphysics.phy-astr.gsu.edu/hbase/magnetic/tracir.html#c3

[15] "Inductance of a coil of wire," Hyperphysics website, copyrighted by C.R. Nave, Georgia State University, 2005, accessed on 04/2005. http://hyperphysics.phy-astr.gsu.edu/hbase/magnetic/indcur.html#c2

[16] Schmitt, R., "Analyze transmission lines with (almost) no math," EDN website, copyrighted by Reed Business Information, 1997-2006, accessed on 03/2006. http://www.edn.com/article/CA56702.html

[17] Sutton, G. and Biblarz, O., *Rocket Propulsion Elements*, John Wiley & Sons, 7th ed., 2001, pp. 679-688.

[18] Goebel, D., Brophy, J., Polk, J., Katz, I. and Anderson, J., "Variable Specific Impulse High Power Ion Thrusters," AIAA 2005-4246, 41st AIAA/ASME/SAE/ASEE Joint Propulsion Conference and Exhibit, July 10-13, 2005.

[19] Rovang, D.C. and Wilbur, P.J., "Ion Extraction Capabilities of Very Closely Spaced Grids," AIAA-82-1894, AIAA/JSASS/DGLR 16th International Electric Propulsion Conference, Nov. 17-19, 1982.

[20] Rovang, D.C. and Wilbur, P.J., "Ion Extraction Capabilities of Two-Grid Accelerator Systems," Journal of Propulsion, Vol. 1, No. 3, 1985, pp. 1772-179.

[21] Brophy, J.R., "Effect of Screen Grid Potential on Perveance," appears in "Advanced Ion Thruster Research," NASA CR-168340 (N84-19467), Jan. 1984.

[22] Wirz, R., Gale, M., Mueller, J. and Marrese, C., "Miniature Ion Thrusters for Precision Formation Flying," AIAA 2004-4115, 40th AIAA/ASME/SAE/ASEE Joint Propulsion Conference and Exhibit, July 11-14, 2004.

[23] Goebel, D., Katz, I., Ziemer, J., Brophy, J., Polk, J. and Johnson, L., "Electric Propulsion Research and Development at JPL," AIAA 2005-3535, 41st AIAA/ASME/SAE/ASEE Joint Propulsion Conference and Exhibit, July 10-13, 2005.